Fuel Sensitive Combustion Model Based on Quasi-Dimensional Multi-Zone Approach for Direct Injection Compression Ignition Engines

by

Kyoung Hyun Kwak

A dissertation submitted in partial fulfillment
of the requirements for the degree of
Doctor of Philosophy
(Mechanical Engineering)
in the University of Michigan
2014

Doctoral Committee:

Associate Professor Claus Borgnakke, Co-chair
Associate Professor Dohoy Jung, Co-chair
Professor Dionissios N. Assanis, Stony Brook University
Professor André L. Boehman
Assistant Professor Mirko Gamba

Acknowledgments

First of all I would like to acknowledge my advisers. Prof. Borgnakke, Prof. Jung and Prof. Assanis wonderfully guided me through my Ph.D. training. I started research with Prof. Assanis and Prof. Jung. They are truly excellent mentors. Later I got trainings from Prof. Borgnakke as well. He is such a great researcher and lecturer. He's knowledge and insights of thermodynamics are truly prodigious. It is really difficult to overemphasize my gratitude to my advisers. I'd also like to give my special thanks to my committee members Prof. Boehman and Prof. Gamba. I really appreciate their precious time and effort on my dissertation.

I wish to thanks to all the members and staffs of W.E. Automotive laboratory. They have been so great for past 6 years. I had really good time working with them. Luke, Ann Marie and Ashwin helped me enormously getting engine experiment data. Doohyun and I had lots of discussion and talk about research and more. I really appreciate that. I'd also like to say thank you to all my friends and members of Song Gang-ho Band. It was such a fun time together all these years.

Most importantly, I really appreciate every support from my family and my loved one. With all those cares, I finally finished my journey.

Lastly, I'd like to show my sympathy to victims of the Sewol Ferry Tragedy.

Table of Contents

List of Figures

List of Tables

List of Appendices

Abstract

This study describes a development of fuel sensitive quasi-dimensional multi-zone model for a direct injection compression ignition (DICI) engine. The objective is to develop fuel sensitive sub models of the DICI combustion process and integrate them into a thermodynamic engine cycle simulation. The proposed spray and evaporation models comprise the sub-models including fuel sensitive spray breakup, improved zone velocity estimations with transient fuel injection, spray penetration and tracking of evaporated fuel components. On these foundations, ignition delay models are formulated with two different descriptions based on the origin of the charge properties in a DICI engine. The global ignition delay model is based on the global combustion chamber charge properties while the local ignition delay model includes variations in properties of each spray zones. The Cetane number is used to describe a fuel effect for both models. Then, the premixed combustion model is reformulated to calculate a proper burn rate profile with respect to equivalence ratio and scale the profile with diluted air.

While the developed models are validated and evaluated by comparing the predictions with experimental data, some of important conclusions have been made. In the spray formation model, the degree of viscosity and surface tension effect on the spray formation and air entrainment is much more pronounced with DME fuel. For the fuels

closer to the conventional DF2, the effect of those properties is minimal. The evaporation model includes the behavior of evaporation at high pressure. The rate of evaporation is usually suppressed with higher pressure but at lower temperature than typical engine-like conditions, the effect is inverted. This effect might be significant for the low temperature combustion. Of the two proposed ignition delay models the local model has a slightly better accuracy compared to the global model. The results demonstrate the improvements that can be obtained when additional fuel specific properties are included in the spray ignition model. Although the proposed fuel sensitive combustion model calculates fuel effect to the combustion, the effect of ignition delay to the overall result of engine cycle simulation was much more dominant with given fuels in this study.

Chapter 1

Introduction

Rudolf Diesel received a patent for the Diesel engine in 1892 in Germany [1]. Since then, this internal combustion engine has been widely used in various applications. Because of its high compression ratio, the thermal efficiency of a Diesel engine is far superior to a typical gasoline engine. However due to the nature of burning lean and stratified mixture, nitro-oxide (NOx) and particular matter emissions are higher than from a gasoline engine.

Emission standards in the United States for the Diesel engine have become stricter. In addition to that, the newly designed Corporate Average Fuel Economy (CAFE) standard proposed a new fuel economy for heavy duty Diesel trucks [2]. Thus industry's demands for research and development of new technologies to meet these regulations are higher than ever. Furthermore, demand for renewable and sustainable energy resources is increasing due to environmental concerns. To cope with these extensive requests of the Diesel engine, various technologies are investigated and researched including high EGR application, various injection strategies, new turbocharger configurations, after treatment,

as well as developments in fuels like Biodiesel, Jet Propulsion fuel (JP8) and Synthetic fuels like Dimethyl ether (DME) and synthetic jet fuel (S8).

1.1 Modeling approaches for a direct injected compression ignition engine for alternative fuel applications

A computer simulation enables studying the application of alternative fuels in a direct injected compression ignition (DICI) engine with details of the spray combustion phenomena included. Insights from the computer simulation are essential for engine design development, engine calibration or adaptation of alternative fuels to reduce emissions and to achieve high fuel economy.

Figure 1.1 shows the general concept of an engine simulation and required sub-models. Among many parts of engine simulation, the most critical and complex part of the engine simulation for alternative fuel applications is the combustion. The combustion of a DICI engine occurs within the stratified charge that is created by the fuel spray, its breakup and subsequent evaporation. The temporal and spatial distributions of properties in the spray and the heat release of the combustion are highly dependent on the fuel properties and the burning characteristics. Therefore, it is very important to introduce the fuel effects on the combustion as accurate as possible.

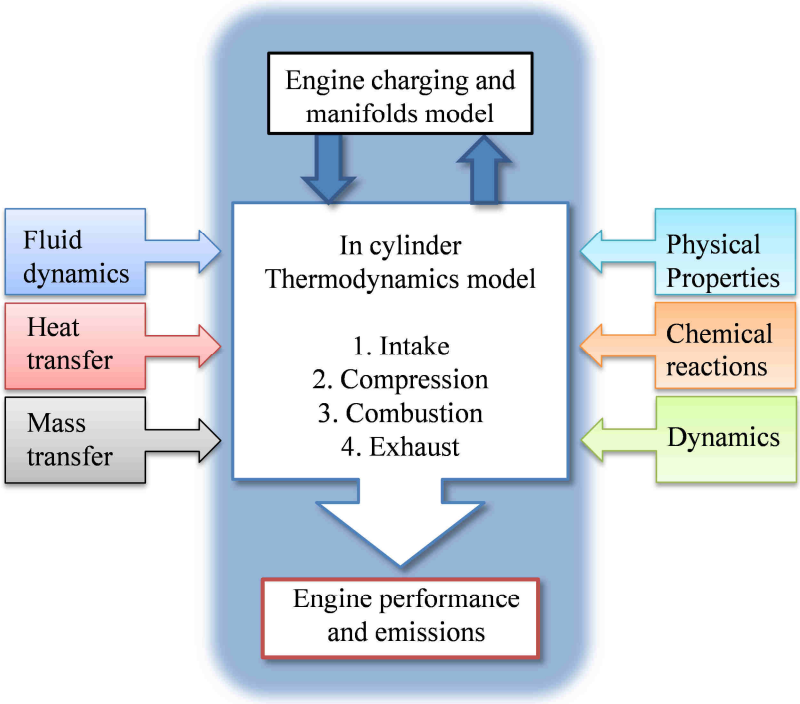

Figure 1.1 General engine simulation flow and area of required models

The approaches of modeling the combustion in a DICI engine can be described in three categories [3].

1) The zero dimensional (0-D) single zone approach assumes uniform cylinder charge properties and composition. Typically the burn rate of the combustion is curve fitted with a Wiebe function or its various derivatives [4]. Although this method is versatile and computationally cost effective, the model is not capable of predicting the influence from various fuels on the combustion. The Wiebe function needs to be carefully calibrated for a specific engine and operating points [5, 6]. Since the 0-D single zone models performs at a very high computational speed, they are frequently used where massive number of cycles need to be calculated [7].

2) The multi-dimensional multi-zone model also known as 3-D Computational Fluid Dynamics (CFD) model divides the whole engine cylinder into small cells and calculates the combustion in an Eulerian description. Because the model calculates mass, energy and momentum equations with chemical reaction mechanisms (reactive flow cases) in multiple cells, the resolutions of temporal and spatial distributions of temperature and charge compositions are very high. Due to radically increased computing power, both commercial and academic 3-D CFD codes are widely used for studying alternative fueled DICI engines. However, even with recent highly advanced computing techniques, it takes hours and more to calculate combustion and it is not suitable for general system integration or behavior analysis.

3) The quasi-dimensional multi-zone combustion model is an attractive method because it is striking a balance between computational efficiency and physical fidelity. The quasi-dimensional model combines some of the advantages of the zero-dimensional models and the multi-dimensional model. A typical model maintains a single uniform zone outside of the spray while dividing the spray into zones to provide temporal and spatial information. The spray phenomenon is described with a Lagrangian specification, so the zones carried with the spray move in the combustion chamber. In each zone, the quasi-dimensional multi-zone model solves the mass, energy and species balance equations but does not explicitly solve the momentum equation. Therefore, this type of models requires significantly less computing resources compared to the multi-dimensional models.

1.2 Overview of quasi-dimensional multi-zone DICI combustion concept

Many modern quasi-dimensional multi-zone DICI combustion models [3, 8–14] are influenced by Hiroyasu and his coworker's work [15–17]. Generally in the quasi-dimensional model, the fuel is injected into the combustion chamber according to the fuel injection schedule and it forms zones at each time step in both the axial and radial directions. The radial zone may be further divided in the rotational direction around the injection axis [13, 14]. Different zones have their own mass of fuel according to the injection rate. The mass of fuel in each zone can be either specified or calculated by using an empirical correlation based on the injection and chamber pressures and the injector geometry. The fuel injected into the chamber is initially assumed to form a liquid core until the liquid fuel jet break-up time has elapsed. Following the break-up, it is assumed that the fuel spray atomizes to fine droplets, each with a diameter equal to the Sauter Mean Diameter (SMD) which is a function of the cylinder conditions at the moment of injection. This is indicated in the time history shown in Figure 1.2.

The air entrainment rate depends on the physical position of each zone, with centerline zones receiving less and zones near the outer edge receiving more air. The amount of entrained air is calculated based on conservation of momentum applied to each zone. It is assumed that the momentum of the zone at any instant is equal to the momentum given to the zone upon nozzle exit. Since the mass of fuel and injection velocity of each zone is initially determined the velocity of the zone can be subsequently calculated from the spray penetration correlation, and then the amount of air entrained is obtained by the zone momentum conservation. It is assumed that fuel droplets begin to evaporate immediately after break-up occurs. Both heat and mass transfer for a single

evaporating droplet are considered in order to compute instantaneous droplet temperature, rate of evaporation and droplet diameter. The conceptual spray evolution and evaporation progress until ignition are illustrated in Figure 1.2.

The ignition delay is calculated as the delay time from the start of injection until the start of combustion. This delay time includes time for chemical mechanism to produce enough radical pool so the fuel-air mixture can be ignited, as well as mixture preparation time by the physical spray processes such as breakup, air entrainment and evaporation. At the time of ignition, the fuel vapor and air mixture in each zone that was prepared during the ignition delay is burned in the first phase of the combustion. The rate of this initial combustion in each zone is calculated by a pre-mixed combustion model. After all the prepared fuel vapor is consumed, the burning rate is mainly controlled by mixture availability because the physical entrainment and mixing process is much slower than the chemical reaction speed. Figure 1.3 shows the in-cylinder pressure and apparent heat release calculated from a measured pressure trace. Ignition delay and two phases of heat release are clearly recognizable in the figure.

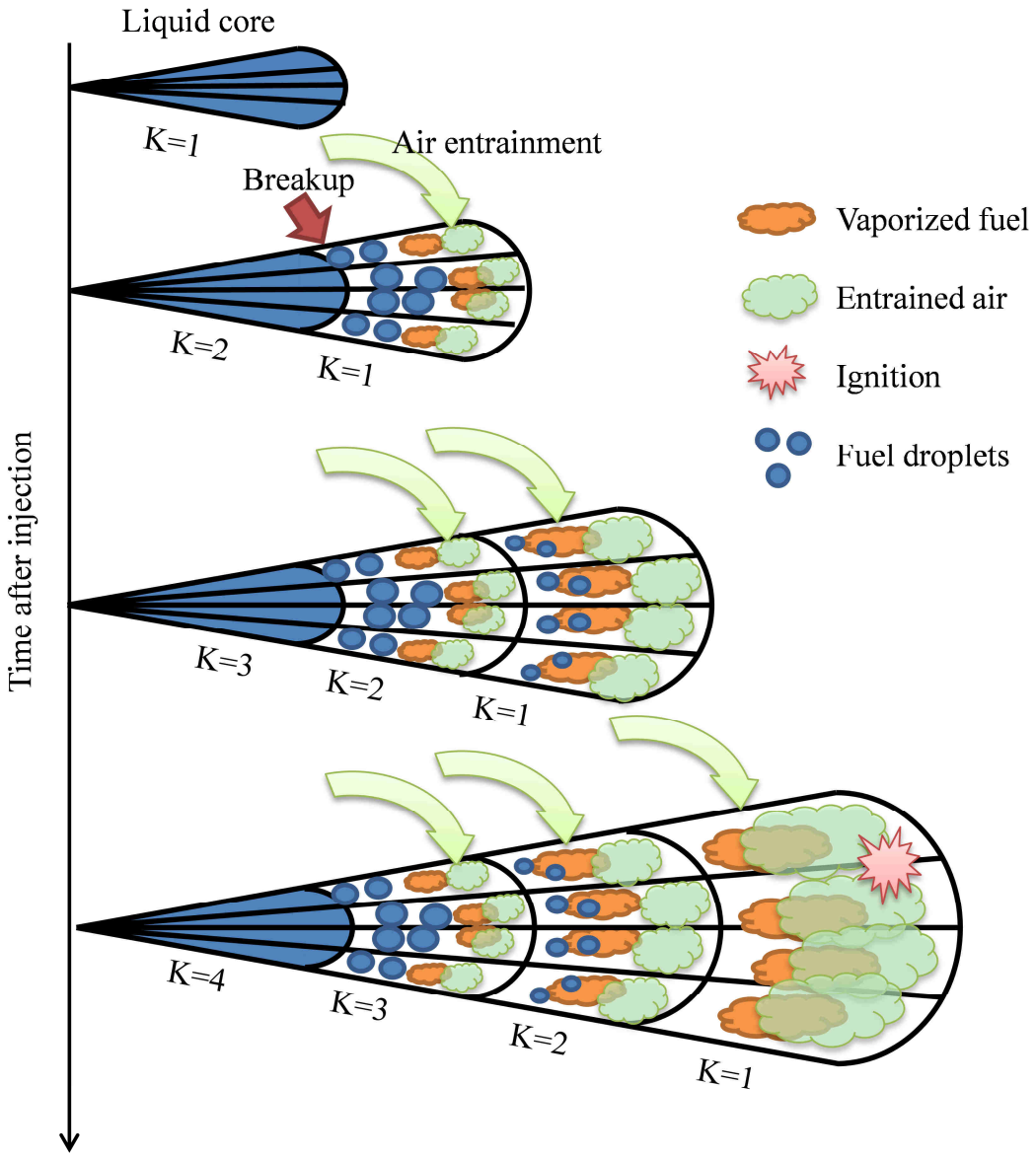

Figure 1.2 Conceptual schematics of spray combustion for DICI engine in quasi-dimensional multi-zone description. K is radial direction zone index

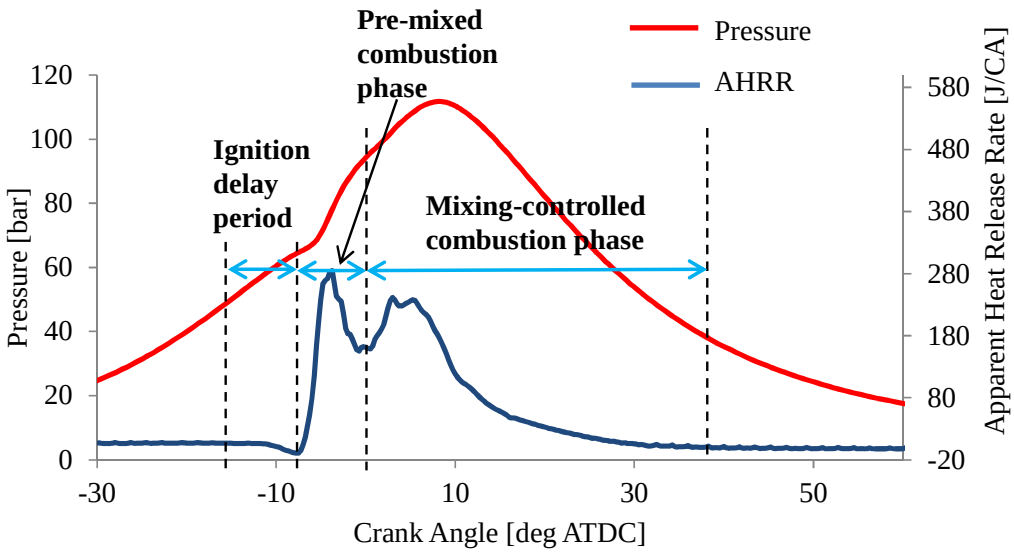

Figure 1.3 Ignition delay and two phases of heat release rate of typical DICI engine

1.3 Literature review

In this section, models from the literature describing DICI combustion are reviewed. The review is mainly focused on the sub models of quasi-dimensional multi-zone combustion models for alternative fuels.

The classic spray penetration correlations of Wakuri *et al.* [18], Dent [19] or Hiroyasu and Arai [15] are the most widely used spray penetration correlations in quasi-dimensional models. However, the only fuel property included in the correlation is the liquid density and the correlation is calibrated for a Diesel spray. In addition to the correlation of Wakuri *et al.* [18] using a spray angle, more recently proposed spray penetration correlations [20–24] also chose the spray angle as a parameter. However, the

spray angle must be predefined from another correlation and calibrated from experiments. In addition, sensitivity to viscosity and surface tension is absent in [20, 21, 24].

The air entrainment can be calculated in two ways. Basically the amount of the air in the spray cone volume is the air entrainment. If both the spray angle and the spray penetration are known, the air entrainment is determined from the spray cone volume and its geometry [15]. Two other well-known correlations for spray angle were developed by Hiroyasu and Arai [15] and Reitz and Bracco [25]. Total entrained air is the amount of air in a spray cone volume, which can be calculated from the tip penetration and the angle of the spray. Siebers [21] developed a spray angle correlation which covers a wide range of ambient conditions. The correlation however is only a function of ambient air density and liquid density. In addition, the model constant must be determined based on the experimental data. This method of calculating the air entrainment can be difficult to implement in a multi-zone spray model due to the unknown distribution of entrained air over the different zones. On the other hand, if the momentum of the spray zone is assumed constant after injection, then, the change of spray velocity can be interpreted as the result of air entrainment [16, 26, 27].

A multi-component evaporation model is desirable for investigating various alternative fuels. The single component droplet evaporation model of Abramzon and Sirignano [28] has been modified and extended to many multi-component applications [29–33]. Each research has a different approach for the multi-component evaporation, but these models except for Burger *et al.* [30] commonly express the evaporation rate for individual species in terms of a fraction of total vaporization rate. The fraction needs to be calculated implicitly which requires an iterative method. Burger *et al.* [30] used the

distillation curve to fit a polynomial of the average molar mass changes during evaporation. Then, the properties used in the model are fitted with the average molar mass. For a given fuel mixture Burger *et al.* pre-computed a table of equilibrium results for some properties as a function of the pressure, temperature, liquid molecular mass and mole fraction in the gas phase for the film around the droplet. However, integrating such models into a quasi-dimensional multi-zone framework is not recommended where a simpler and more computationally efficient model is desirable.

Due to the improved computing power, chemical kinetic mechanisms are used more frequently than before when calculating ignition delay. These mechanisms are built to calculate radical reactions of combustion process of an individual fuel and the ignition delay is a part of these combustion processes. For calculating an ignition delay in a DICI engine, the chemical kinetic mechanism is typically coupled with multi-dimensional computational fluid dynamics simulation. However, even with current computing power, detailed mechanisms are too big for CFD based engine simulation [34] and typically reduced to less than a few hundreds reactions [35, 36].

To achieve computational efficiency, the chemical kinetic mechanism can be further reduced. The Shell ignition model [37] was originally developed to predict knocking of spark ignition engine and used later for a DICI engine because the chemical kinetic mechanism of ignition delay and knocking is the same. Since the mechanism is highly reduced, the shell model needs to be calibrated for a particular fuel. Adjustable parameters can be partially [38] or fully [39] calibrated.

One of the most common methods to calculate the ignition delay is Arrhenius equation type ignition delay models [15, 16, 40–43]. The Arrhenius equation is used to

describe a chemical reaction rate where the inverse of the average rate represents ignition delay time. Activation temperature for the model is an apparent activation temperature because the average rate of reaction is a combination of many different radical reactions. Because the model is simple and a calibration process is much easier than for other models, this type of ignition delay model is widely used for quasi-dimensional multi-zone combustion models [3, 10, 11, 16, 44].

For several decades, many researchers have been studying the Arrhenius equation type ignition delay correlations and applied these to a DICI engine. Numerous ignition delay correlations are based on Wolfer's correlation [45] which has been calibrated for Diesel engines [40], constant volume bombs [15] or gaseous fuel cases [46]. Furthermore the correlation is modified to capture various engine operating situations such as transient engine operation [41], biofuel applications [42], exhaust gas recirculation of Diesel engine [46] or blended hydrocarbon fuels [47]. These correlations are all developed and calibrated to use global averaged engine conditions. Hiroyasu *et al.* [16] developed an ignition delay model of a Diesel engine using local spray information such as temperature and equivalence ratio for a quasi-dimensional multi-zone spray model. This model was extended to recent multi-zone model [44]. In addition, in an effort to capture the ignition quality of different fuels, the Cetane number [11, 42, 47, 48] or the amount of aromatic contents [47] was included in the activation energy for the correlations In spite of all the previous effort made for spray ignition delay, there is still no definitive model which is sensitive to the various fuels and applicable to a wide engine operating range.

Many burn rate models [49–51] used in the quasi-dimensional model are based on a one-step global reaction rate which is expressed with Arrhenius equation including

frequency factor as a function of concentration of fuel and oxidizer. Westbrook and Dryer presented a one-step global reaction rate model for various hydrocarbon fuels [52]. Although their calibration was performed to calculate laminar flame speed, the calibration result clearly shows slow reaction rate with heavier fuels. To capture the two phase heat release rate of DICI engine combustion more precisely, separate burn rate models are used for each phase [3, 13, 53]. The premixed burn rate model is based on one step global reaction rate and the mixing controlled burn rate model is correlated to account for physical preparation of vaporized fuel and air.

Other types of burn rate calculations are often used in quasi-dimensional combustion model as well. Morel and Wahiduzzaman [8] developed a burn rate model with the rich equivalence ratio limit at 3. The model is made to have a maximum burn rate at the equivalence ratio of 1. A simpler way to compute the burning rate of combustion is assuming the burned fuel mass is proportional to the stoichiometric air-fuel ratio [9, 17, 54]. With this model, all the available fuel less or equal to stoichiometric fuel mass is burned in each time step. This model may be too simple to accurately capture the combustion of local spray zones of various fuels and operating conditions. Zhou *et al.* [10] developed a new concept of fuel droplet group combustion model considering collisions and interactions between droplets. In their work the concept of flame surface is introduced in a quasi-dimensional model platform to calculate evaporation and combustion of droplet groups. Although this concept can calculate the DICI combustion accurately, it may be too complex for the quasi-dimensional combustion model. Recently calculation of combustion using chemical kinetic mechanism is also attempted in a quasi-dimensional multi-zone model [55].

A limitation of the existing burn rate correlation is that a new calibration of the model is required for different fuels. When simulating alternative fuels, this could be a critical drawback, especially when the calibration of the model against engine experimental data is not available.

1.4 Objective

For the research and development of a DICI engine with alternative fuel application, fuel sensitive computer model is important. Without fuel property effect in the model, intensive calibration must be done in advance for each fuel and in many cases this is not desirable. Most of the previously developed models reviewed in the previous section are developed based on the Diesel combustion and do not have the ability to distinguish the fuel being used. The present study is focused on developing a fuel sensitive combustion model for a DICI engine using a quasi-dimensional multi-zone modeling framework.

The main goals of this dissertation are to:

- Develop a fuel sensitive DICI combustion model by modifying or develop new sub models: spray formation, evaporation, ignition delay and burn rate.
- Integrate the new sub models in a full engine cycle simulation frame work, which should be fast yet accurate enough to predict engine performance with various fuels.

- Validate and evaluate the developed sub models and the integrated cycle simulation result in various experimental data such as constant volume chamber with engine like conditions and alternative fueled diesel engine experimental data with different engine operating conditions.

The following chapters of the dissertation are organized as follows. The development, validation and evaluation of spray and evaporation model are presented in Chapter 2. In Chapter 3, two newly developed ignition delay models which utilize global and local in-cylinder information respectively are presented. In Chapter 4, a new scaled pre-mixed burn rate model is presented. In Chapter 5 the developed models are integrated into a full cycle engine simulation and the evaluation of the integrated cycle simulation is presented. Chapter 6 summarizes this study and highlights the conclusions and the suggestions for future work.

Chapter 2

Spray and evaporation models for multi-fuel mixtures for direct injection internal combustion engines

In this chapter, direct injection spray and evaporation models during the pre-ignition period in the quasi-dimensional multi-zone Direct Injection Compression Ignition (DICI) engine simulation are presented. The spray penetration, the air entrainment, the spray angle and the multi-component evaporation models are modified based on the models from [3] or newly developed for alternative fuel applications. To confirm the validity of the model, experimental data from the literatures were compared with simulation results. In addition, the model behavior with different fuels has been studied in wide ranges of ambient temperature and pressure.

2.1 Spray Model

The fuel spray is divided into zones as illustrated in Figure 2.1. Fuel injected into the combustion chamber according to the fuel injection schedule forms a parcel during each time step. Then, each fuel parcel is further divided into small zones with equally

distributed mass of fuel in the radial direction. Zone index is assigned according to the zone location in the axial and radial directions of the spray.

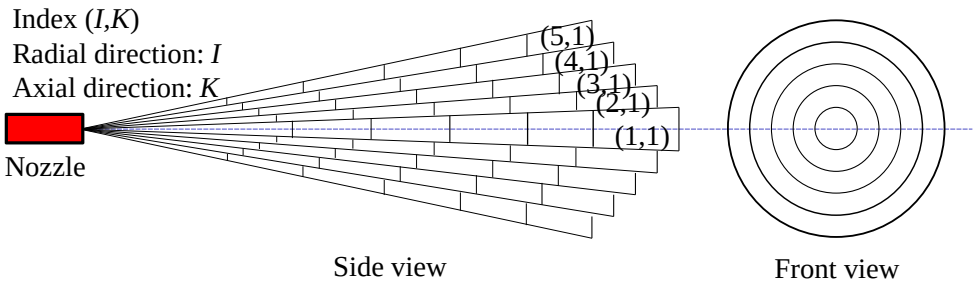

Figure 2.1 Schematic of multi-zone spray concept

2.1.1 Spray penetration and breakup time

A classical spray penetration model for Internal combustion (IC) engines assumes the jet velocity during the pre-breakup period remains constant equal to the initial injection velocity, u_{inj}. After the breakup time, t_b, the spray slows down and its penetration is proportional to the square root of time [15].

$$\begin{cases} S = u_{inj} t & t < t_b \\ S = \beta\sqrt{t} & t \geq t_b \end{cases} \tag{2.1}$$

where β is a proportionality constant

The initial jet velocity is expressed as follows.

$$u_{inj} = C_d \sqrt{2\Delta P / \rho_l} \tag{2.2}$$

The spray penetration at the breakup time is defined as the breakup length, l_b which can be calculated using Eqs. (2.1) and (2.2).

$$l_b = u_b t_b = \beta\sqrt{t_b} \tag{2.3}$$

In Eq. (2.3), the velocity of spray at breakup, u_b, is the same as the initial injection velocity, u_{inj}. Then Eq. (2.1) can be rewritten using Eqs. (2.2) and (2.3). So the generalized spray penetration model can be described as

$$\begin{cases} S = C_d \sqrt{2\Delta P/\rho_l} \cdot t & t < t_b \\ S = C_d \sqrt{2\Delta P / \rho_l} \cdot \sqrt{t_b} \cdot \sqrt{t} & t \geq t_b \end{cases} \tag{2.4}$$

Hiroyasu and Arai [15] used Levich's breakup time model [56] which is derived from the wave stability analysis of the surface of liquid jets.

$$l_b = \zeta \sqrt{\frac{\rho_l}{\rho_a}} d_n \tag{2.5}$$

In their work, the coefficient ζ and the nozzle discharge coefficient, C_d, are fitted to the experiment.

$$\begin{aligned} \zeta &= 15.8 \\ C_d &= 0.39 \end{aligned} \tag{2.6}$$

Jung [3] modified this correlation using an actual nozzle discharge coefficient.

$$\zeta = \frac{2.95^2}{2^{0.5} C_d} = \frac{6.15}{C_d} \tag{2.7}$$

These models are extensively used in recent multi-zone combustion simulations. However, the only sensible fuel properties of these models is the liquid fuel density because the spray penetration models relies on the breakup model described in Eq. (2.5). Other properties such as viscosity and surface tension of the liquid fuel are also important to describe breakup phenomena. Detailed breakup phenomena and its mechanisms are well reviewed in Faeth et al. [57] and Chryssakis [58]. More detailed breakup models incorporating viscosity and surface tension can be found in many CFD applications.

Among the various models the WAVE breakup model [59] is a simple alternative breakup time calculation model. This model starts with the same stability analysis of liquid jet surface wave as Levich's model. Instead of deriving a correlation based on many assumptions, the numerical solution of the analysis is calculated and curve fitted. The wave growth rate, Ω, and the corresponding wave length, Λ, are correlated with non-dimensional parameters. These non-dimensional parameters are calculated for the liquid jet with velocity, u and initial blob radius, a.

$$\Omega\left(\frac{\rho_l a^3}{\sigma}\right)^{0.5} = \frac{0.34 + 0.38We_g^{1.5}}{(1+Oh)(1+1.4X^{0.6})}$$
$$\frac{\Lambda}{a} = 9.02\frac{(1+0.45Oh^{0.5})(1+0.4X^{0.7})}{(1+087We_l^{1.67})^{0.6}} \tag{2.8}$$

where

$$Oh = \frac{We_l^{0.5}}{\mathrm{Re}_l},\ X = Oh \cdot We_g^{0.5}$$
$$We_l = \frac{\rho_l u^2 a}{\sigma},\ We_g = \frac{\rho_g u^2 a}{\sigma},\ \mathrm{Re}_l = \frac{ua}{\nu_l}$$

Using the wave growth rate and the corresponding wave length, the child droplet radius, r, its parent blob radius, a, and characteristic breakup time, τ, are described as follows.

$$r = B_0\Lambda \qquad B_0\Lambda \le a$$
$$r = \min\begin{cases}(3\pi a^2 u / 2\Omega)^{0.33} \\ (3a^2\Lambda / 4)^{0.33}\end{cases} \qquad B_0\Lambda > a \tag{2.9}$$

$$\frac{da}{dt} = -\frac{a-r}{\tau} \tag{2.10}$$

$$\tau = \frac{3.726 B_1 a}{\Lambda \Omega} \tag{2.11}$$

where B_0 is the model size constant, typical value is 0.61 and B_1 is the model time constant which depends on the injector characteristics.

In the multi-zone simulation context, the liquid jet temperature is assumed to be constant as well as the velocity of the spray in the pre-breakup region. The velocity, u, in Eq.(2.8) can be the velocity of the zone before breakup. The rate growth rate and the corresponding wave length are also constant under the assumptions. Therefore, Eqs. (2.10) and (2.11) are constant and characteristic breakup time can be considered as the breakup time of the spray. By setting the initial blob size the same as the nozzle diameter, d_n, the breakup time can be expressed as

$$t_b = \frac{3.726 B_1 d_n}{\Lambda \Omega} \tag{2.12}$$

In Figure 2.2 the variation of the WAVE breakup time is shown as function of viscosity and surface tension. Surface tension and viscosity shows opposite effects on the breakup time.

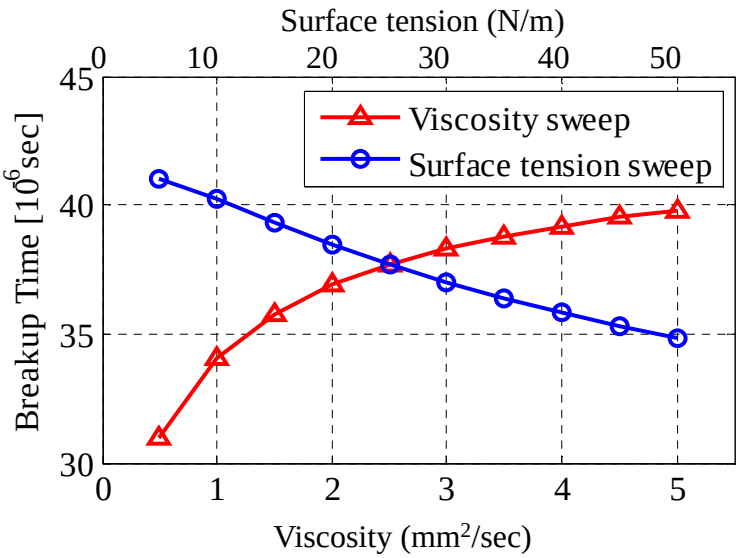

Figure 2.2 Breakup time calculation of WAVE breakup model varying viscosity and surface tension for ΔP=1100 bar and fuel density of 841 kg/m^3 for both cases. For surface tension sweep, viscosity is fixed at 2.5 mm^2/sec. For viscosity sweep, surface tension is fixed at 25 mN/m.

2.1.2 Zone to zone interaction in the spray model

In the multi-zone spray model environment, the spray penetration is calculated for each zone. The zone velocity is constant in the pre-breakup region and equals the initial injection velocity. However the injection process is transient in a real engine with a variable injection rate profile over time. The early injection with small lift creates slower injection velocities followed by higher lifts with higher injection velocities. If zone to zone interaction is not considered during the breakup period, the transient injection rate causes zone overlapping in the spray particularly in the liquid phase of the jet. This is not physically permissible.

To resolve this problem a new penetration concept is developed for the pre-breakup region. At the start of injection, the initial velocity, which is calculated from the injection profile, of the leading zone is slower than the velocity of the subsequent zone.

Since the zones are parts of the continuous liquid core of the fuel spray and the internal circulation motion of fuel jet is neglected in this framework, it is reasonable to assume that a faster zone pushes zone in front and both zones have the same velocity. This zone to zone interaction during the pre-breakup period is modeled by applying a momentum conservation law. The new velocity for the liquid core is updated whenever new zones are injected using the momentum conservation.

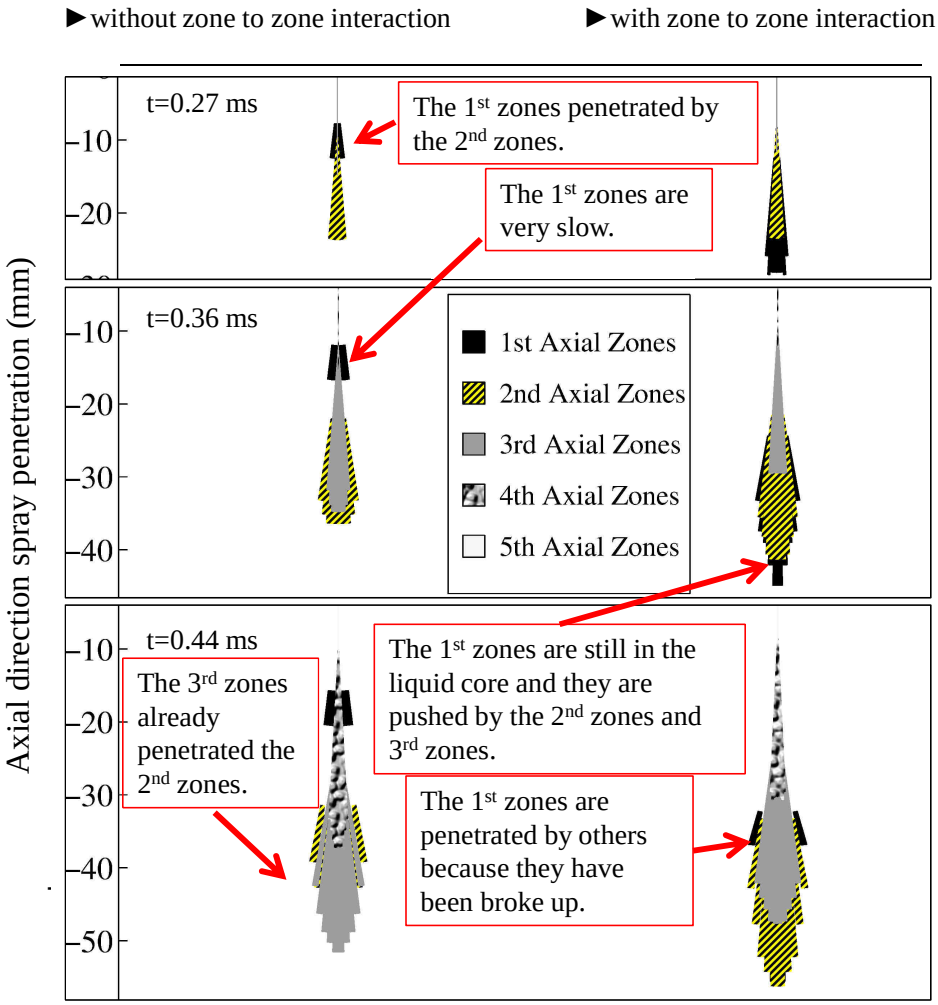

Figure 2.3 Schematics of zone interaction concept. Left: the classical model without zone to zone interaction, Right: the new model with zone to zone interaction.

Figure 2.3 shows the concept of zone to zone interaction. The figure compares two spray penetration models without and with zone to zone interactions. On the left, the

classical model calculation without zone interaction is illustrated. The 1st zones of spray show slowest penetration because the injection profile begins with a transient slope. The 1st zones are falling behind and penetrate separately. However with zone interaction model on the right, the 1st zones are pushed by the following zones. Therefore the zones within the liquid core stay together and the average velocity is calculated from the total momentum. However, after the 1st zones break up, they are allowed to be penetrated by the following liquid core zones. The 1st zones gained enough speed and the separation from the other spray is minimal.

After the breakup of the liquid core, the zone to zone interaction with direct pushing assumption is not valid, because droplets are colliding with each other and trajectories of each droplet are significantly different. In the multi-zone simulation environment, individual trajectories of droplets are not traced and the initially distributed fuel always stays in the zone. In this approach, only zones remaining in the liquid core state before breakup participates in momentum conservation for the calculation of injection velocity. After breakup the zone trajectory follows the penetration correlation.

The initial zone velocity is calculated from a given injection mass flow rate profile.

$$u_z(I,K) = u_{inj}(K) = \frac{\dot{m}_{parcel}(K)}{\rho_l A_n} \tag{2.13}$$

where $\dot{m}_{parcel}(K)$ is mass flow rate of *K*-th parcel obtained from the injection profile. The mass flow rate of each zone is evenly distributed for radial direction zones.

$$\dot{m}_f(I,K) = \frac{\dot{m}_{parcel}(K)}{I_{\max}} \tag{2.14}$$

The difference between injection pressure and ambient pressure is expressed as follows.

$$\Delta P(K) = \frac{1}{2\rho_l}\left(\frac{\dot{m}_{parcel}(K)}{C_d A_n}\right) \tag{2.15}$$

The liquid core velocity is calculated by momentum conservation.

$$u_{core} = \frac{\sum_{I=1}^{I_{\max}} \sum_{K=K_{tip}}^{K_{\max}} \left(\dot{m}_f(I,K) \cdot u_z(I,K)\right)}{\sum_{I=1}^{I_{\max}} \sum_{K=K_{tip}}^{K_{\max}} \dot{m}_f(I,K)} \tag{2.16}$$

The zone velocity, $u_z(I,K)$ of all the existing liquid zones is assigned as the core velocity u_{core} in the pre-breakup region. If the breakup time of the zone is reached, the spray velocity at breakup, $u_b(I,K)$ is assigned as u_{core} at that time.

The breakup time of each zone in a parcel linearly decreased in radial direction according to zone geometry. The correction factor is multiplied to the breakup time calculated in Eq. (2.12) for each zone.

$$t_b(I,K) = \frac{I_{\max} - (I - 0.5)}{I_{\max}} t_b \tag{2.17}$$

where $I_{\max}$ is maximum number of zone in radial direction.

Combining the WAVE breakup time in Eq. (2.17) with the spray penetration correlation in Eq. (2.4) the final form of spray penetration is expressed as

$$\begin{cases} S(I,K) = \left(\dfrac{\sum_{K=K_{tip}}^{K_{max}} \left(\dot{m}_f(I,K) \cdot u_z(I,K) \right)}{\sum_{K=K_{tip}}^{K_{max}} \dot{m}_f(I,K)} \right) t & t < t_b(I,K) \\ S(I,K) = u_b(I,K) \sqrt{\dfrac{3.726 B_1 d_n}{\Lambda \Omega}} \sqrt{t} & t \geq t_b(I,K) \end{cases} \tag{2.18}$$

2.1.3 Air entrainment

The air entrainment to each zone is calculated with a momentum conservation concept [16] with additional details in [3]. The initial momentum of the zone at the breakup is equal to the momentum of the zone at any subsequent distance traveled. The outer zones have shorter penetration than inner zones which leads to higher entrainment rate. The shorter penetration of outer zone is a result of the shorter breakup time. The velocity of zones slows down after the breakup, so that the total momentum in the each zone is kept constant by the amount of air entrained.

$$m_f(I,K) \cdot u_b(I,K) = \left(m_a(I,K) + m_f(I,K) \right) \frac{dS(I,K)}{dt} \tag{2.19}$$

By balancing the initial momentum of the spray zone and the momentum of the zone at any instance, the air entrainment of the zone can be obtained.

$$\dot{m}_a(I,K) = m_f(I,K) \cdot \left(u_b(I,K) \cdot \frac{dS(I,K)}{dt} - 1 \right) \tag{2.20}$$

By differentiating Eq. (2.19) the rate of air entrainment is obtained.

$$\dot{m}_a(I,K) = -\frac{m_f(I,K)\cdot u_b(I,K)}{\left(dS(I,K)/dt\right)^2}\frac{d^2S(I,K)}{dt^2} \tag{2.21}$$

2.2 Evaporation model

The model for single-component droplet evaporation is extended to multi-component fuels. To reduce computational expense, the fuel mixture in the droplet is assumed to be a pseudo-single component fuel. The mass fraction of each component is then recovered using Raoult's law (ideal solution) and the new liquid composition is calculated as the droplet evaporates. This also assumes that the liquid drop has a uniform distribution of species so the uneven evaporation rate of different components of the fuel does not lead to diffusional effects. For very small droplets this is a reasonable assumption but could be important for low diffusivities and high evaporation rates.

2.2.1 Single-component droplet evaporation

The droplet evaporation model calculates the rate of vaporized mass transfer from the liquid droplet to the air. The temperature of liquid droplet is increased by the heat transfer from the surrounding air as shown in Figure 2.4.

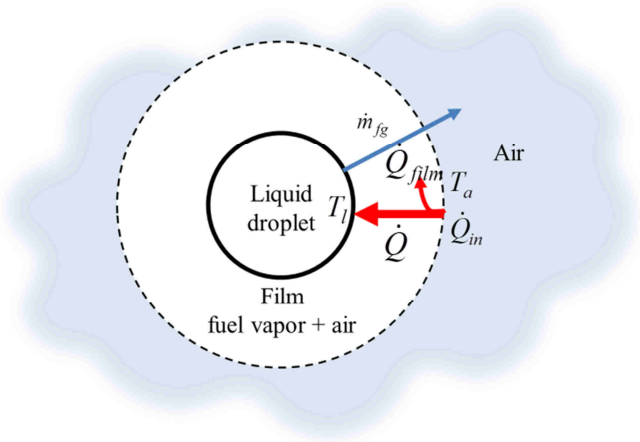

Figure 2.4 Schematic of evaporating fuel droplet

The classical droplet evaporation model [28] using Spalding mass transfer number B_M is expressed as

$$\frac{dm_l}{dt} = -\pi d_l D Sh \rho_m \ln(1 + B_M) \tag{2.22}$$

where d_l is the liquid diameter, D is the binary diffusion coefficient, Sh is the Sherwood number and ρ_m is density of the fuel vapor and gas mixture in the film.

The exact temperature and fuel vapor fraction profiles in the film are too complicated to model in the simplified evaporation model. All the gas phase properties are evaluated at the film conditions. The mean temperature and fuel vapor fraction of the film are expressed from an assumed profile (variation) through the layer as follows.

$$\begin{aligned} T_m &= T_l + \frac{T_\infty - T_l}{3} \\ x_{f,m} &= x_{v,s} + \frac{x_{v,\infty} - x_{v,s}}{3} \end{aligned} \tag{2.23}$$

where x is mass fraction. The subscripts indicate as follows; v indicates vapor, f indicates fuel, s indicates surface and ∞ indicates ambient condition far enough from droplet.

The Spalding mass transfer number is defined from following equation.

$$B_M = \frac{x_{v,s} - x_{v,\infty}}{1 - x_{v,s}} \tag{2.24}$$

The heat transfer from the surrounding air to the droplet is calculated from the following equation by El Wakil et al. [60].

$$\dot{Q} = \pi d_l^2 h(T_a - T_l)\left(\frac{z}{e^z - 1}\right) \tag{2.25}$$

where z is given by

$$z = \frac{C_{p,m}}{\pi d_l k_m Nu}\frac{dm_{fg}}{dt} \tag{2.26}$$

Equation (2.25) is derived considering the amount of the energy required for heating the film. The heat transfer coefficient, $h = k_m Nu / d_l$ in Eq. (2.25) is calculated for non-evaporating condition. To include the evaporation effect on the heat transfer, a correction factor, $z/\left(e^z - 1\right)$ is added as in Eq. (2.25). The evaporating fuel is mixed with the air in the film, and then diffuses out to the air. Both the air and the fuel vapor in the film are heated by heat transfer from the air as shown in Figure 2.4To account for both fuel and air in the film under mean condition in Eq. (2.23) using the heat capacity of the film, $C_{p,m}$ instead of the fuel vapor, $C_{p,v}$ in Eq. (2.26) is considered to be more appropriate. All properties and non-dimensional numbers in Eqs. (2.25) and (2.26) are calculated at the film condition. Nusselt number and Sherwood number are calculated using the well-known empirical correlations [61].

$$\begin{aligned} Nu &= 2 + 0.6\,\mathrm{Re}_d^{1/2}\,\mathrm{Pr}^{1/3} \\ Sh &= 2 + 0.6\,\mathrm{Re}_d^{1/2}\,Sc^{1/3} \end{aligned} \tag{2.27}$$

Equation (2.27) is further modified by Arbramzon and Sirignano [28] to consider the Stefan flow effect which thickens the laminar boundary layer.

$$Nu^* = 2 + \frac{Nu - 2}{f(B_T)}$$
$$Sh^* = 2 + \frac{Sh - 2}{f(B_M)} \tag{2.28}$$

where, $B_T = (1 + B_M)^{\chi} - 1$, is the Spalding heat transfer number and

$$\chi = \left(\frac{c_{p,v}}{c_{p,a}}\right)\left(\frac{Sh^*}{Nu^*}\right)\frac{1}{Le}.$$

The modifying factors $f(B)$ are given by

$$f(B) = (1+B)^{0.7}\,\frac{\ln(1+B)}{B} \tag{2.29}$$

where B is the corresponding Spalding transfer number.

The temperature of the liquid droplet is given by solving the droplet energy balance.

$$m_l C_{p,l}\frac{dT_l}{dt} = \dot{Q} + \lambda\frac{dm_l}{dt} \tag{2.30}$$

where λ is heat of evaporation (h_{evap})

2.2.2 Extension to multi-component droplet evaporation

For a computer simulation, the fuel properties of wide range of temperature and pressure are required and they are not readily available. Therefore a multi-component fuel surrogate is often used for computer simulation.

To maintain low computational load of multi-component evaporation model, a fuel mixture is treated as a single component droplet with properties of the mixture. The concentrations of each component are calculated by Raoult's law which gives vapor-liquid equilibrium in the film of the droplet. This concept for droplet evaporation of fuel spray is based on the following assumptions.

First of all, a well-mixed liquid droplet is assumed so that the Soret effect can be ignored. Secondly, spatial distribution inside the droplet is assumed to be negligible. In addition, ideal gas and ideal solution are assumed. Therefore, Raoult's law is applied to calculate Spalding mass transfer number for the fuel mixture. Lastly, the multi-component fuel species are assumed to diffuse into air, thus a simple binary diffusion coefficient is used.

Since the fuel species are diffused only into air, total fuel vapor flux in the radial direction becomes the summation of binary species fluxes defined by Fick's first law.

$$-J = -\sum_{i=1}^{n} J_i = \sum_{i=1}^{n} D_i \frac{\partial c_i}{\partial r} = D_m \frac{\partial c}{\partial r} \tag{2.31}$$

where J is diffusion flux in mol/(m^2·s), D is diffusion coefficient in m^2/s, c is molar concentration in mol/m^3. The subscripts indicate as follows; i indicates species, n indicates number of total species and m indicates mean value at film condition.

Species mole fraction, y_i can be calculated from their concentration and the mean binary diffusion coefficient is expressed as

$$D_v = \sum_{i=1}^{n} D_i y_i \tag{2.32}$$

Using Raoult's law the mass fraction of fuel vapor (includes all fuel components), x at the surface (film) for Eq. (2.24) is calculated from following equations.

$$
\begin{aligned}
P_{vap} &= \sum_{i=1}^{n} y_{i,l} P_{sat,i} \\
y_{v,s} &= \frac{P_{vap}}{P} \\
x_{v,s} &= y_{v,s} \frac{M_{v,s}}{M_{avg,s}}
\end{aligned}
\tag{2.33}
$$

where P_{vap} is vapor pressure of mixture, P_{sat} is saturated vapor pressure and M is molar mass.

The liquid droplet composition is can be calculated using mass conservation of each component. The instantaneous mole fractions of vapor fuel components leaving the droplet at the surface are obtained using Raoult's law.

$$
y_{i,v} = \frac{y_{i,l} P_{sat,i}}{\sum_{i=1}^{n} y_{i,l} P_{sat,i}} \tag{2.34}
$$

where subscript l indicates liquid.

2.2.3 High pressure effect on the fuel vapor

The compressibility of the fuel vapor is considered to calculate the real vapor density at the film. In the film of a droplet, the vapor and the liquid fuel are in equilibrium. Thus a simple corresponding state principal (CSP) method for the compressibility of saturated vapor can be used [62]. For the mixture fuel, the pseudo critical properties such as critical temperature, critical pressure and critical compressibility using Kay's rule [63] are used to calculate the mixture compressibility.

$$
Z_m = Z_m^0 + \omega_m Z_m^1 \tag{2.35}
$$

where Z is compressibility factor and ω is acentric factor.

Then the partial density of the fuel mixture at the film is given by

$$\rho_m = \frac{x_{v,s} PM_{v,s}}{Z_m RT_m} \tag{2.36}$$

Kay's rule in connection with a general equation of state as Lee-Kesler can provide the compressibility factor if not known as well as the fugacity for the liquid phase of the fuels. Such an extension would increase the complexity but make the model more accurate compared to Raoult's rule and ideal solution assumption.

2.2.4 Initial droplet size calculation

At the breakup time, the droplet size distribution is neglected and all the droplets are assumed to have the same size. The initial droplet size is calculated using a Sauter mean diameter (SMD), d_{32} correlation proposed by Estes and Mudawar [64].

$$\frac{d_{32}}{d_n} = 3.67\left[We_d^{0.5}\,\mathrm{Re}_d\right]^{-0.259} \tag{2.37}$$

where

$$We_d = \frac{\rho_a u_b^{\,2} d_n}{\sigma},\ \mathrm{Re}_d = \frac{\rho_l u_b d_n}{\mu_l}$$

and d_n is nozzle diameter.

2.3 Results and discussion

2.3.1 Spray penetration model validation

To validate the new penetration model with the integrated WAVE breakup model, experiment data with three different fuels are collected from the literature [65]. The experiment measured spray penetrations of Diesel, soybean BioDiesel and dimethyl ether (DME) in a common rail injection system under atmospheric conditions. Injection rate of each fuel is illustrated in Figure 2.5 and the properties of fuels are listed in Table 2.2

Table 2.1 Test fuel properties at 293 K, 0.1 MPa

	Diesel	BioDiesel (Soybean)	DME
Density (kg/m^3)	828	884	660
Viscosity (mm^2/s)	2.835	4.022	0.12-0.15
Surface tension (kg/s^2)	0.027	0.028	0.012

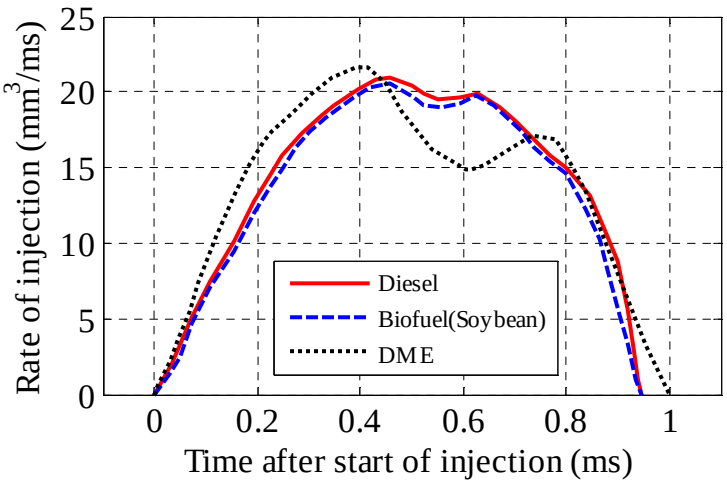

Figure 2.5 Volumetric injection rate profiles for the test cases. The mass injection rate is converted to the volume injection rate to identify the differences between the three fuels more intuitively.

The parameter of the WAVE breakup time, B_1, is calibrated as 12.5 to match the calculated spray penetration with Diesel fuel experimental data. A comparison of other two fuels using new model is illustrated in Figure 2.6 (a). In the experimental results, higher viscosity of BioDiesel causes a longer breakup time and results in longer penetration. For DME fuel, low surface tension causes longer breakup length and spray penetration. However, the effect of low viscosity overwhelms this effect and results in short penetration. Figure 2.6 (b) shows a comparison of the penetration model from our base framework [3] using Eqs. (2.4), (2.5) and (2.7). The model employs classical Levich's breakup model and has no interaction model between spray zones. In the comparison the new spray model matches the spray penetration better than the base model. Especially, the new model can capture the shorter penetration length of the DME. In the pre-breakup region, the DME case shows slightly higher penetration, which is due to the higher injection rate of the DME. The penetration result of the base model does not distinguish three different fuel injections well enough to reproduce the experimental data. Overall, the penetration of DME is more distinguishable from others due to its extremely low viscosity and surface tension.

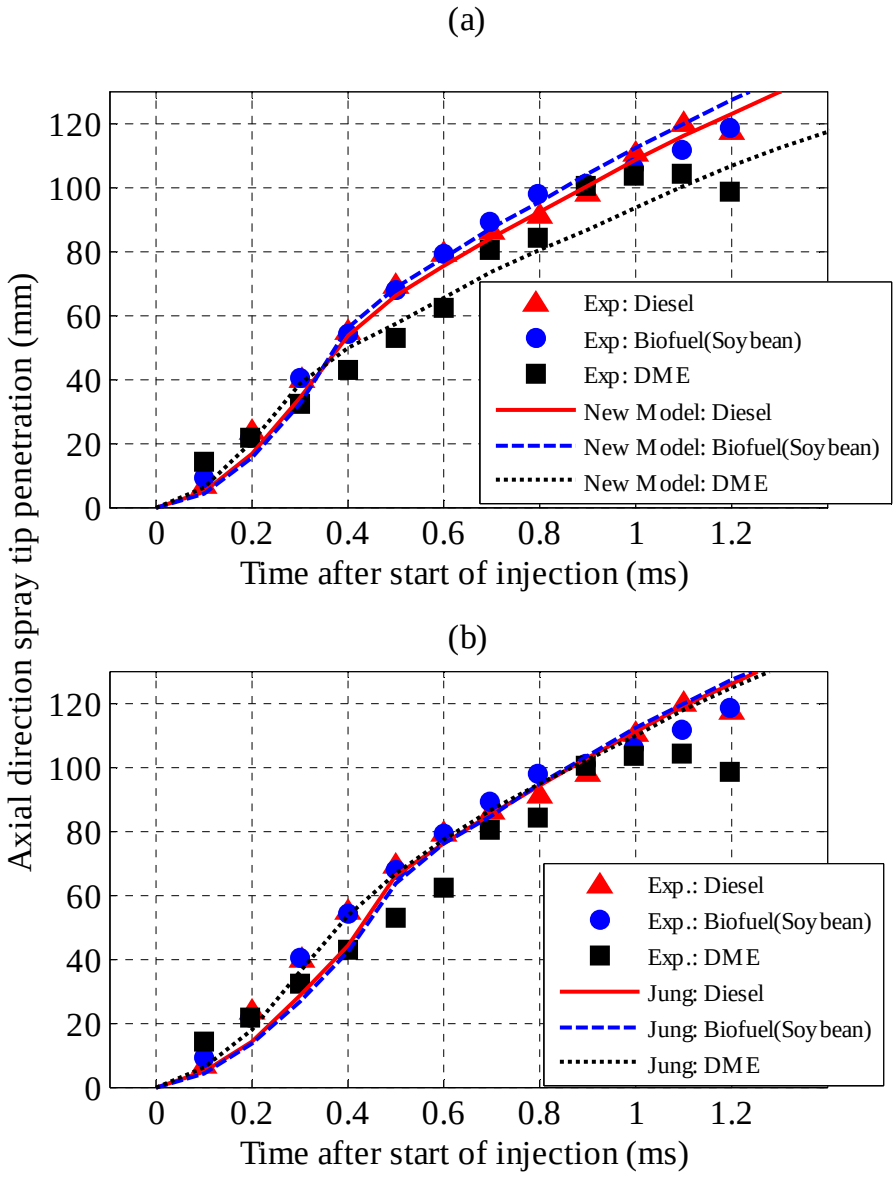

Figure 2.6 Comparison of spray penetration with experiment using (a) new model and (b) base model for injection pressure of 60 MPa with 0.3 mm of nozzle size, ambient temperature of 293 K and ambient pressure of 0.1 MPa.

Another comparison is made using experimental data from [66]. The experiment compared spray penetration of Diesel fuel #2 (DF2) and JP8 in the constant volume chamber at 21% O_2 molar concentration. The estimated fuel property at 373 K for the simulation is listed at Table 2.2. The calibrating parameter *B1* is calibrated as 10.0. In Figure 2.7, a comparison of experiment data and the proposed model is presented for both

fuels. The results of simulation and experiment have a good level of agreement. In fact, the spray penetrations of two different fuels are very close to each other in this case. Since the physical fuel property of DF2 and JP8 is relatively similar compared to previous comparison, the calculation results as well as experiment data are almost the same. The slight over prediction in the later part of the penetration is due to the combustion of the spray.

Table 2.2 Estimated fuel properties at 373 K, 0.1 MPa

	DF2	JP8
Density (kg/m^3)	778	750
Viscosity (mm^2/s)	1.80	1.05
Surface tension (kg/s^2)	0.0172	0.0150

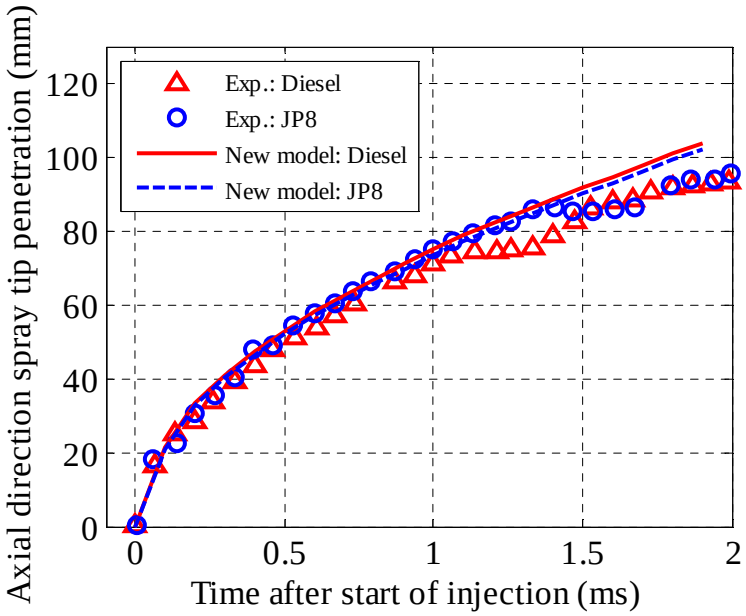

Figure 2.7 Comparison of spray penetration with DF2 and JP8 for injection pressure of 110 MPa with 0.18 mm nozzle diameter, ambient temperature of 850 K, and ambient density of 14.8 kg/m^3.

2.3.2 Air entrainment model validation by spray angle comparison

The air entrainment into the spray cannot be directly measured form the experiment or extremely difficult if possible. However, the total air entrainment can be considered as the total air inside of the spray cone volume. In this study, the spray penetration and the air entrainment are calculated from the model described in Eqs. (2.18) and (2.21). The spray angle can be calculated from those by assuming simple geometrical shape of the spray as shown in Figure 2.8. The spray is considered to be composed with two cones, one from the injector tip with the length of *S(5,1)* and the other with the length of [*S(1,1)-S(5,1)*]. The volume of two cones is equal to the sum of the individual volumes of the zones.

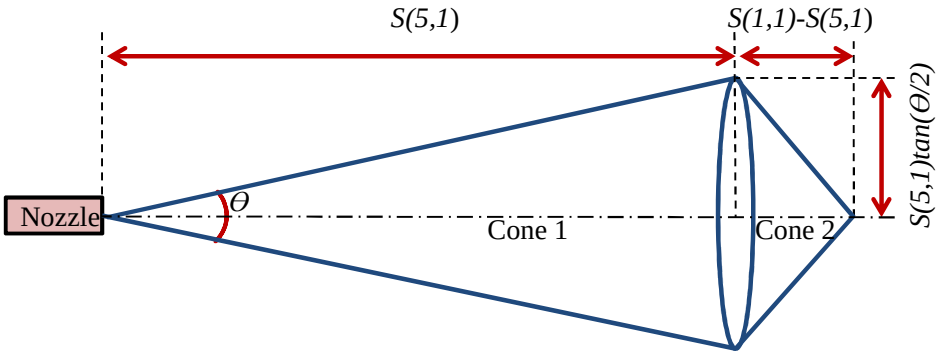

Figure 2.8 Geometry of spray cone

$$V_{spray} = \sum V_z = V_{cone1} + V_{cone2} = \sum_{t=t_b}^{t} m_z(t) \Big/ \rho_z$$
$$= \frac{\pi}{3}\left[S(5,1) \cdot \tan\left(\frac{\theta}{2}\right)\right]^2 \cdot \left(S(5,1) + [S(1,1) - S(5,1)]\right) \quad (2.38)$$

Then, the spray angle can be calculated from the spray penetration and air entrainment as follows.

$$\theta = 2\arctan\left(\frac{1}{S(5,1)} \sqrt{\frac{3}{\pi}\left(\sum_{t=t_b}^{t} m_z(t) \right) \Big/ \left(S(1,1)\rho_z \right)} \right) \tag{2.39}$$

Since the spray penetration is validated in the previous section, a comparison of this spray angle with experimental results can be used to validate the model accuracy of air entrainment. Experimental data of spray angle measured from the same experiment setup [66] in Figure 2.7 for Diesel fuel #2 (DF2) and JP8 fuels is compared with the calculated spray angle. In addition, other commonly used spray angle correlations are also compared for the reference. The other two spray angle correlations are given as follows.

Hiroyasu and Arai [15]

$$\theta = 0.05\left(\frac{\rho_a \Delta P d_n^2}{\mu_a^2} \right)^{0.25} \tag{2.40}$$

Reitz and Bracco [25]

$$\begin{aligned} \tan\left(\frac{\theta}{2} \right) &= \frac{1}{A} 4\pi \left(\frac{\rho_g}{\rho_l} \right)^{0.5} \frac{\sqrt{3}}{6} \\ A &= 3.0 + 0.28\left(\frac{l_n}{d_n} \right) \end{aligned} \tag{2.41}$$

Figure 2.9 shows the comparisons of spray angle calculation over time. Hiroyasu and Arai correlation given as Eq. (2.40) over-predicted the spray angle and Reitz and Bracco correlation given as Eq. (2.41) under-predicted the spray angle. The results from the momentum conservation method, given as Eq. (2.40), match the experimental data better than the other two correlations in the later part of injection while the other two correlations give constant values. The comparison result implies that the air entrainment model using momentum conservation method is reasonably valid.

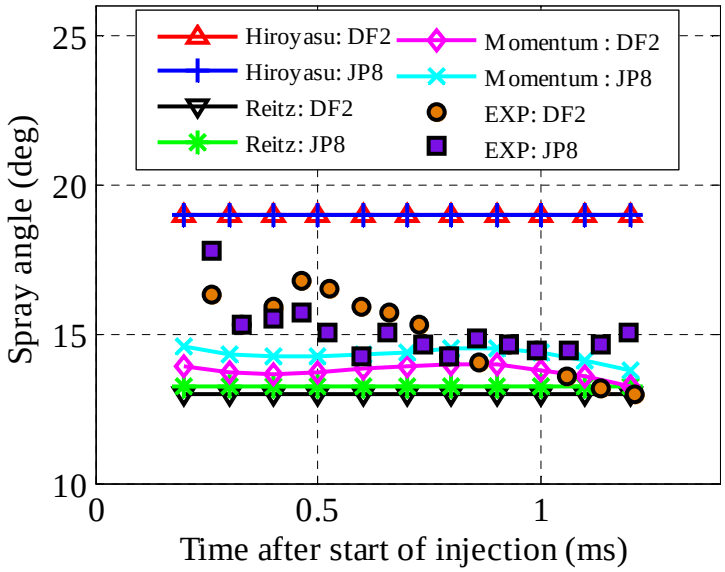

Figure 2.9 Comparison of spray angle models with experiment. The test fuels were injected at 110 MPa to air in the high pressure vessel at the ambient temperature and the density of 850 K and14.8 kg/m3 respectively.

2.3.3 Droplet evaporation model validation

The evaporation model is compared with experimental data from three literatures. Nomura et al. [67] measured n-heptane evaporation time at the atmospheric pressure in a microgravity environment and with no convective flow. Gökalp et al. [68] showed

evaporation characteristic of the binary mixture of n-heptane and n-decane with two different blend ratio at the atmospheric pressure. Lastly experimental data from Stengele et al. [29] provides the evaporation time and the velocity with free-falling binary mixture of the n-pentane and n-nonane droplet under high pressure condition.

Figure 2.10 shows a comparison of evaporating n-heptane droplet history with two different ambient temperatures at the atmospheric pressure. In this case there is no convective flow thus it is a limiting case for an evaporating droplet [61] and the Nusselt number becomes 2.0. The computed droplet history shows good agreement with the experiment data at 648 K, but slightly slower evaporation at 471 K.

Figure 2.11 shows a n-heptane and n-decane mixture evaporation comparison with two different blend ratios. In the comparison, both the models calculated under-predicted results at the latter stage of evaporation. The experiment was performed using a suspended droplet and the suspension is not considered in the calculation. Thus the effect from the support might be the cause of a different evaporation rate in the later part where the droplet becomes small as it evaporates and the effect of suspender becomes dominant. In the experiment shown in Figure 2.10 was also performed with a suspended droplet, however the size of the suspender in the experiment is relatively small: 0.15 mm diameter silica fiber verses 0.2 mm diameter with 0.4 mm diameter at tip. Therefore the effect of suspender is small for Figure 2.10.

The result of freely falling droplet case in Figure 2.12 shows that the presented evaporation model performs well in high ambient pressure condition. For the evaporation model, the velocity of the free falling droplet is calculated according to the method presented in Stengele et al.[29]. The gravity force, the buoyance force and the drag force

of the droplet are considered. The velocity of freely falling droplet accelerated in the beginning because the initial velocity of droplet is 0.45 m/s and the drag coefficient of droplet decreases as it evaporates. It is because the relative velocity of surrounding gas and droplet becomes small [28, 69].

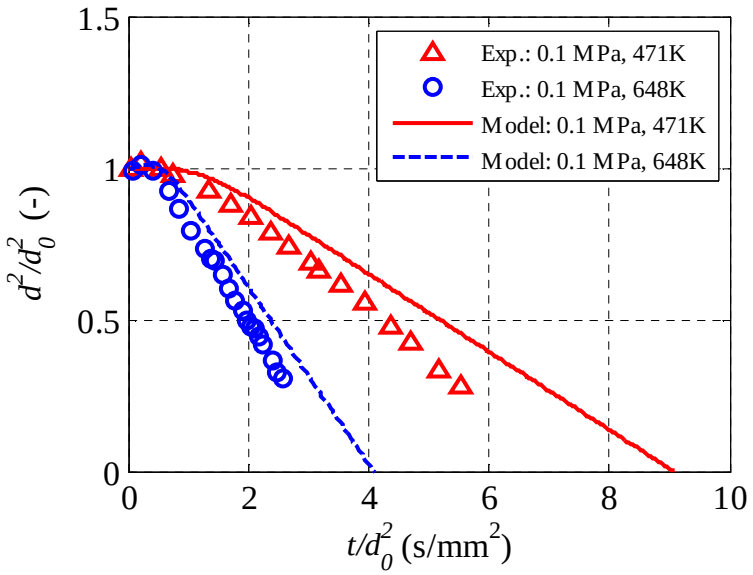

Figure 2.10 Comparison of single component fuel evaporation calculation with experiment data. d^2/d_0^2 indicates regression of the non-dimensional droplet surface and t/d_0^2 indicates the time normalize by the square of initial droplet size. Experiment data is obtained from Nomura et al.[67].

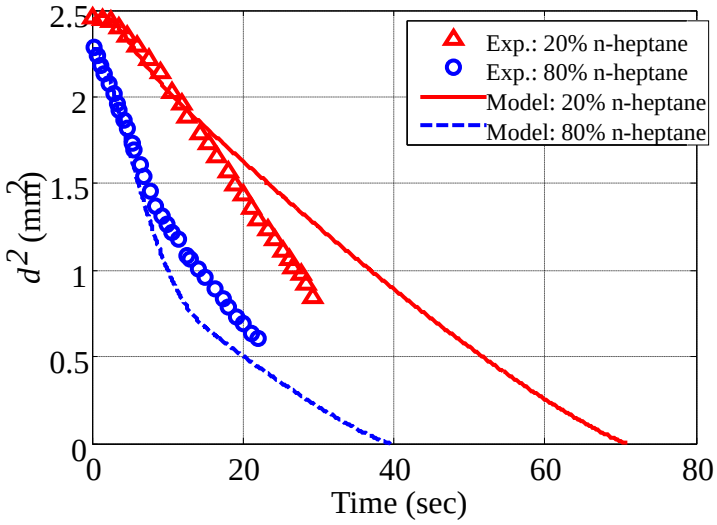

Figure 2.11 Comparison of multi-component fuel evaporation calculation with experiment data. d^2 indicates regression profile of the droplet surface. Experiment data are obtained from Gökalp et al.[68]. Ambient pressure of 0.1 MPa, ambient temperature of 372 K and External flow velocity of 1.45 m/s are used.

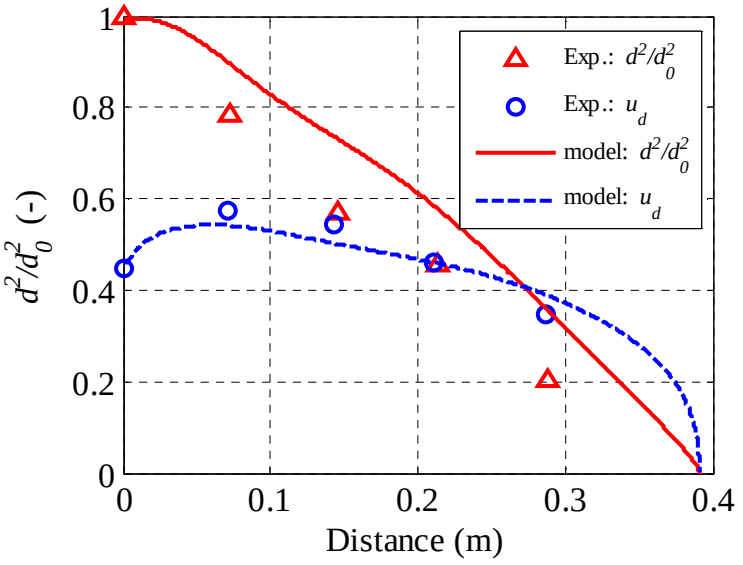

Figure 2.12 Comparison of multi-component fuel evaporation calculation with experiment data. u_d in the second y-axis indicates the velocity of the droplet.. Experiment data are obtained from Stengele et al.[29]. Ambient pressure of 4 MPa and ambient temperature of 550 K are used. Initial droplet temperature is 400 K.

2.3.4 Liquid length comparison

The penetration length of the zone, which has remained liquid fuel and is the furthest from the tip, is defined as the liquid length. The calculated liquid length is a combined result of jet penetration, breakup, zone to zone interaction and evaporation. The experimental data for DF2 and JP8 are taken from the literature [66]. The estimated fuel properties at 436 K of DF2 and JP8 are used for spray penetration and breakup. Multi-component surrogates are used for the evaporation. A mixture of 49 % n-tetradecane, 30 % n-decane and 21 % 1-methyl naphthalene in mass basis is used for DF2 [70]. A mixture of 18 % n-tetradecane and 82 % n-dodecane in mass basis is used [71] for JP8.

Figure 2.13 and Figure 2.14 show comparisons of the liquid length at various ambient temperatures and densities. The experiment results show that the liquid lengths of JP8 are 10-15 % shorter than DF2 [66]. For DF2, simulation results show good agreements with the experiment data over a wide range of ambient temperature and density. As ambient temperature rises the fuel droplets evaporate faster and liquid lengths becomes shorter. High ambient density causes shorter spray penetration. For JP8, simulation results show shorter liquid lengths especially with lower ambient densities. But in general current spray breakup, penetration and evaporation model can predict overall trend of liquid lengths over a wide ambient temperature and density changes as well as two different fuels.

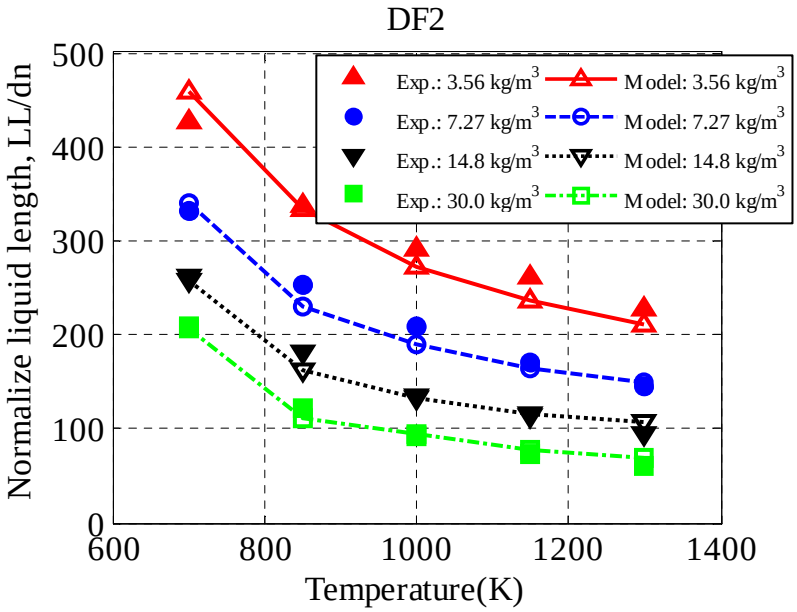

Figure 2.13 Liquid length comparison with various ambient condition. The injection pressure is 110 MPa with nozzle diameter of 0.246 mm for DF2. Initial fuel temperature is 436 K.

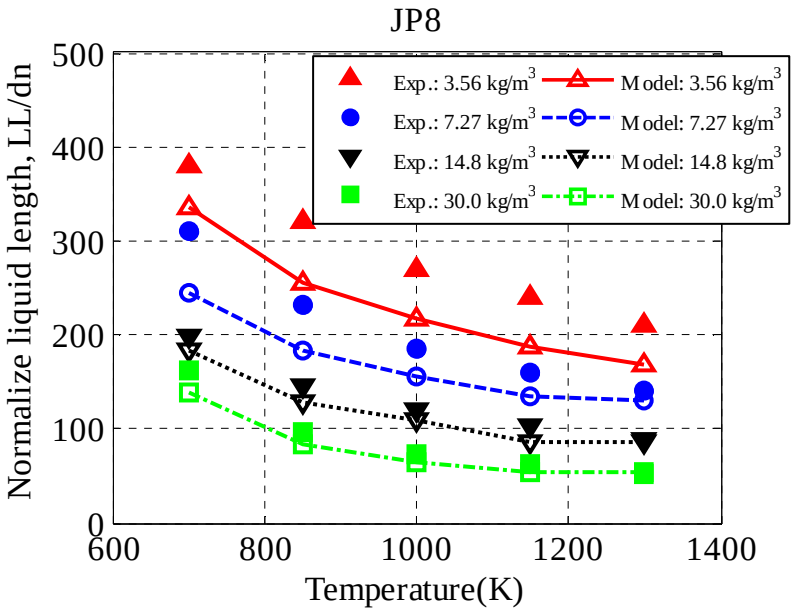

Figure 2.14 Liquid length comparison with various ambient condition. The injection pressure is 110 MPa with nozzle diameter of 0.180 mm for JP8. Initial fuel temperature is 436 K.

2.3.5 Effects of temperature and pressure on fuel spray and evaporation

The liquid phase life times of fuel sprays calculated with the presented model are analyzed. The liquid phase life time is calculated from the start of injection to the end of evaporation. In-cylinder ambient conditions at the time of injection, covering typical Diesel combustion as well as other combustion mode, are the region of interest: temperature range from 500 K to 1000 K and pressure range from 10 bar to 70 bar. The injection pressure of 600 bar, nozzle diameter of 0.18 mm and fuel temperature of 314 K were used. For the analysis, surrogates fuels for gasoline, DF2, JP8 and a single component fuel of DME are simulated. The gasoline surrogates are obtained from [72]. Other surrogates for DF2 and JP8 are described in the previous section. These surrogates with two-three components are selected to match the properties related to the evaporation only. It is impractical to match all the properties of real fuel since the number of component in the surrogates should be increased significantly. The blend ratio of surrogates and properties at the injection are listed in Table 2.3.

Figure 2.15 to Figure 2.18 show the results of liquid phase life time for various fuels. DME shows consistent evaporation trend in the entire sweeping range. Both ambient temperature and pressure causes shorter liquid life time as they rises. For gasoline, DF2 and JP8, the liquid life time are shorten as pressure rises at high temperature. However in the low temperature region below approximately 550 K, 680 K and 650 K for gasoline, DF2 and JP8 respectively, higher ambient pressure promotes longer liquid phase life time.

Table 2.3 Surrogate blends and properties at 314 K, 0.1 MPa

	Gasoline surrogate	DF2 surrogate	JP8 surrogate	DME
Blend ratio (mass basis)	n-hexane 34 %	n-tetradecane 49 %	n-dodecane 82%	dimethyl ether 100%
	n-decane 21 %	n-decane 31 %	n-tetradecane 18%	n/a
	n-heptane 45%	1-methyl naphthalene 20 %	n/a	n/a
Density (kg/m^3)	665.17	783.54	733.3	621.37
Viscosity (mm^2/s)	0.588	1.634	1.567	0.164
Surface tension (kg/s^2)	0.0193	0.0266	0.0246	0.0103
Diffusion coefficient (m^2/s)	7.76e-6	5.98e-6	5.78e-6	1.36e-5
Molar mass (kg/kmol)	100.96	164.98	174.61	46.069

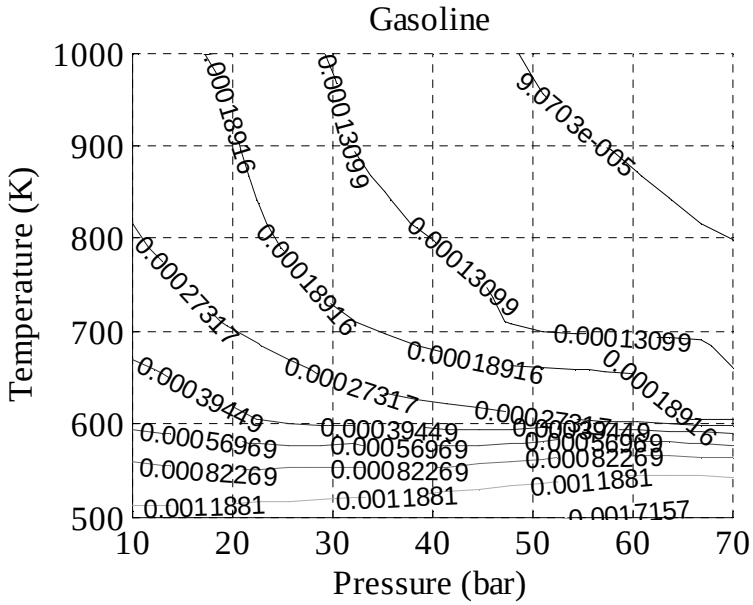

Figure 2.15 Liquid phase life time for Gasoline spray

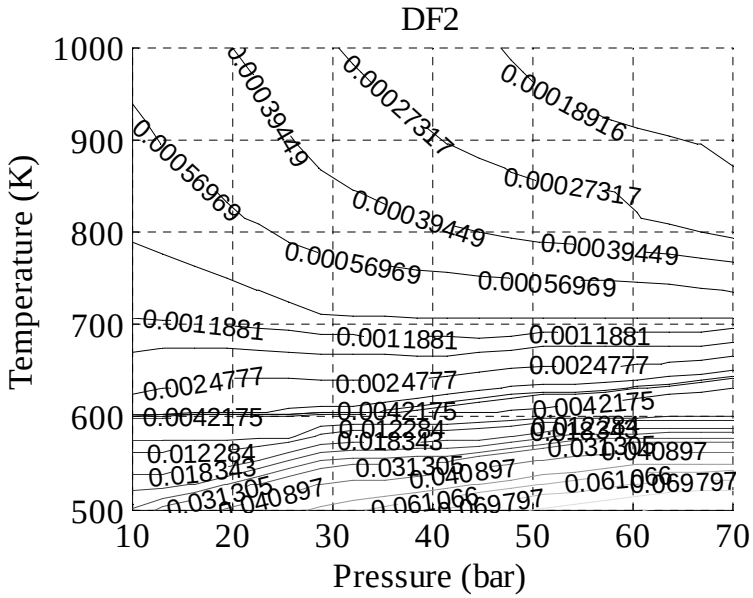

Figure 2.16 Liquid phase life time for DF2 spray

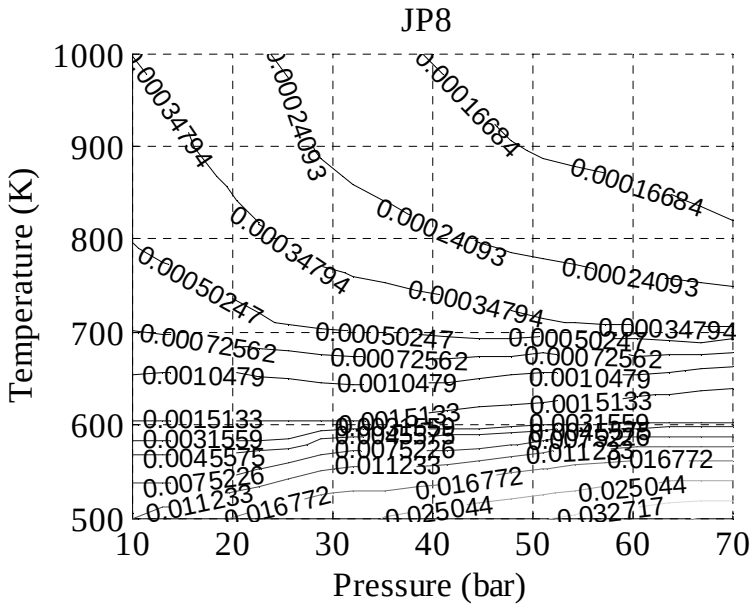

Figure 2.17 Liquid phase life time for JP8 spray

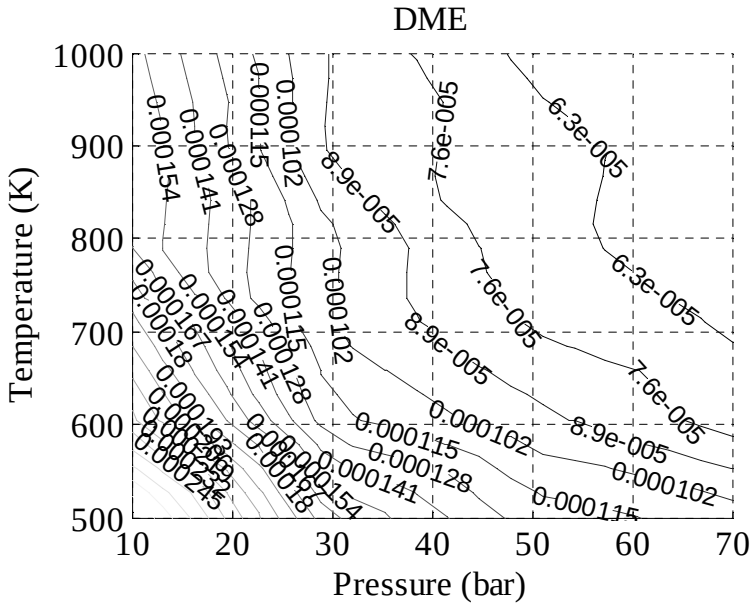

Figure 2.18 Liquid phase life time for DME spray

Such dependence of liquid droplets life time behavior on the ambient pressure can be also found in the previous experiments [67, 73]. The life time of liquid phase fuel decreases with pressure increasing at high temperature, but at low temperature its trend is reversed. Evaporation time illustrated in Figure 2.19 clearly show such trend captured by the presented model. DME is extremely volatile compared to other fuels and the saturated vapor pressure at given temperature is higher than other fuels. Therefore suppressing effects of high ambient pressure on the evaporation is relatively weak with DME. Thus the tendency did not appear in Figure 2.18 but in Figure 2.19 with much lower temperature range. The reversal trend of DME can be observed at around 300 K.

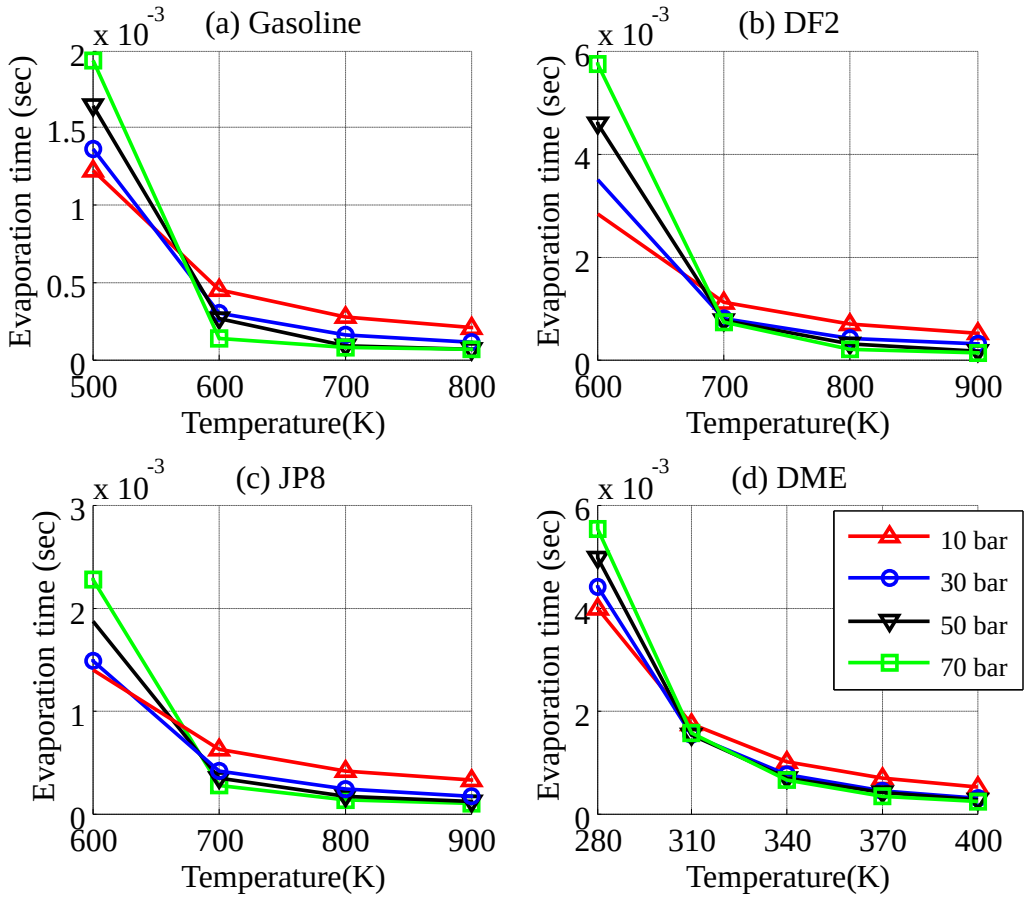

Figure 2.19 Behavior of evaporation model with temperature and pressure

2.3.6 Species history

Evaporation of multi-component fuel spray in four different cases (25 bar and 55 bar at 600 K and same ambient pressures at 900 K) are simulated. The injection conditions were the same as the previous section 4.5.Figure 2.20 to Figure 2.23 show liquid mass fraction histories of species in the droplet with three different fuels. It is obvious that species with higher volatility evaporate first. At lower ambient temperature conditions in Figure 2.20 and Figure 2.22, lighter species evaporates from the early stage of evaporation while heavier species tend not to evaporate. Thus their composition

increases fast with time. At higher ambient temperature condition in Figure 2.21 and Figure 2.23, heavier species evaporate equally with light species and lighter species accelerates its evaporation in the later stage. Therefore the composition of liquid droplets does not change much at earlier stage.

In terms of overall evaporation time, increasing the ambient temperature at a given pressure shortens the evaporation time. At higher pressure, evaporation time is also decreased except for DF2 and JP8 fuel at 600 K. It is because the dependence on the pressure changes below 650 to 680 K for these fuels as observed in Figure 2.19.The effect of the temperature on evaporation is more significant than the pressure. Ambient temperature increment of 300 K reduces evaporation time dramatically in both pressure cases.

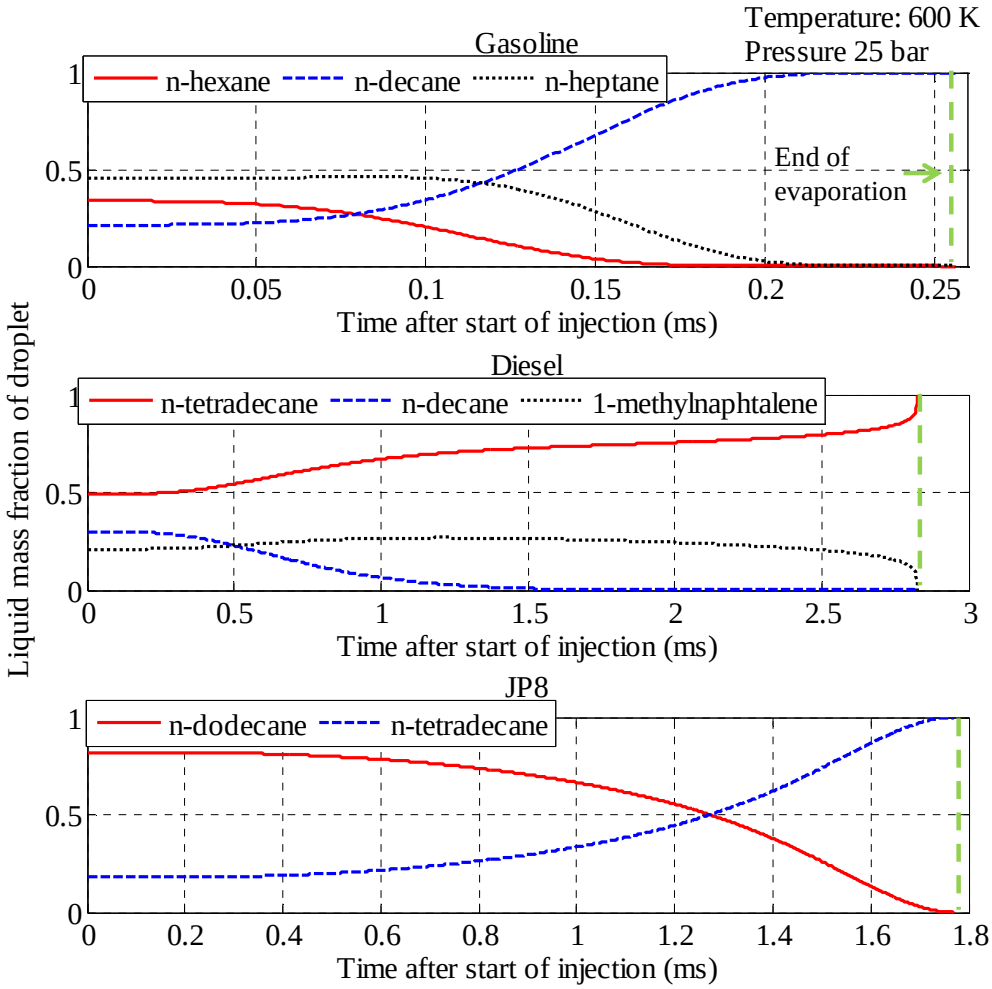

Figure 2.20 Liquid mass fraction histories of the components at 25 bar and 600 K

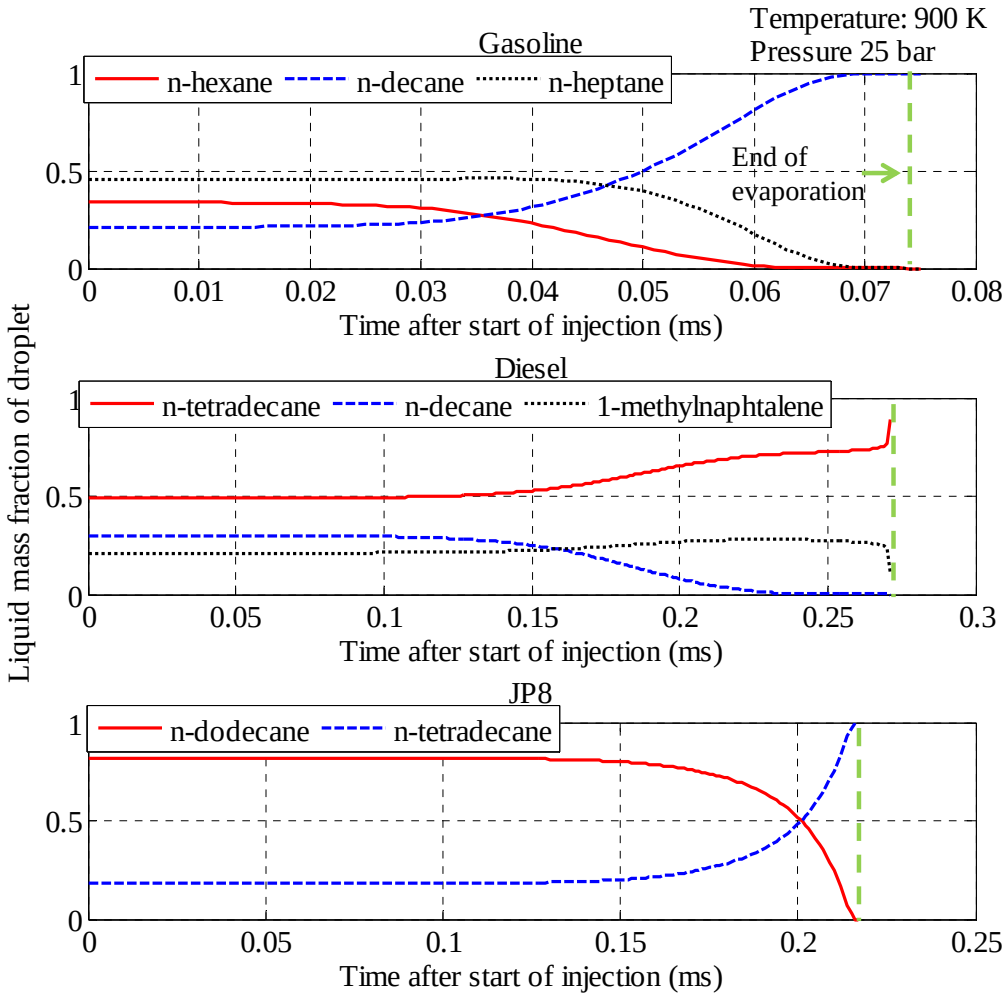

Figure 2.21 Liquid mass fraction histories of the components at 25 bar and 900 K

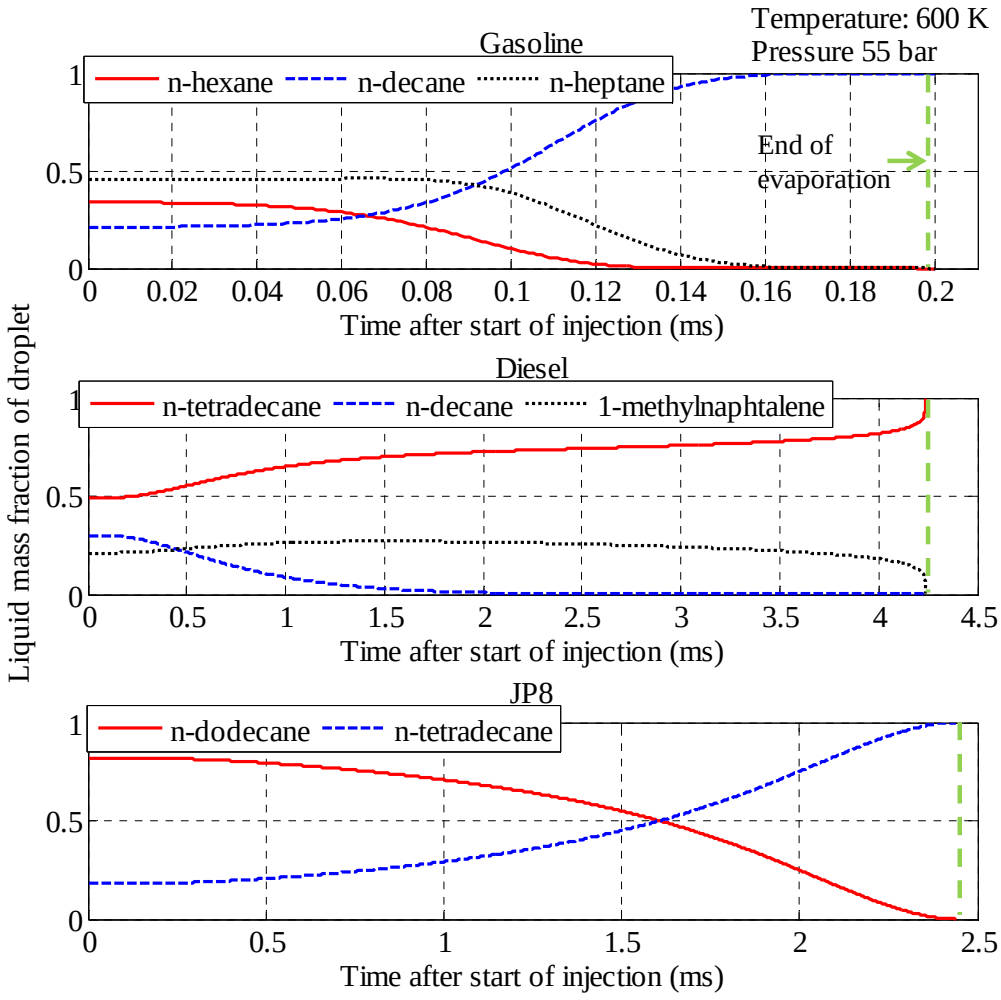

Figure 2.22 Liquid mass fraction histories of the components at 55 bar and 600 K

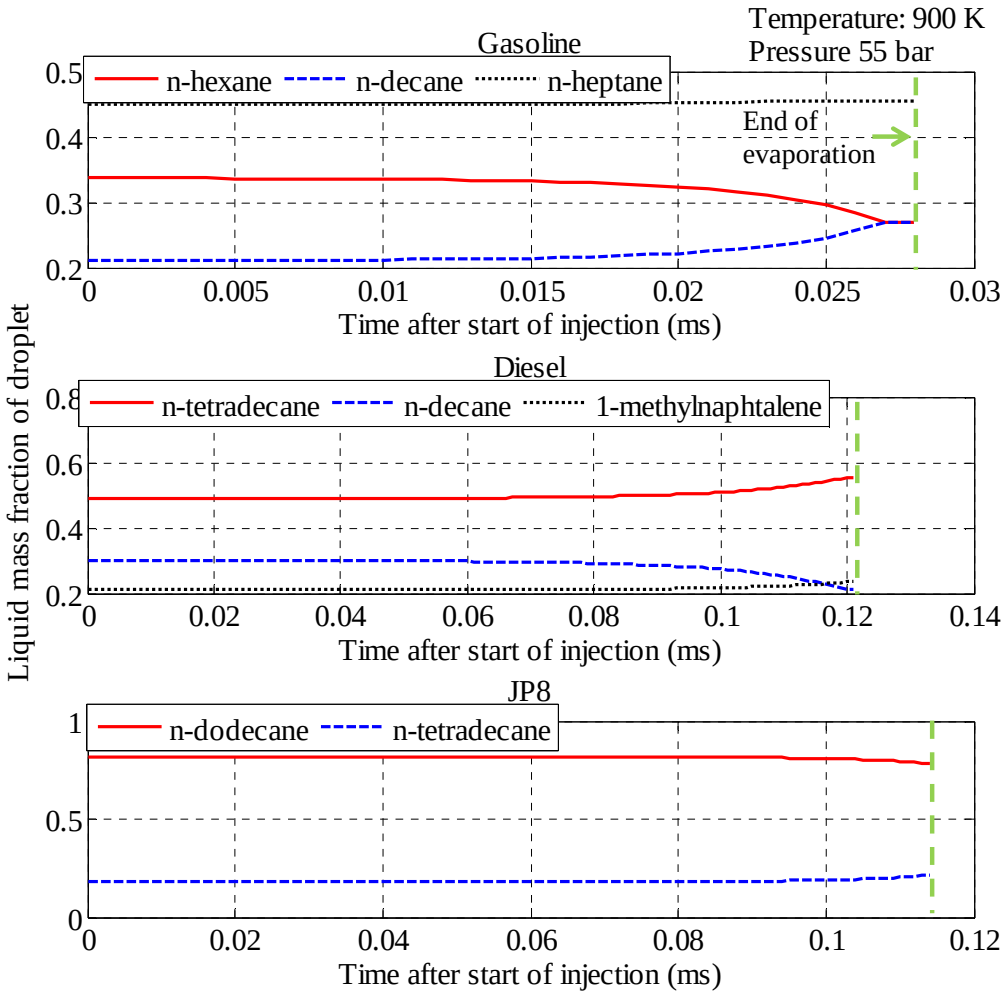

Figure 2.23 Liquid mass fraction histories of the components at 55 bar and 900 K

2.4 Summary and Conclusions

This chapter presents the enhanced models for spray and evaporation for the quasi-dimensional multi-zone DICI engine simulation framework. These models are capable of capturing various thermo-physical properties of multi-component fuel which is a key element in the adaptation of alternative fuels to DICI engine operation.

The modification of the classical phenomenological spray correlation using the WAVE breakup model and implementing zone to zone interaction for the pre-breakup region showed improvement of model fidelity and captures behaviors of spray penetration of various fuels. In addition, spray angle comparison result validates the current approach for calculating air entrainment rate. A simple multi-component droplet evaporation model has been extended from single component droplet evaporation. This method proves the capability of predicting multi-component fuel droplet vaporization rate in various ambient conditions. In addition, the developed model simulates evaporation of penetrating DF2 and JP8 fuel sprays over a wide range of temperature and pressure conditions.

The major conclusions are as follows.

1. Surface tension and viscosity of a liquid fuel are key properties that need to be included in a breakup model in addition to density and injection pressure differences. This includes additional fuel specific properties in the model.

2. By adding a zone to zone interaction model, the inconsistent locations of the initial zones relative to the main spray is avoided. This improves the behavior and consistency of the previous developed model of the spray.

3. The proposed model allows a different composition in the vapor compared to the liquid as influenced by different ambient conditions and the fuel mixture composition. The effect of an elevated pressure is important and included in the vaporization process model. This can have a significant impact on the ignition delay and subsequent combustion, and generally improves the fidelity of the model.

4. From the evaluation of the model with various fuels in a wide range of engine in-cylinder conditions, the model is able to capture a complex influence of the temperature that depends on pressure and the fuel type. This will become more pronounced with certain conditions, such as early injection or EGR, both leading to lower temperatures.

Chapter 3

Fuel sensitive ignition delay models for a local and global description of direct injection internal combustion engines

In this chapter, the Arrhenius type fuel sensitive spray ignition delay models in the quasi-dimensional multi-zone DICI engine simulation are presented. Ignition delay models are developed using two different descriptions. The developed models are able to capture ignition delay of typical fuels suitable for Diesel engine operation including dilution effect. Other kinds of fuels are also used to evaluate the new models.

3.1 Ignition delay overview

Even though an Arrhenius equation type ignition delay model can be used for both spray ignition delay and the premixed charge ignition delay, the calibration of the model for each case is very different because the premixed charge ignition process happens in a physically well prepared environment than the spray ignition process. In the premixed charge spatial variations are small so local diffusion/conduction processes are minimal whereas in the spray there are strong local gradients in most of the properties and thus significant local diffusion type fluxes, like heat, species flux and shear.

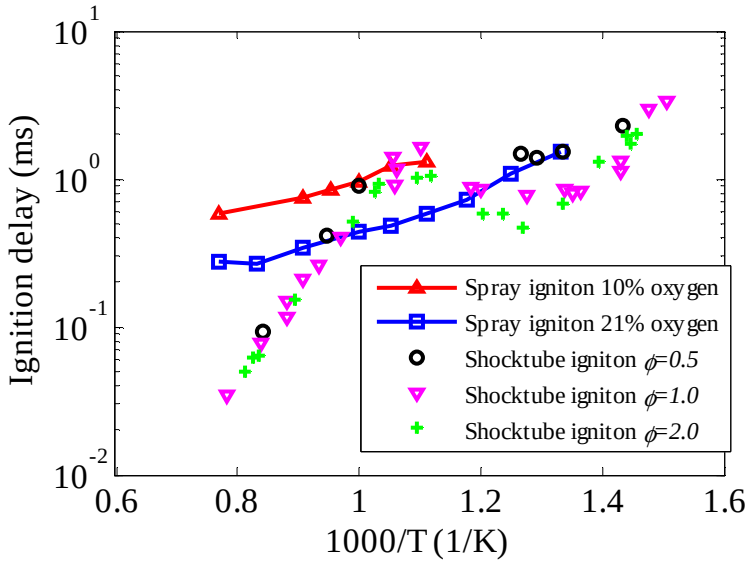

Figure 3.1 Comparison of n-heptane ignition of spray in constant volume chamber vs. shock tube ignition. Spray ignition delay is obtained from ECN data base [74] and shock tube data is obtained from Ciezki and Adomeit [75]. Presented data is scaled to 50 atm using the following equation: $\tau_{scaled} = \tau_{id}\left(50\text{atm}/P_{atm}\right)^{-1}$

A comparison of spray ignition delay and premixed ignition delay as a function of temperature is shown in Figure 3.1. As seen in the figure, the ignition delay behavior in the NTC regime is usually not observable with a fuel spray where temperature and pressure are under typical Diesel like conditions, except for the cases of extremely early injection. In addition, the apparent activation temperature (which is the activation energy divided by the universal gas constant) for the ignition delay is much smaller than for the premixed charge ignition delay except in the NTC regime. In a premixed charge, the ignition delay is mainly dominated by the chemical processes with vapor fuel and oxidizer well mixed. Local variance of their concentrations can be considered minimal as well. On the other hand, the spray ignition is a combination of chemical processes and physical processes with a stochastic distribution of properties like temperature and equivalence ratio. The ignition in a spray occurs at a local spot where environmental

conditions such as concentrations of fuel and oxidizer differ from location to location. The local temperature is lower than the ambient air temperature due to the evaporation of the liquid fuel. The local variance and transient behavior of the conditions are due to the physical processes of the spray evolution. As the liquid fuel penetrates into the ambient air in the combustion chamber, it breaks up, evaporates, and mixes with the entrained air. Therefore the concentrations of fuel and oxidizer continuously change while the spray evolution process is happening.

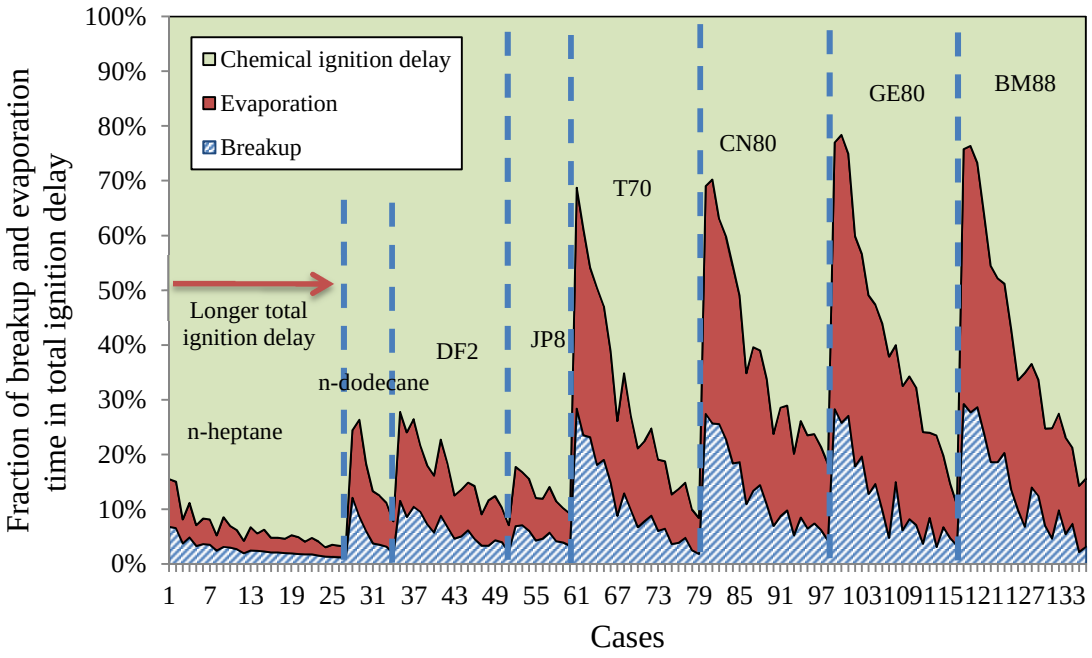

Figure 3.2 Physical and chemical ignition delays

Figure 3.2 shows how the total ignition delay is split into the breakup time, the evaporation time and the balance is the chemical time. The spray ignition delay data are taken from a constant volume chamber by Sandia National Laboratories and they are available in the online data base called the Engine Combustion Network (ECN) [74]. The blend ratio and properties of the test fuels are listed in Table 3.1. The breakup and

evaporation times are calculated from the sub-models developed in Chapter 2 for given fuels. It should be notice that the total ignition delays are normalized to 100% and the breakup and evaporation times are not changing dramatically as appears in the figure. But overall they occupy significant portion of total delay for some fuels, thus it should be considered in the spray ignition delay.

The breakup time model is a function of density, viscosity and surface tension. Higher density, viscosity and lower surface tension result in longer breakup time. As seen in the result of Chapter 2 the viscosity and surface tension need to be extremely different from one another to have a significant effect to breakup. Differences of surface tension between fuels are not big enough to change breakup time considerably. T70 has second lowest viscosity among the fuels, but because of high density, breakup time is longer than fuels like n-heptane, n-dodecane, DF2 and JP8.

Saturated vapor pressure, diffusion coefficient heat of evaporation and specific heat capacity are closely related to the evaporation process. Faster evaporation time is a result of both higher diffusion coefficient and higher saturated vapor pressure. In addition, both higher heat of evaporation and lower liquid heat capacity prevent temperature rising of fuel droplets. Therefore evaporation time turns out to be shorter. Evaporation time of n-heptane is shortest because the fuel has highest saturated vapor pressure. T70, CN80, GE80 and BM88 have relatively low saturated vapor pressure, which leads to longer evaporation time. BM88 has lowest saturated vapor pressure however also has relatively low liquid heat capacity. Therefore droplet temperature rises little faster than others. In case of evaporation process, the related fuel properties of evaporation interacts more

compared to breakup process so the result of evaporation should not be judged by a single property of fuel.

For the chemical ignition delay part, the process is strongly influenced by its chemistry. In addition the process is also very sensitive to the detailed conditions in the local gas mixture and its history. The variations of local conditions are calculated by breakup, evaporation and air entrainment processes. Thus these physical fuel spray evolution process is an important part for the modeling of the ignition delay in a DICI engine.

Table 3.1 Fuel blend ratio and property of ECN test fuels

		JP8*	DF2	n-heptane	n-dodecane	T70	CN80	GE80	BM88
Fuel blend ratio (mass basis, surrogates are used for DF2 and JP8)		n-dodecane 82%	n-tetradecane 49 %	n/a	n/a	Tetraethoxy-propane 73.9 %	n-hexadecane 76.5 %	Tri-propylene-glycol-methyl-ether 83.0 %	Dibutyl-maleate 89.1 %
		n-tetradecane 18%	n-decane 31 %			Heptamethyl-nonane 26.1 %	Heptamethyl-nonane 23.5%	Heptamethyl-nonane 17.0 %	n-hexadecane 5.6 %
		n/a	1-methyl naphthalene 20 %			n/a	n/a	n/a	2-ethylhexyl-nitrate 5.3 %
Properties at 373K***	Density (kg/m3)	731	767	613**	693**	808	724	858	907
	Viscosity (mm^2/s)**	0.838	0.799	0.357	0.747	0.488	1.250	1.471	1.181
	Surface tension (kg/s^2)**	0.0223	0.0198	0.0117	0.0194	0.0225	0.0216	0.0287	0.0252
	Diffusion coefficient (m^2/s))**	1.01E-06	4.68E-07	1.47E-06	1.04E-06	1.10E-06	8.96E-07	1.01E-06	9.49E-07
	Saturated vapor pressure (kPa))**	3.7297	1.6987	105.59	1.9351	0.36791	0.25982	0.12755	0.062636
	hevap (kJ/kg))**	321.35	306.56	310.03	307.98	279.73	283.09	395.83	327.93
	Cpl (kJ/kg/K))**	2.367	2.497	2.602	2.501	2.225	2.446	2.406	2.164
(*nO2 /nf*) at stoichiometry		19.11	18.59	11	18.5	18.92	24.5	16.91	17.09

* JP8 test data is tabulated from literature [66]. The test data was also acquired used the same test setup in Sandia National Laboratories, but not listed in the ECN.

** These properties are calculated based on fuel surrogates. For calculation methods, see Appendix A.

*** Some of ECN ignition data are not measured with liquid fuel temperature at 373K. The listed properties are for comparison purpose. See Appendix C for detailed experiment conditions.

3.2 Fuel sensitive spray ignition models

To develop a fuel sensitive spray ignition delay model, experimental data of spray ignition delay using different fuels in a same test setup are collected from the ECN database. From this database, spray ignition delay data of four different fuels (JP8, DF2, n-heptane and n-dodecane) are taken and used for regression.

The obtained data is pre-screened to match the experimental conditions close to that of Diesel engines. For example, ignition delay less than 2 ms, and injection pressure difference of 1400 ~ 1500 bar data are used for the regression analysis. The test data used for the analysis are listed in Appendix C. It is impossible to conduct an experiment which controls fuel properties or chemical reactions of the auto ignition process in the fuel spray. Therefore, in the experiment, control parameters are limited to the environmental parameters such as temperature, pressure, composition of oxidizer, and injection conditions. Table 3.1 shows properties and blend ratio for surrogates of the test fuels.

3.2.1 Formulation of fuel sensitive spray ignition delay model using global information

Typically an Arrhenius type spray ignition delay model is developed as a function of global temperature and pressure in the combustion chamber. An Arrhenius type model based on Wolfer's correlation[45] is one of the simplest models, which is traditionally used as a spray ignition delay model in a Diesel engine simulation.

$$\tau_{id}[ms] = A_g P^{-n} \exp\left(\frac{\theta_g}{T_g}\right) \tag{3.1}$$

where, A_g is a pre-exponential parameter in ms·bar^n, P is chamber pressure in bar, n is exponent for pressure sensitivity, T_g is global chamber temperature in K, and θ_g is a global apparent activation temperature in K.

This equation form served very well in the Diesel engine simulation for several decades, however, the correlation does not contain variables which can capture dilution effects. In the ECN spray ignition delay data set, simulated EGR data is included. To simulate dilution by EGR, test data was selected for the condition of various ambient oxygen mole fractions which are experimentally controlled by pre-combustion. Therefore, Eq. (3.1) is modified to include the ambient oxygen mole fraction $y_{O_2,Amb.}$.

$$\tau_{id}[ms] = A_g P^{-n} y_{O_2,amb}^{-m} \exp\left(\frac{\theta_g}{T_g}\right) \tag{3.2}$$

where m is the exponent for the ambient O_2 mole fraction sensitivity. The charge overall air-fuel ratio or equivalence ratio is not included as they have very little influence on the local ignition delay in the spray configuration.

Table 3.2 Individual calibration parameters for four different fuel using ECN test data

	JP8	DF2	n-heptane	n-dodecane
A_q (ms · bar^n)	0.6204	0.1853	0.2697	0.0332
n			1.0	
m			1.0	
θ_g (K)	2587.9	3350.7	2799.8	3946.6
R^2	0.9676	0.9148	0.9612	0.9778

For each of the fuels in the ECN data, the model in Eq. (3.2) is calibrated and the calibration parameter sets are listed in Table 3.2. The pressure and oxygen mole fraction

exponents (n, m) are found to be the same for the four test fuels. The listed calibration parameters are implicitly includes the fuel properties which affect the ignition delay of spray. To develop fuel sensitive spray ignition delay model, these properties need to be identified and used as explicit variables for the correlation. With a fuel spray, the ignition delay is affected not only by a chemical ignition process but also by physical fuel spray evolution processes such as penetration, evaporation, air entrainment and mixing. The effect of all these processes on the spray ignition delay is still unclear and to separate and observe the effects of these processes in the experiment is almost impossible as well.

The Cetane number is a traditional parameter that characterizes ignition quality of the fuel. The standard procedure [76, 77] for measuring the Cetane number utilizes spray ignition apparatus such as cooperative fuel research (CFR) engine or ignition quality tester. Since the procedure measures the apparent effect of a fuel on the spray ignition from the tester, the Cetane number is the parameter which takes into account both physical and chemical ignition processes. Since Cetane number is measured with a specific operating conditions and test equipment, the ignition delay in a real engine can be different between fuels with the same Cetane number. The ignition delay varies depending on different ambient conditions and this is altered by different equipment and operating conditions. The deviation between fuels and effect of environmental condition of different engine condition can be captured by the Arrhenius equation.

Some of the ignition delay models [42, 48] utilize Cetane number for modeling the activation energy. However, apparent global activation temperatures do not vary as much as parameter A_g. With the temperature range of typical engine simulation situation, the activation temperature differences are even less pronounced. Figure 3.3 shows that

using average apparent activation temperature, 3171 K, actually fits reasonably well with different fuels although n-dodecane result shows slightly larger error than others. In fact, small variations of apparent activation temperature indicate local temperature sensitivities of ignition delays for different fuels are masked by the spray processes. Compared to the activation temperature variation of different fuels in premixed ignition delay experiment [78, 79], the deviation in spray ignition delay is very small. When averaged apparent activation temperature is used, the trend of model parameter A_g against Cetane number becomes monotonic and can be expressed by a function of the Cetane number as seen in Figure 3.4.

The curve fitting of the pre-exponential parameter A_g becomes a simple power function of the Cetane number *CN*.

$$A_g = 402.87 CN^{-1.936} \tag{3.3}$$

By substituting Eq. (3.3) into Eq. (3.2), the fuel sensitive spray ignition delay using global information (global information model) becomes as follows.

$$\tau_{id}[ms] = 402.87 CN^{-1.936} P^{-1} y_{O_2,amb}^{-1} \exp\left(\frac{3171}{T_g}\right) \tag{3.4}$$

This global model uses the Cetane number as the sole fuel specific information build into this model. Together with the overall charge pressures, temperature and ambient oxygen concentration these variables are predicting the ignition delay.

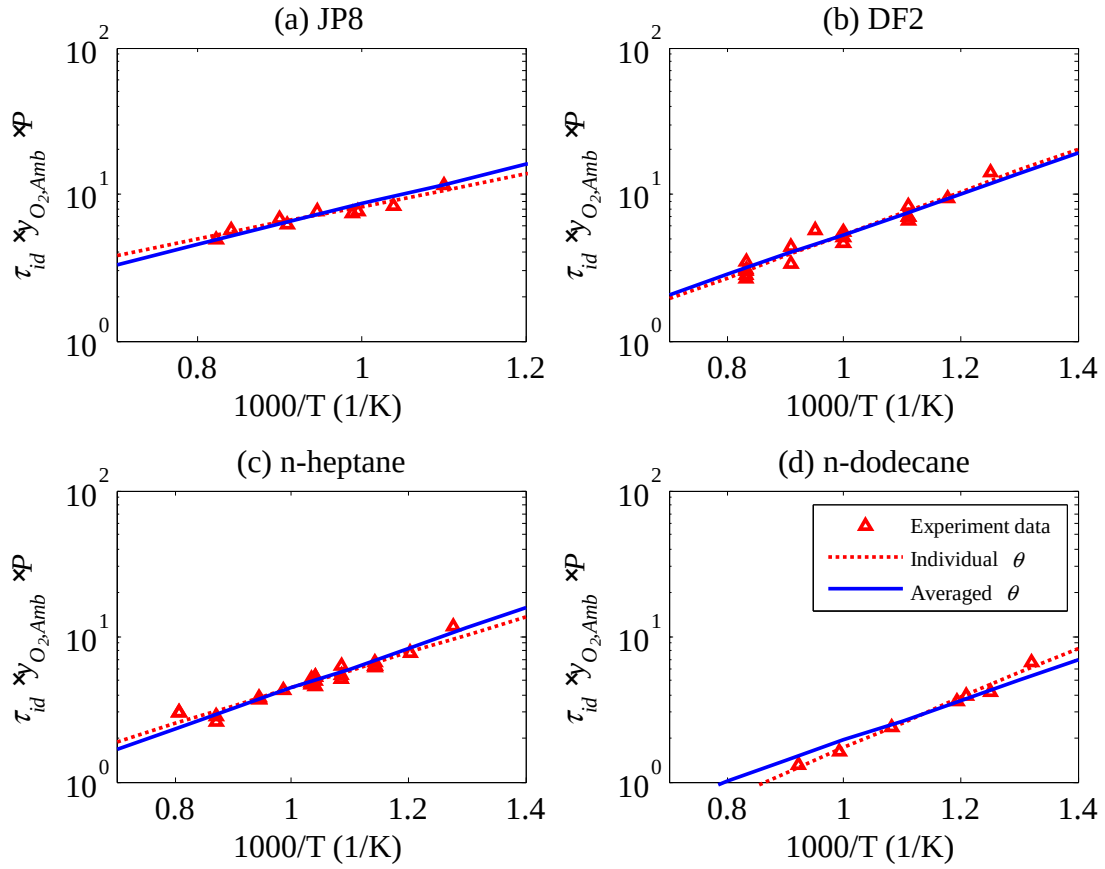

Figure 3.3 Comparison of activation temperatures. From Eq. (3.2) with exponent -1 for both pressure and ambient oxygen mole fraction, experimental and calculated ignition delay can be expressed as a simple exponential form, $A\exp(\theta/T)$.

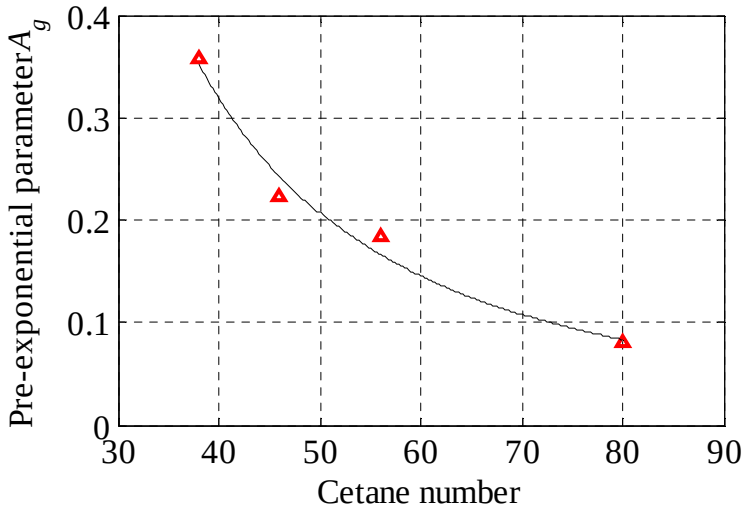

Figure 3.4 Monotonic behavior of pre-exponential parameter A_g and its curve fitting model. R^2=0.9829

3.2.2 Formulation of fuel sensitive spray ignition delay model using local spray information

The actual ignition occurs in a local spot of injected fuel spray. Therefore, the global ignition delay model cannot capture the deviation of local conditions such as temperature, and equivalence ratio from the average chamber condition. To enhance the spray ignition delay model, such local condition information should be utilized. This information is available with the enhanced spray and evaporation model described in the previous chapter. In each zone, the concentration (molar density) of oxygen and fuel vapor is calculated as follows.

$$[O_2] = \frac{y_{O_2} P}{\bar{R} T_z} \quad \text{and} \quad [F] = \frac{y_F P}{\bar{R} T_z} \tag{3.5}$$

where $[O_2]$ and $[F]$ are concentrations in mol/cm^3, y_{O_2} and y_F are mole fractions, P is global pressure in bar, $\bar{R}$ is universal gas constant: 83.1446 cm^3·bar/(mol·K) and T_z is zone temperature in K.

Since a part of the physical process of spray ignition delay such as break up and evaporation is captured by the multi-zone spray model, the ignition delay model is required to capture the ignition delay dominated by chemical effects. The Arrhenius equation used for the premixed charge ignition delay experiment [78, 80, 79] data fitting is considered as a chemical ignition delay correlation. Thus for the ignition delay model with a multi-zone spray model, the following correlation is used.

$$\tau_{del}[ms] = A[O_2]^{-n}[F]^{-m} \exp\left(\frac{\theta}{T_z}\right) \tag{3.6}$$

where, τ_{del} is delay time in ms from breakup to ignition, A is pre-exponential parameter in ms·(mol/cm^3)$^{n+m}$, n and m are exponent that determines effect of concentration, and θ is apparent activation temperature in K.

Although the multi-zone model captures physical part of ignition delay by calculating concentration of each zone, there are additional information which should be implicitly captured by the experimentally determined pre-exponential parameter A and apparent activation temperature θ. In addition, breakup time is not included in the ignition delay since there is no fuel vapor in the zone during this period. The evaporation process starts after breakup and generates fuel vapors. Thus Eq. (3.6) is defined to calculate the delay time, τ_{del} from breakup to ignition, which includes evaporation time and chemical ignition time.

By reformulating Eq. (3.6), the uncertainties of the physical part of the ignition delay can be identified. Replacing the concentration terms in Eq. (3.6) with Eq. (3.5), the delay time, τ_{del} can be expressed as follow.

$$\tau_{del}[ms] = A\frac{P^{-n-m}}{\left(\overline{RT}\right)^{-n-m}} y_{O_2}^{-n} y_F^{-m} \exp\left(\frac{\theta}{T_z}\right) \tag{3.7}$$

The mole fraction of fuel can be also expressed with equivalence ratio and molar oxygen-fuel ratio.

$$y_F = \frac{y_{O_2}\phi}{\alpha} \tag{3.8}$$

where α is the stoichiometric molar ratio of oxygen to fuel. The ratio is equal to $a+0.25b$ with a hydrocarbon fuel, C_aH_b.

In Eq. (3.8) , the definition of equivalence ratio is expressed with mole fractions.

$$\phi = \frac{\left(n_{O_2}/n_F\right)_{ST}}{\left(n_{O_2}/n_F\right)_R} = \frac{\left(y_{O_2}/y_F\right)_{ST}}{\left(y_{O_2}/y_F\right)_R} = \frac{\alpha}{\left(y_{O_2}/y_F\right)_R} \tag{3.9}$$

where subscript *ST* and *R* indicates stoichiometric condition and real condition respectively.

After the mole fractions of fuel in Eq. (3.7) is replaced with Eq. (3.8), the equation becomes,

$$\tau_{del}[ms] = \left\{\frac{A}{\overline{R}^{-n-m}\alpha^{-m}}\right\}\phi^{-m}P^{-n-m}y_{O_2}^{-n-m}\left\{\exp\left(\frac{\theta}{T_z}\right)\frac{1}{T_z{}^{-n-m}}\right\} \tag{3.10}$$

The first curly bracket of Eq. (3.10) is a constant but contains some fuel information. Thus the whole bracket can be expressed as another pre-exponential parameter A_z. Then the pre-exponential parameter A can be written as follows.

$$\left\{\frac{A}{\overline{R}^{-n-m}\alpha^{-m}}\right\} = A_z \tag{3.11}$$

$$A = A_z\overline{R}^{-n-m}\alpha^{-m} \tag{3.12}$$

Finally, by substituting pre-exponent parameter A in Eq. (3.6) by Eq. (3.12), and use θ_z instead of θ to signify the new model, the equation becomes,

$$\tau_{del}[ms] = A_z\overline{R}^{-n-m}\alpha^{-m}\left[O_2\right]^{-n}\left[F\right]^{-m}\exp\left(\frac{\theta_z}{T_z}\right) \tag{3.13}$$

where θ_z is local apparent activation temperature for the multi-zone spray model in K. Note that all the calibration parameters (n, m, A_z and θ_z) are model constants applied for all the different zones. The local information used in the model is the temperature and the two concentrations.

In theory, the equivalence ratio of the spray changes significantly during the evaporation and air entrainment processes, therefore the equivalence ratio can range from zero to infinity. If the equivalence ratio reaches extreme values (small or large), ignition delay must become longer since there are not enough oxidizer or fuel molecules to interact with each other. The minimum ignition delay does not necessary have to be located at equivalence ratio of 1. In Eq. (3.13), the concentration exponents represent sensitivity to the concentration, hence to the equivalence ratio. As seen in the Figure 3.5, positive exponents for both *n* and *m* are desired for the desired response with respect to the change in equivalence ratio.

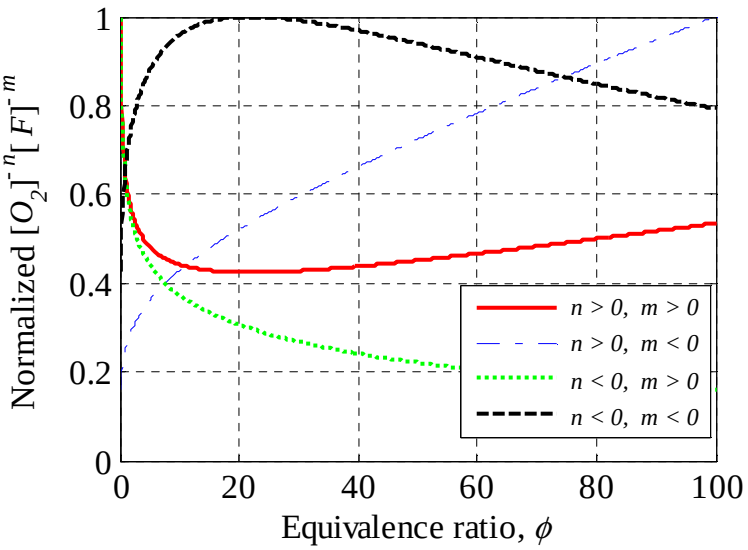

Figure 3.5 Effect of different values of concentration exponents

In Eq. (3.10), the pressure exponent is (-*n*-*m*). This exponent should be the same value as the exponent value from global spray ignition delay model in Eq. (3.4) because

of the global pressure assumption. Thus a criterion ($n+m=1$) can be used in addition to the positive exponents for current test fuels in this study.

Table 3.3 Parameters for local ignition delay model

	JP8	DF2	n-heptane	n-dodecane
A_z	1.76E-4	1.13E-4	9.99E-5	4.56E-5
n	0.8			
m	0.2			
θ_z (K)	4000			

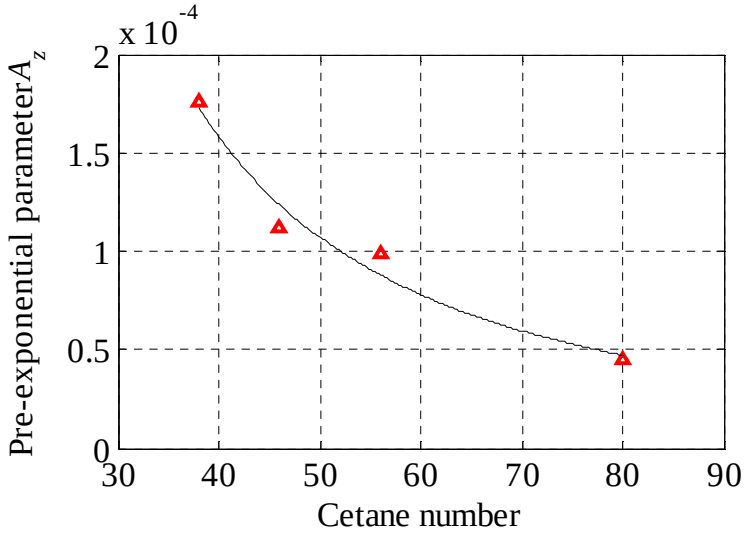

Figure 3.6 Regression of pre-exponent parameter A_z versus Cetane number for local ignition delay model.

After implementation of Eq. (3.13) in the multi-zone model, calibration parameters are obtained using ECN data and listed in Table 3.3. For simplicity, a fixed apparent activation temperature and only one set of the concentration exponents are used. The obtained pre-exponential parameter A_z are presented in Figure 3.6 with respect to Cetane number of the fuels. It shows that the pre-exponential parameter A_z can be described as a power function of Cetane number similar to global ignition delay model.

In addition exponent for universal gas constant in Eq. (3.13) is also (*-n-m*) for all the test fuels. Therefore,

$$A_z = 9.84\times10^{-2} CN^{-1.744} \tag{3.14}$$

$$A_z \overline{R}^{-1} = 1.183\times10^{-3} CN^{-1.744} \tag{3.15}$$

Finally, the fuel sensitive spray ignition delay model using local spray information becomes.

$$\tau_{del}[ms] = 1.183\times10^{-3} CN^{-1.744} \alpha^{-0.2} [O_2]^{-0.8} [F]^{-0.2} \exp\left(\frac{4000}{T_z}\right) \tag{3.16}$$

Using the ignition integral by Livengood and Wu [81], the ignition time, t_{ign}, is obtained from the condition

$$\int_{t_{break}}^{t_{ign}} \frac{1}{\tau_{del}} = 1 \tag{3.17}$$

where t_{break} is the breakup time of the spray. Note that the starting time of integration is the breakup time.

3.3 Results and discussion

3.3.1 Result of developed spray ignition delay models

Predicted ignition delay by the two developed ignition delay models is compared to the corresponding experimental data and presented in Figure 3.7 and Figure 3.8. In the figures, the test points have various combustion chamber density and ambient oxygen contents except for n-dodecane case. Thus the ignition delay shows in the chart is scattered. In order to identify validity of the proposed models easily from the figures,

presented data are scaled to 50 bar and 21 % oxygen with exponent -1 using the following equation and illustrated in in Figure 3.9 and Figure 3.10.

$$\tau_{scaled} = \tau_{id}\left(\frac{50\text{bar}}{P}\right)^{-1}\left(\frac{0.21}{y_{O_2,Amb}}\right)^{-1} \tag{3.18}$$

As seen in the figures, both models predict the ignition delay very well for most of the data points. The local ignition delay model captures the trend of ignition delay slightly better for DF2 and n-heptane fuels. The variations of local conditions within spray are captured with the local model so the spread of ignition delay at the same temperatures can be captured properly.

Table 3.4 shows R^2 results of each fuel for the two models. The average R^2 values are about 0.92 for both models. When compared to global spray ignition delay model, using the local information of spray improves the precision except for n-heptane case. As seen in the Figure 3.10 (c), this is mainly because the predictions are slightly biased towards shorter delay. Since n-heptane is the lightest among the four test fuels, it has the fastest evaporation rate. The concentration of fuel for n-heptane changes faster than the other fuels as well. Therefore, the exponent values used for local ignition delay model is less close to the optimal value for n-heptane and results in a less accurate prediction. Average root mean square errors for the global and local models are 0.0971 and 0.0957 respectively.

Table 3.4 R^2 of two fuel sensitive spray ignition delay models

Fuel	Global model	Local model
JP8	0.9467	0.9594
DF2	0. 8884	0.9024
n-heptane	0.9223	0.8865
n-dodecane	0.9074	0.9269
Average	0.9162	0.9188

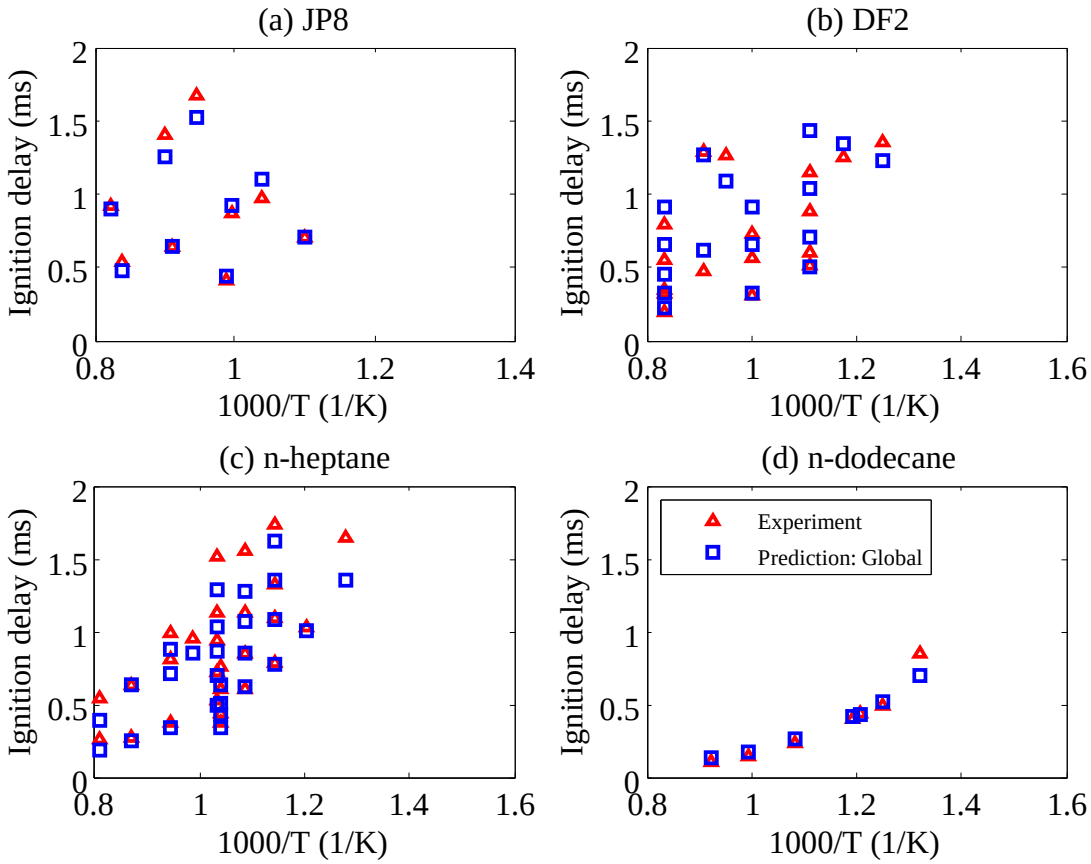

Figure 3.7 Prediction result of fuel sensitive spray ignition delay model using global information original data

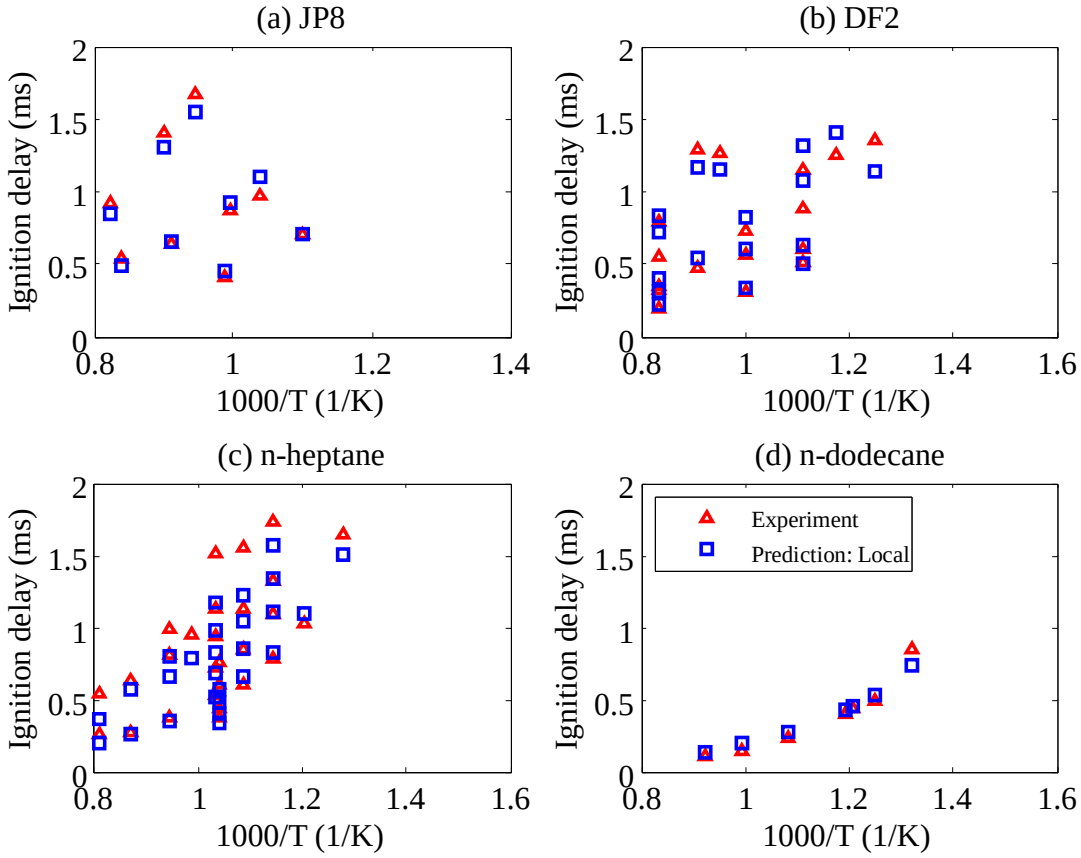

Figure 3.8 Prediction result of fuel sensitive spray ignition delay model using local spray information original data

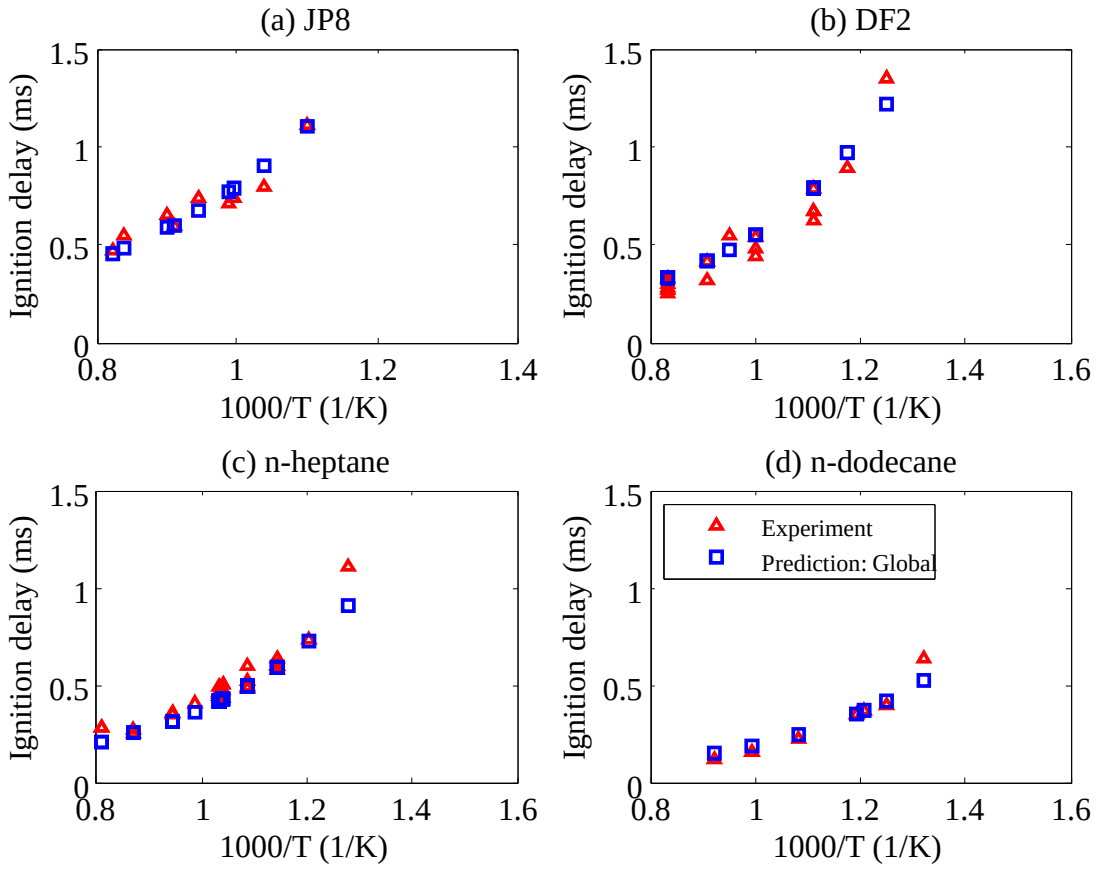

Figure 3.9 Prediction result of fuel sensitive spray ignition delay model using global information scaled to 50 bar and 21% oxygen.

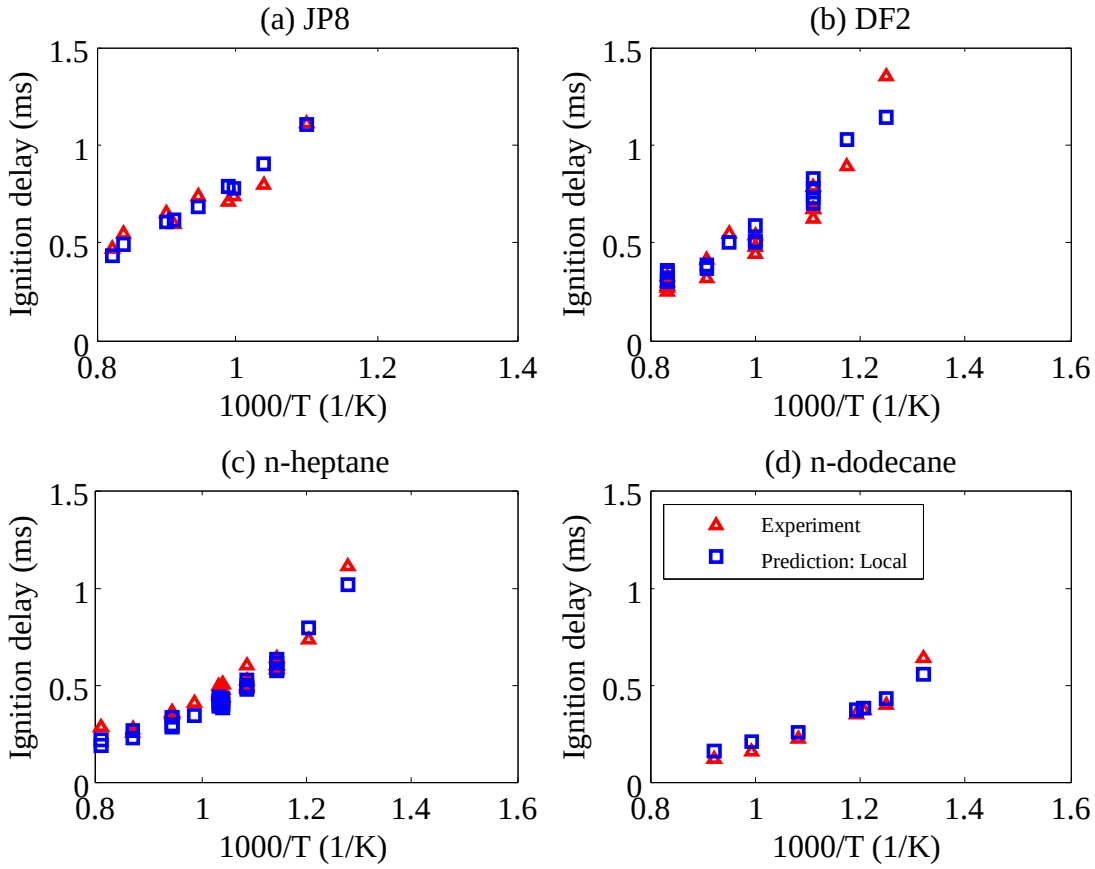

Figure 3.10 Prediction result of fuel sensitive spray ignition delay model using local spray information scaled to 50 bar and 21% oxygen.

3.3.2 Comparison with other spray ignition delay models

To highlight performance of the developed models, the predicted results from four other ignition delay models for a Diesel engine are shown in Figure 3.11 to Figure 3.14.

Wolfer's ignition delay model [45] is calibrated to 21 % ambient oxygen case of DF2 and presented in Eq. (3.19).

$$\tau_{id}[ms] = 0.95 P^{-1} \exp\left(\frac{3350.7}{T_g}\right) \tag{3.19}$$

Aligrot's model [47] in Eq.(3.20) is developed based on various blend of fuel with different Cetane number from 20 to 60. Parameter *A* from Wolfer's model is expressed in a linear function of Cetane number.

$$\tau_{id}[ms] = \exp\left(-3.55\times10^{-2}\,CN - 7.621\right)P^{-0.35}\exp\left(\frac{8610}{T_g}\right) \tag{3.20}$$

Rakopoulos's model [11] in Eq. (3.21) is used in their study of ethanol-Diesel fuel blends. Parameter *A* is calibrated to 4.5 ms·bar$^{0.737}$ for DF2 fuel in ECN data at 21 % ambient oxygen case.

$$\tau_{id}[ms] = AP^{-0.737}\exp\left(\frac{2100K\times 35.44/\left(CN+25\right)}{T_z}\right) \tag{3.21}$$

Zheng's model [42] in Eq.(3.22) is developed to capture oxygenated fuel effect of biodiesel fuel. The activation temperature from this model is modified from Watson's model [40] using Cetane number. Cetane number of 46.3 would have a factor of unity. Parameters *A, k* and *n* used for comparison are 6.1 ms·bar$^{1.02}$, 0.1 and 1.02 respectively.

$$\tau_{id}[ms] = A\left(\left[O_2\right]_{\text{intake}} + \left[F_O\right]_{\text{fuel}}\right)^{-k} P^{-n}\exp\left(\frac{2100\times 71.3/\left(CN+25\right)}{T_g}\right) \tag{3.22}$$

where $\left[O_2\right]_{\text{intake}}$ is oxygen concentration in intake flow, $\left[F_O\right]_{\text{fuel}}$ is equivalence oxygen concentration in fuel.

The result of calibrated Wolfer's model in Figure 3.11 shows that prediction result of each fuel aligned in parallel with each other except for n-heptane. This is because the calibrated activation temperature for DF2 used for this comparison is close to the calibrated temperature of the global spray ignition model in Eq. (3.4). Result of n-heptane is scattered because ambient oxygen contents of experiment data ranged from 8 %

to 21 % and the model does not captures the variation. The application of Aligrot's model in Figure 3.12 results in the most scattered results. The pre exponential parameter is a function of Cetane number and determined with their experimental results with corresponding activation temperature. Because its activation temperature is much higher than the calibrated temperature, the model does not perform well with ECN test fuels. Figure 3.13 shows Rakopoulos's ignition delay model results. This model is the only model that is developed for a multi-zone model among the four models in the comparison. However, the calculated activation temperature is quite low; for Cetane number from 38 to 80, the activation temperature change from 1181.44 K to 708.86 K. Also the model does not capture dilution effects. Thus even after calibration of parameter *A*, the results show a discrepancy with experimental data. Figure 3.14 shows Zheng's model result. This model also shows lower activation temperatures, 2376.7 K to 1432 K respectively for Cetane number from 38 to 80. This model captures oxygen concentration of intake air and oxygenated fuel, but due to the lower activation temperature the model does not exhibit a good result.

The result of all four ignition delay models shows that they are inadequate for predicting the ignition delay of different fuels or diluted conditions other than the fuel range that each model was originally developed for.

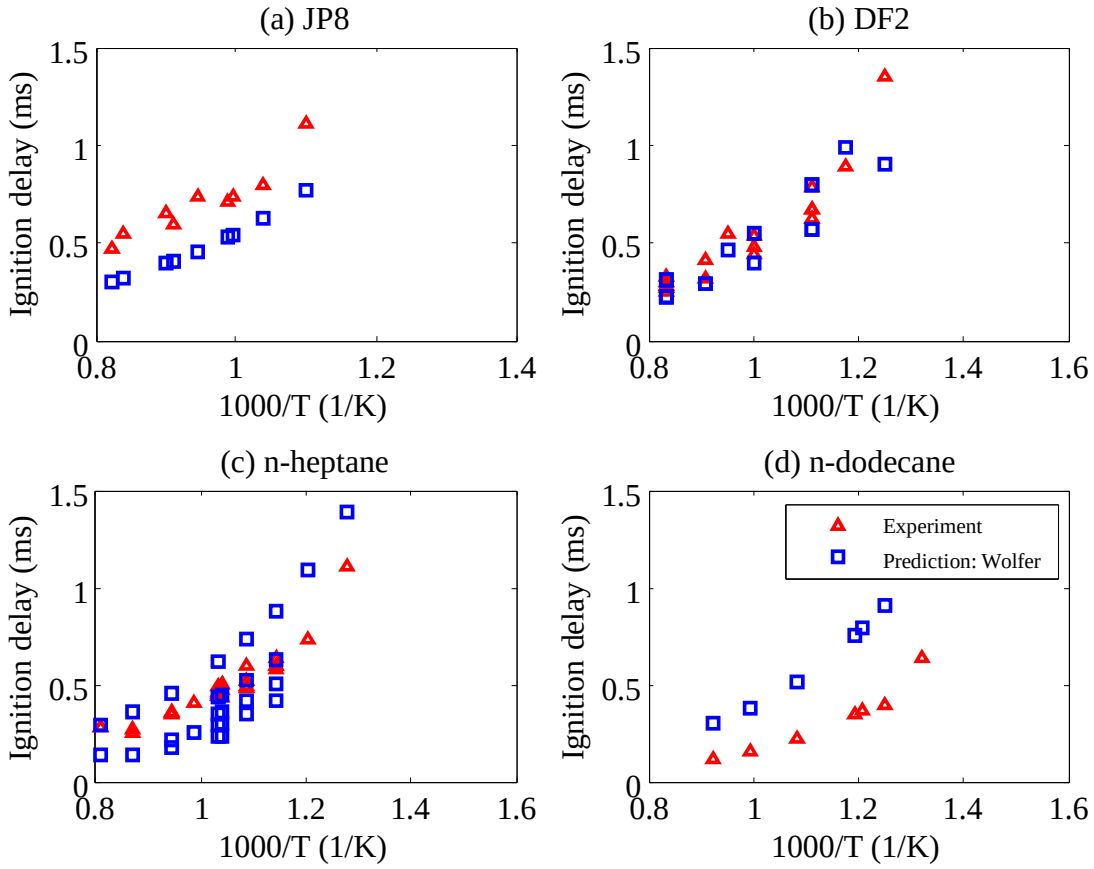

Figure 3.11 Prediction result of calibrated Wolfer's ignition delay model scaled to 50 bar and 21% oxygen.

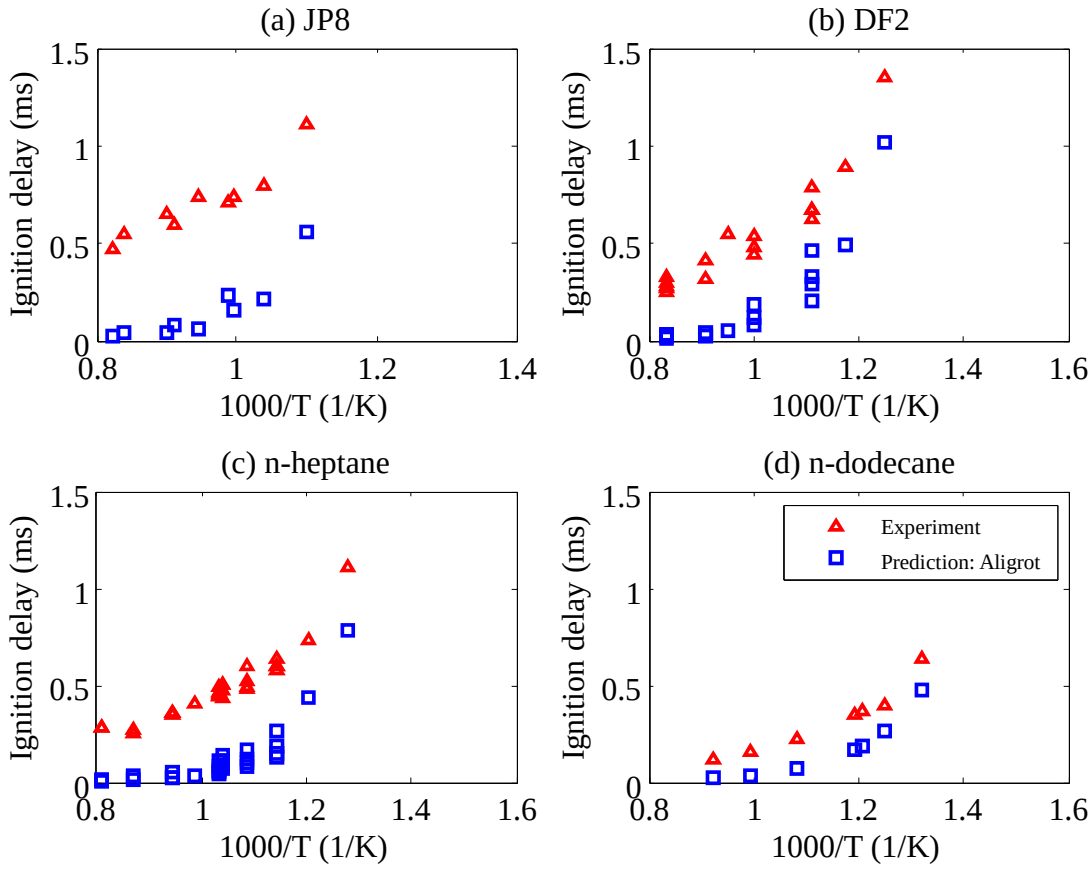

Figure 3.12 Prediction result of Aligrot's ignition delay model scaled to 50 bar and 21% oxygen.

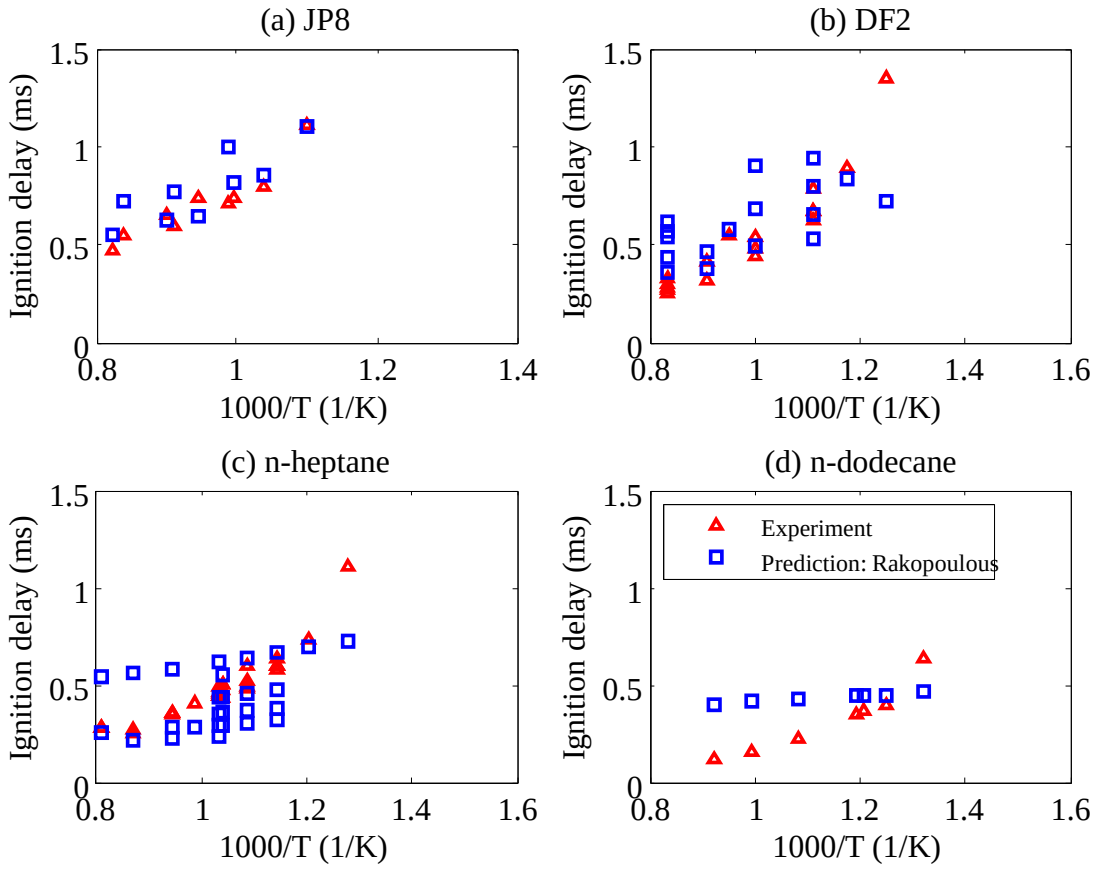

Figure 3.13 Prediction result of calibrated Rakopoulos' ignition delay model scaled to 50 bar and 21% oxygen.

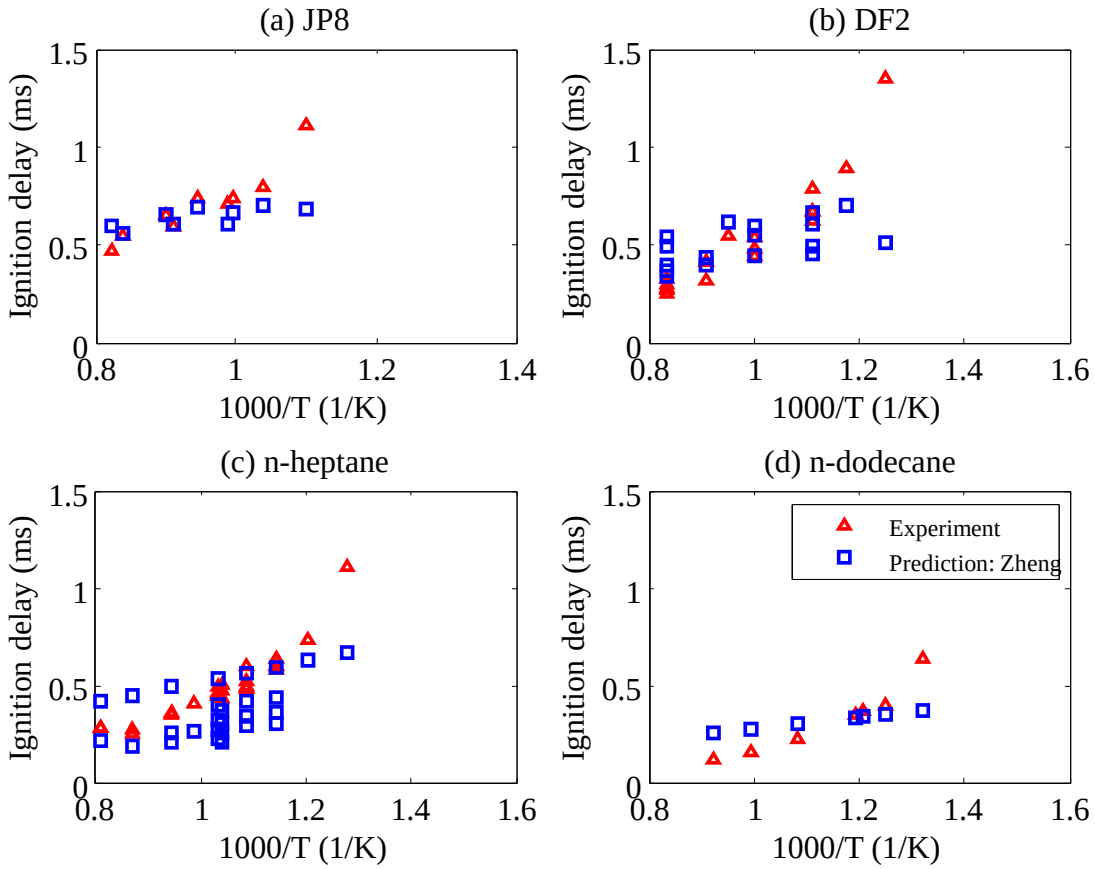

Figure 3.14 Prediction result of calibrated Zheng's ignition delay model scaled to 50 bar and 21% oxygen.

3.3.3 Performance of developed models for other fuels in the ECN

To investigate the performance of the two developed models for other alternative fuels, experimental results of different test fuels, namely, T70, CN80, GE80 and BM88 from the literature [82] are compared with the model predictions. The test data used for the comparison are listed in the Appendix C. These fuels are oxygenated fuels except for CN80 and the ignition delay is measured using the same constant volume chamber setup in Sandia National Laboratory as done with the previous test fuels. The acquisition of the

ignition delay is performed with 21 % ambient oxygen at three different ambient densities (7.3, 14.8 and 30 kg/m^3). The properties of these test fuels are listed in Table 3.1. Ignition delays for these additional test fuels are calculated without re-calibration of the global and the local ignition delay models.

The results illustrated in Figure 3.15 and Figure 3.16 shows that the developed ignition delay models are not suitable for prediction of other fuels without any re-calibration. In both cases, sensitivity with the Cetane number is exaggerated. Thus the predicted results generally show longer ignition delay for T70 and shorter ignition delay for the other fuels compared to the experimental data. In both Figure 3.15 and Figure 3.16 the activation temperatures of the models are smaller than their optimal values to match with the experimental result of for CN80, GE80 and BM88. In addition the deviation comes from the fact that the activation temperature of the models does not explain the sensitivity of the experimental results to the temperature. The scaled experimental results show different temperature sensitivity depending on the ambient air density for fuels like GE80 and T70.

The local model utilizes oxygen and fuel concentrations of local zones. These concentrations are the outcome of enhanced sub-models of multi-zone model, which are capable of capturing physical property differences of each fuel. Only the remainder effects are captured by the calibration of the model. As a result, the local model is a bit more sensitive to the different conditions of the experimental setup. Therefore, this model performs slightly better as seen in Figure 3.16.

The other models in Eqs. (3.19) to (3.22) are also tested with T70, CN80, GE80 and BM88. These correlations are not re-calibrated for the new set of the fuels. The

results are shown in Figure 3.17 to Figure 3.20. They generally do not capture different experimental conditions well. Figure 3.17 shows that current calibration for Wolfer's model is not acceptable for the test fuels. Aligrot's model in Figure 3.18 shows better performances than that shown in previous section. However Cetane number effect is more exaggerated than global or local model results in Figure 3.15 and Figure 3.16. Rakopolous' model in Figure 3.19 shows scattered result but less sensitive to the temperature because initially the model did not have enough variation to the pressure and having small activation temperature. Zheng's model in Figure 3.20 captured pressure effect pretty well but again the overall sensitivity to the temperature is very small which result in much smaller variation in ignition delay compared to experimental data.

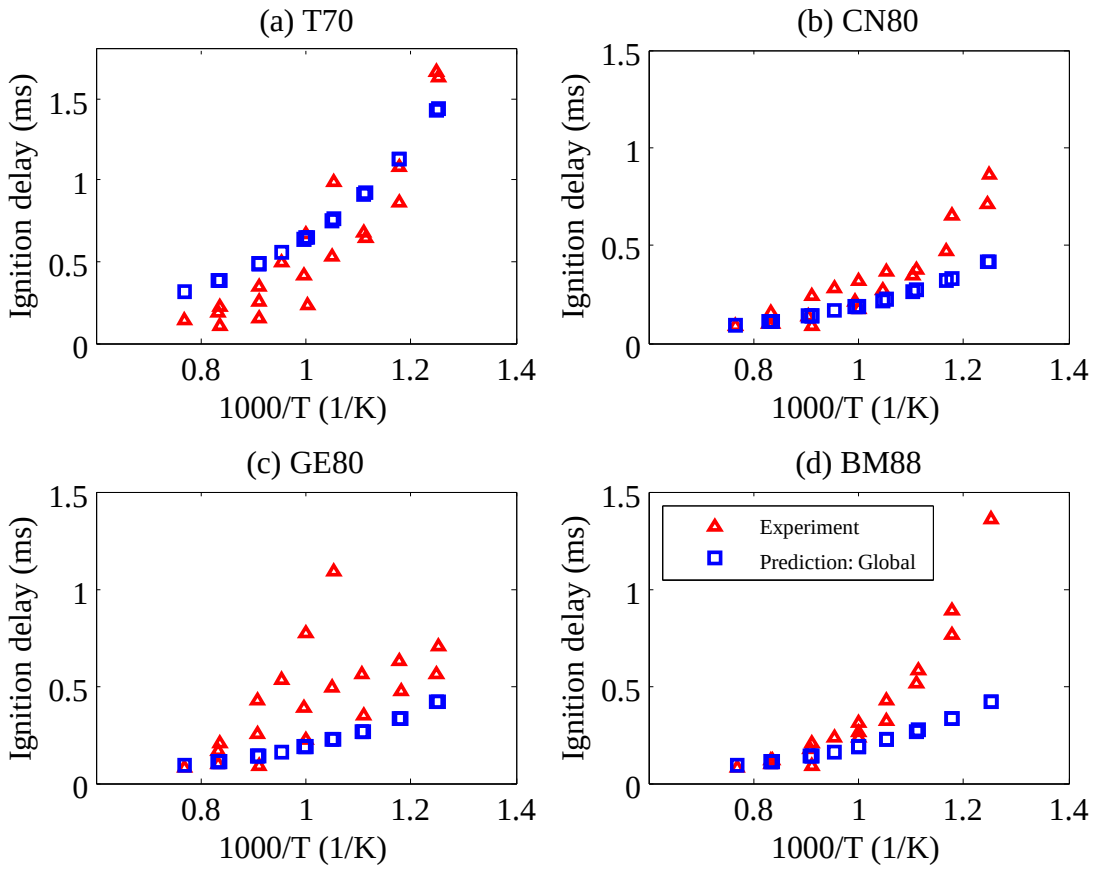

Figure 3.15 Result of global ignition delay correlation scaled to 50 bar and 21% oxygen.

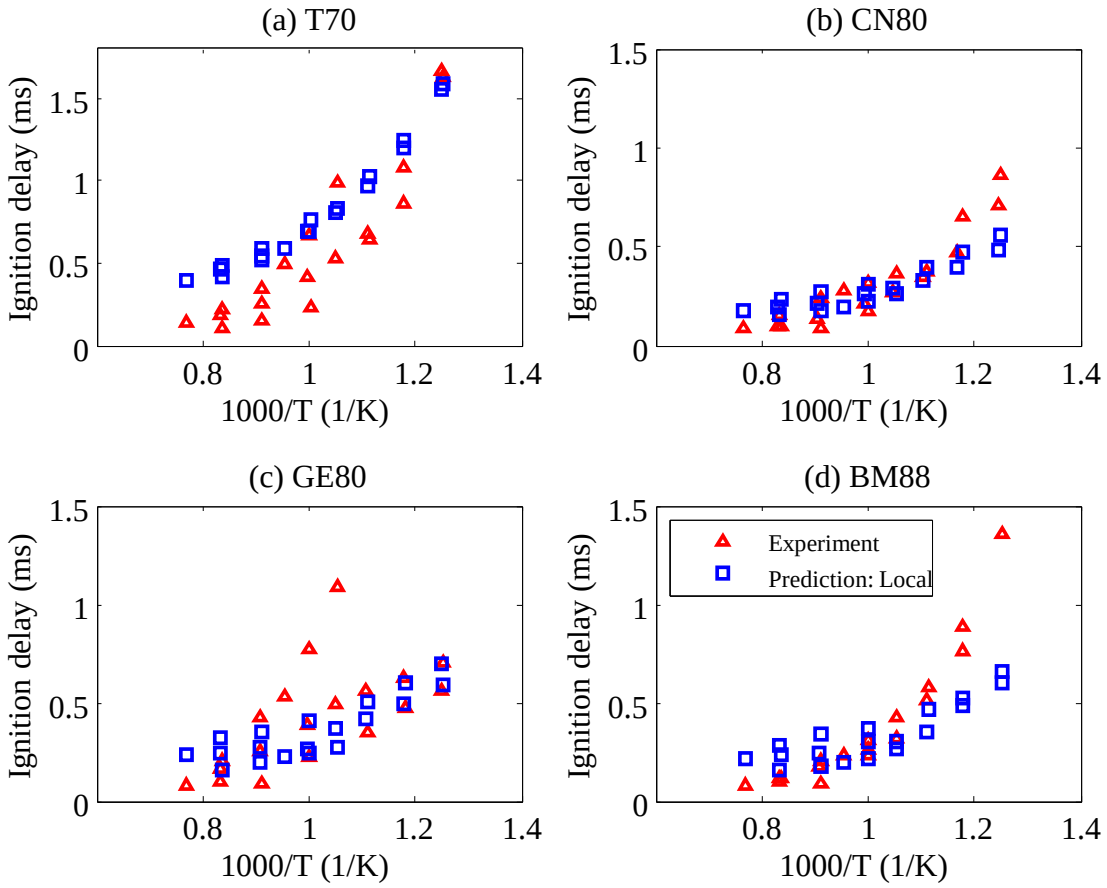

Figure 3.16 Result by local ignition delay scaled to 50 bar and 21% oxygen.

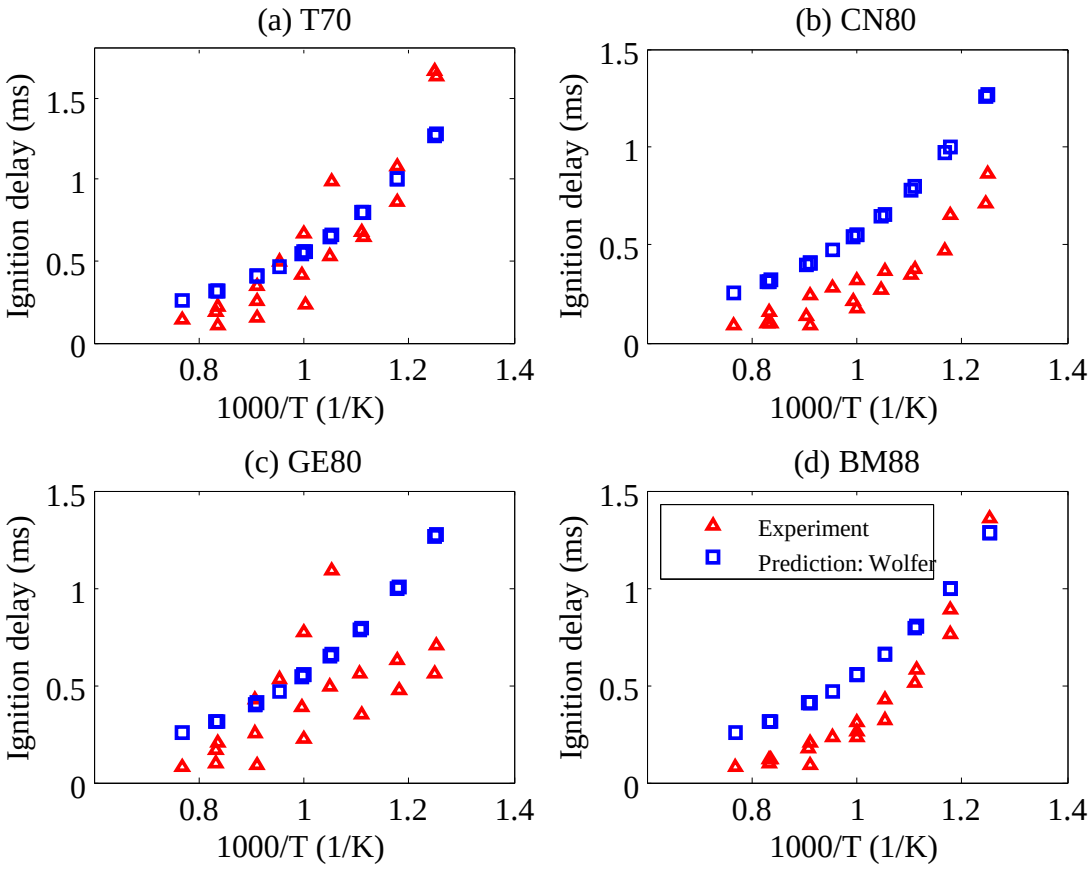

Figure 3.17 Prediction result of Wolfer's ignition delay with T70, CN80, GE80 and BM88 scaled to 50 bar and 21% oxygen.

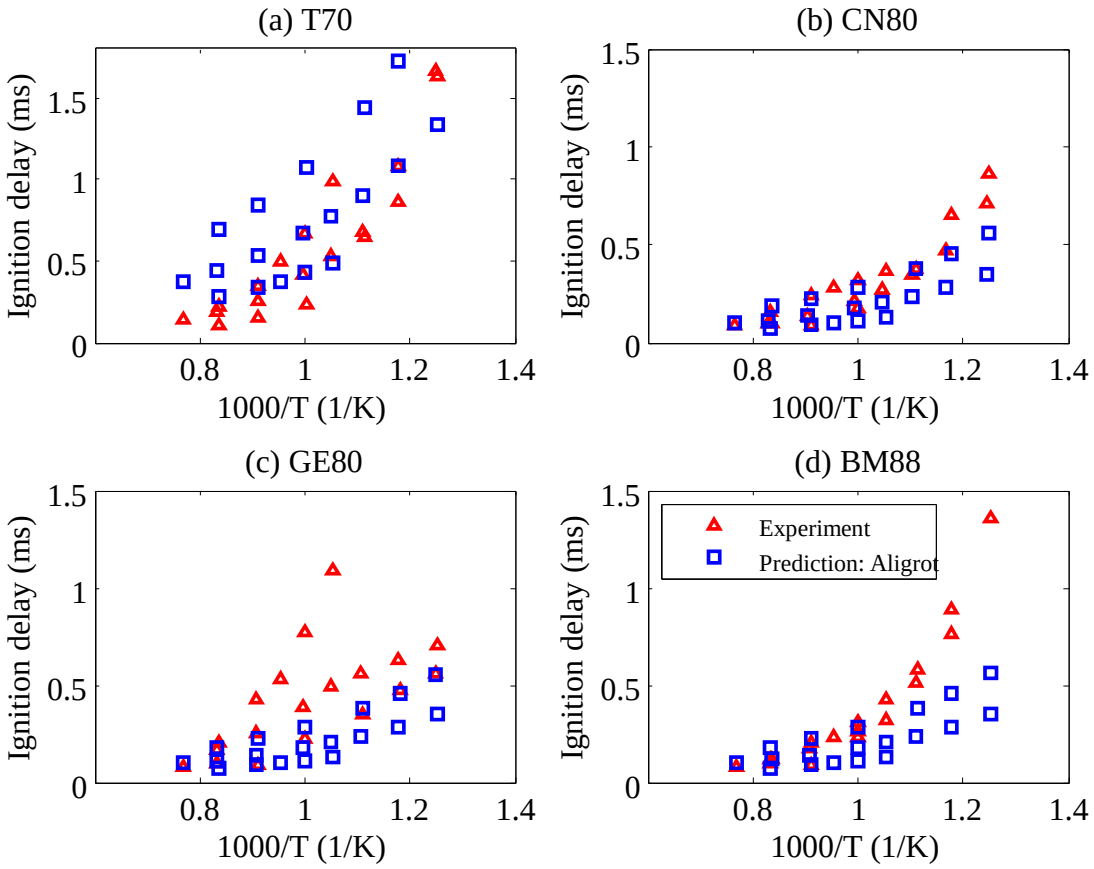

Figure 3.18 Prediction result of Aligrot's ignition delay model with T70, CN80, GE80 and BM88 scaled to 50 bar and 21% oxygen.

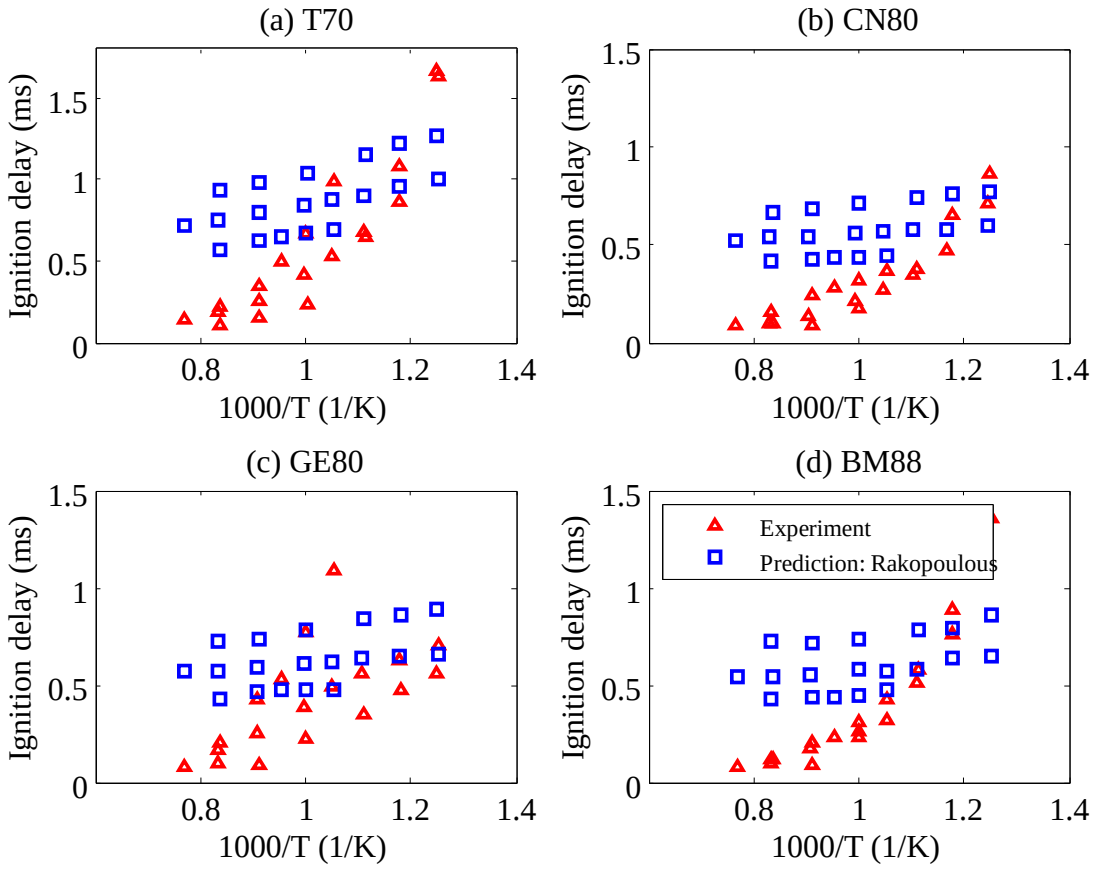

Figure 3.19 Prediction result of calibrated Rakopoulos' ignition delay model with T70, CN80, GE80 and BM88 scaled to 50 bar and 21% oxygen.

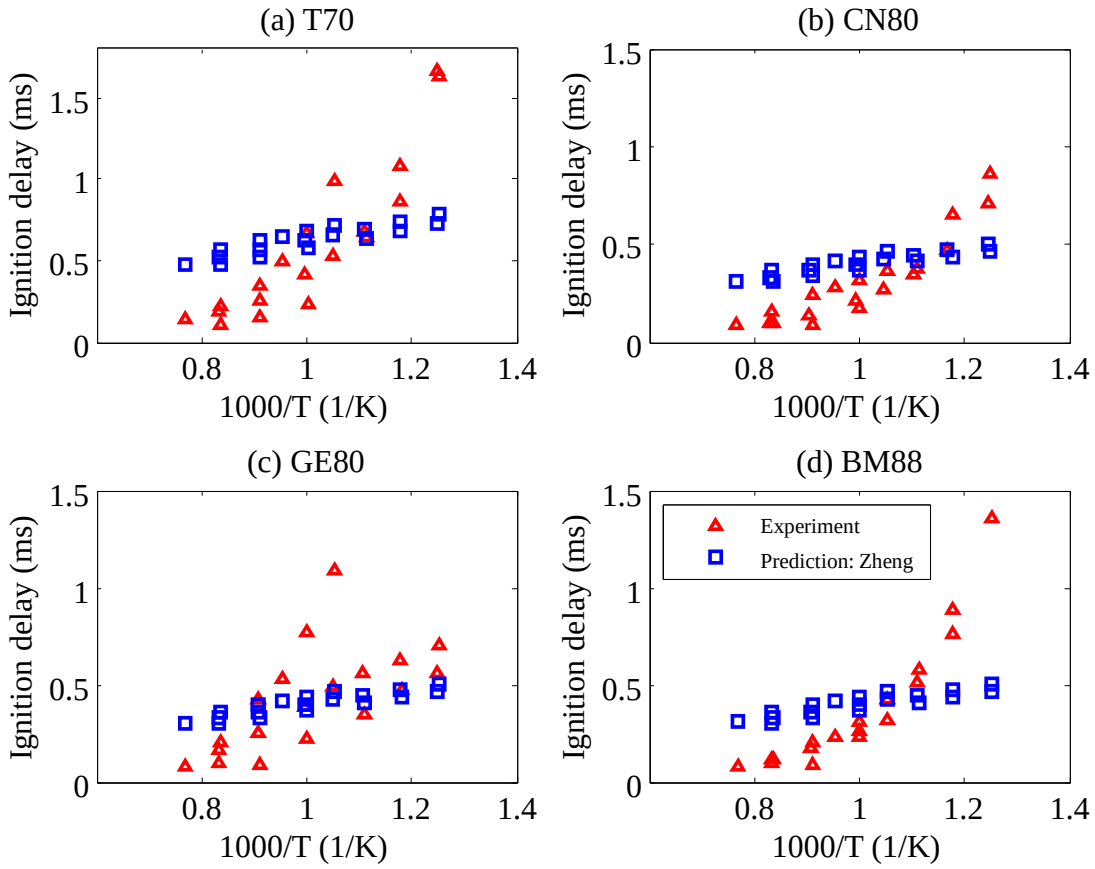

Figure 3.20 Prediction result of calibrated Zheng's ignition delay model with T70, CN80, GE80 and BM88 scaled to 50 bar and 21% oxygen.

3.4 Summary and Conclusion

In this chapter, two fuel-sensitive spray ignition delay models are developed: a global model and a local model. These models follow the Arrhenius type expression modified with the oxygen concentration and Cetane number to extend the range of validity. The models are also sensitive to pressure (density) and dilution, which is important for use in modern engine EGR applications for emission control. Both models were calibrated with four different fuels (JP8, DF2, n-heptane and n-dodecane).

Spray ignition correlations previously developed by others are typically calibrated with a specific fuel, mostly Diesel fuel and they have to be recalibrated if they are intended to be used for different fuels. Unlike the previous models the models and methodology developed in this investigation show very good predictive capability with a single set of calibration parameters for different fuels. The deviations between models and experimental data are significantly less than previous models.

However, the proposed models have a limitation in predicting the ignition delay of synthetic/oxygenated fuels. It was found that the Cetane number is not sufficient to explain the behavior of synthetic/oxygenated fuels and a simple change in the activation temperature cannot cover the behavior either. Additional fuel specific information would be required to extend the proposed models to these other fuels. The proposed models have relatively better predictive capability compared to the existing models for this class of fuels.

Chapter 4

Enhanced combustion modeling method for diluted air-fuel mixture: Scaled premix burn rate model

In this chapter, a method to calculate the burn rate of combustion in the quasi-dimensional multi-zone DICI engine simulation is presented. The premixed combustion model is newly formulated to calculate the burn rate of diluted air and fuel mixtures appropriately. The dilution effect to the combustion is important for simulating a modern DICI engine which employs high rate of EGR flow for emission purposes.

4.1 Scaled premixed burn rate model

Among two phase of spray combustion, pre-mixed combustion is more sensitive to the fuel chemistry. During the ignition delay period, the air-fuel mixtures in each zone are calculated using spray penetration, breakup, air entrainment and droplet evaporation models. Then the burn rate is mostly dominated by the chemical reaction rate. Using a single step global reaction rate in an Arrhenius equation form for premixed burn rate is an adequate method for practical computation time and reasonable accuracy over wide engine operating range. Nishida and Hiroyasu [49] developed a burn rate model for their

multi-zone Diesel simulation using a single step global reaction rate of n-dodecane combustion. The rate of consumed fuel vapor mass is described as follow.

$$\frac{dm_{fb}}{dt} = -A\rho_{mix}^{2} x_{O_2}^{n} x_{fu,v}^{m} \exp\left(-\frac{\theta_p}{T_z}\right) \tag{4.1}$$

where A is a model constant in $m^3/(kg \cdot s)$, ρ_{mix} is density of mixture, x_{O_2} and $x_{fu,v}$ are mass fraction of oxygen and fuel vapor respectively and θ_p is activation temperature.

In this model, the activation temperature is determined as 12000 K based on the extended C-H-O chemical kinetic reaction mechanism [83]. The exponents of mass fractions are determined to have a maximum combustion rate at the stoichiometric condition (when $x_{fu,v}$ = 0.22, n=5 and m=1) of a mixture with pure oxygen and fuel.

However this calibration does not work properly when oxidizer is not pure oxygen and diluted as in case of air. Equation (4.1) does not calculate a peak combustion rate at the stoichiometric condition.

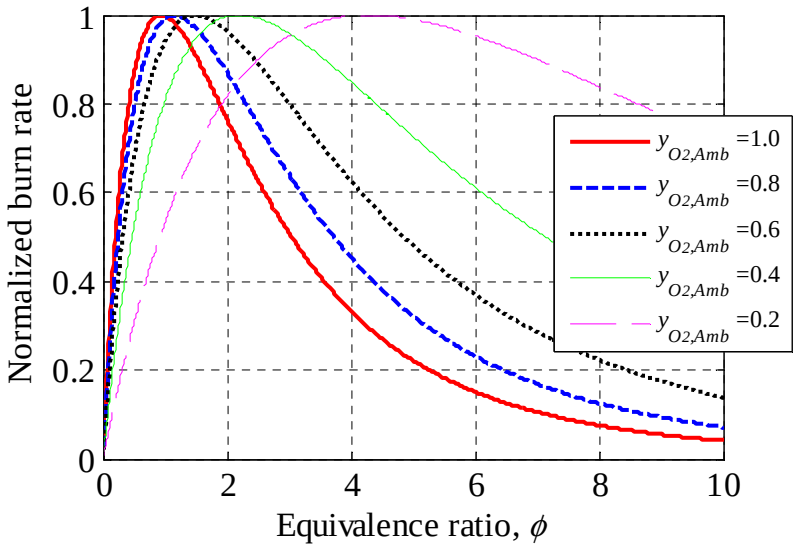

Figure 4.1 Normalized calculation result of Nishida correlation with different oxygen mole fraction in the air.

Figure 4.1 shows normalized burn rates of Nishida correlation at different oxygen mole fraction in the air. In the figure, the peak of the burn rate moves to the richer side as the oxygen is diluted. The maximum burn rate of the correlation at diluted situation can be achieved at stoichiometric condition with re-calibrated exponents of mass fractions. However this calibration increases exponents of oxygen mole fraction much higher (n=16 and m=1 when 21 % of oxygen contains in the ambient) and causes sensitivity of oxygen contents to burn rate becomes irrationally high. In this case slight dilution by EGR flow can cause significantly low burn rate. Thus the burn rate correlation should be reformulated with the equivalence ratio so that the peak of burn rate remains at the stoichiometry without the effect of dilution. Then, the overall rate can be scaled judiciously by the dilution effect maintaining the peak of the burn rate at stoichiometry.

For the new correlation, the normalized burn rate at the mixture of pure oxygen and fuel shown in Eq. (4.1) is taken as a reference and curve fitted. An exponential function given in the following equation is used to describe the normalized burn rate.

$$f_1 = a\phi_{ub}{}^{b} \exp\left(-c\phi_{ub}{}^{d}\right) \tag{4.2}$$

where a, b, c and d is the calibration constants ϕ_{ub} is the equivalence ratio of unburned air and fuel mixture.

This function is made with an intimation from the probability density function of Weibull distribution [84]. Unlike with the Weibull distribution, the exponents and coefficients are not mathematically tied together. The result of regression listed in Table 4.1 shows that the Eq. (4.2) can represent the function shape of normalized Nishida correlation very well.

Table 4.1 Coefficients and goodness of fit of regression

Coefficients	
a	29.95
b	1.577
c	3.406
d	0.4847
Goodness of fit	
R^2	0.9997
Sum of Squared Error	0.03289

The trend of burn rate with different dilution calculated by Nishida model in Eq. (4.1) at stoichiometric is taken as reference for new model development. The oxygen and fuel mass fraction terms in the equation can be reformulated to scale the Eq. (4.2) for dilution effect. The mass fraction terms can be expressed as follow.

$$f_2 = x_{O_2}^n x_{fu,v}^m = \left(y_{O_2} \frac{M_{O_2}}{M} \right)^n \left(y_{fu,v} \frac{M_f}{M} \right)^m \tag{4.3}$$

At stoichiometric condition, the mole fractions in Eq. (4.3) of oxygen and fuel can be also expressed as follows.

$$\begin{aligned} y_{O_2} &= \frac{n_{O_2}}{n_a + n_{fu,v}} = \frac{n_{O_2}}{n_{O_2} / y_{O_2,au} + n_{fu,v}} = \frac{\left(n_{O_2} / n_{fu,v}\right) y_{O_2,au}}{n_{O_2} / n_{fu,v} + y_{O_2,au}} \\ &= \frac{\alpha \cdot y_{O_2,au}}{\alpha + y_{O_2,au}} \\ y_{f,v} &= \frac{n_{fu,v}}{n_a + n_{fu,v}} = \frac{n_{fu,v}}{n_{O_2} / y_{O_2,au} + n_{fu,v}} = \frac{y_{O_2,au}}{n_{O_2} / n_{fu,v} + y_{O_2,au}} \\ &= \frac{y_{O_2,au}}{\alpha + y_{O_2,au}} \end{aligned} \tag{4.4}$$

where *n* is mole number, α is oxygen-fuel molar ratio at stoichiometric condition and y_{O_2au} is oxygen mole fraction in the unburned air of each zone.

By substitute, Eq. (4.4) to Eq. (4.3), the scaling function becomes as follow.

$$f_2 = \frac{\alpha^n y_{O_2,au}^{n+m}}{\left(\alpha + y_{O_2,au}\right)^{n+m}} \left(\frac{M_{O_2}^{\ n} M_f^{\ m}}{M_{avg}^{\ n+m}} \right)_{ST} \tag{4.5}$$

where M is molar mass, M_{avg} is average molar mass of stoichiometric mixture at given oxygen content of ambient air in the zone.

In Eq. (4.5) the dilution effect and the fuel effect are described with the oxygen mole fraction in the zone and stoichiometric oxygen-fuel molar ratio. This equation is independent of equivalence ratio; therefore it can be used to scale Eq. (4.2). In addition, temperature and pressure effects are captured by density term and exponential term with activation temperature in (4.1). Therefore, the scaled pre-mixed bun rate model is expressed as follows.

$$\left(\frac{dm_{f,v}}{dt} \right)_{PRE} = B_p \phi_{ub}^{\ 1.577} \exp\left(-3.406 \phi_{ub}^{\ 0.4847}\right) \frac{\alpha^n y_{O_2,au}^{n+m}}{\left(\alpha + y_{O_2,au}\right)^{n+m}} \left(\frac{M_{O_2}^{\ n} M_f^{\ m}}{M_{avg}^{\ n+m}} \right)_{ST} \times \exp\left(\frac{-12000K}{T_z} \right) \rho_m^2 V_z \tag{4.6}$$

where B_p is calibration parameter in $m^3/kg{\cdot}s$. The coefficient a of Eq.(4.2) is included in the parameter.

The exponents n and m of the scaled pre-mixed bun rate model in Eq. (4.6) are taken as the same as in the Nishida correlation (n=5 and m=1). This calibration will give the same scaling effect as Nishida correlation except for the location of the maximum burn rate

After all the pre-mixed fuel and air, which is prepared during the ignition delay, has been consumed, the rest of fuel in the spray jet (including fuel injected after ignition) starts burning. In this combustion phase, fuel and air needs to be mixed prior to the

combustion and mixing process requires several other processes in addition to mixing itself such as breakup, air entrainment and evaporation. The chemical reaction rate is usually much faster than these processes. Therefore in this 'mixing-controlled' combustion phase, also known as diffusion combustion phase, the mixing process becomes a limiting factor of the overall combustion rate. The heat release of pre-mixed phase usually show high spike due to the rapid combustion. For mixing-controlled combustion phase, the heat release usually shows much longer duration due to the slower burning rate compared to the earlier phase.

The mixing controlled combustion model used in this study is developed by Jung [3]. Usually, the burn rate of this phase is limited by fuel availability, but sometimes when the gas temperature is low enough or the mixture is very lean, so that kinetics slows down exponentially, the combustion rate is limited by chemical kinetics. The following equation describes the rate of combustion at mixing controlled combustion phase.

$$\left(\frac{dm_{fb}}{dt}\right)_{MIX} = B_m m_{fu,v} \frac{P_{O_2}}{P} P^{0.25} \exp\left(\frac{-2500K}{T_z}\right) \tag{4.7}$$

The available fuel and air mixture is calculated from the spray formation air entrainment and evaporation model developed in Chapter 2. This mixture availability competes with the burn rate given in Eq. (4.7). In the simulation, the numerical solution of the equation is taken care to avoid unfeasible solution by the following steps. The available fuel is compared with the burned fuel prescribed by the burn rate in Eq. (4.7). If the available fuel is less that the prescribed burned fuel, the only available fuel will be completely burned with the rate. If the combustion is kinetically limited, the only prescribed burned mass, which is less than the available fuel will be burned with the rate.

4.2 Characteristics of the scaled premixed burn rate model

Experimentally measured burning rate of fuel spray in high spatial resolution is extremely difficult to obtain. Typically the apparent heat release rate is calculated from the engine cylinder pressure traces. This apparent heat release rate is not suitable to validate a burn rate correlation because the burn rate is a comprehensive simulation result from all the other spray models combined. Therefore, a qualitative assessment of the developed pre-mixed burn rate model is presented here.

For the evaluation, the burn rates of n-dodecane fuel and diluted air with oxygen mole fraction at 21 % to 13 % are calculated and presented in Figure 4.2.

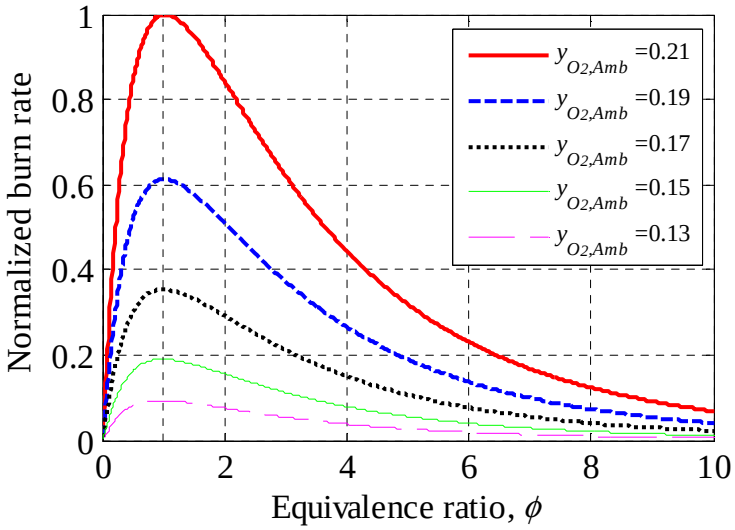

Figure 4.2 Normalized burn rate relative to 21% oxygen case with n-dodecane

The burn rates in the figure are normalized to the peak of 21 % case. As seen in the figure the maximum of burn rate is located at the stoichiometry, while burn rates are reduced as the air is diluted. The flammability limits are implemented with the function used for curve fit in Eq. (4.2). The function decays fast at higher equivalence ratio. In

addition, the function has an infinite tail which provides a numerical stability for the simulation.

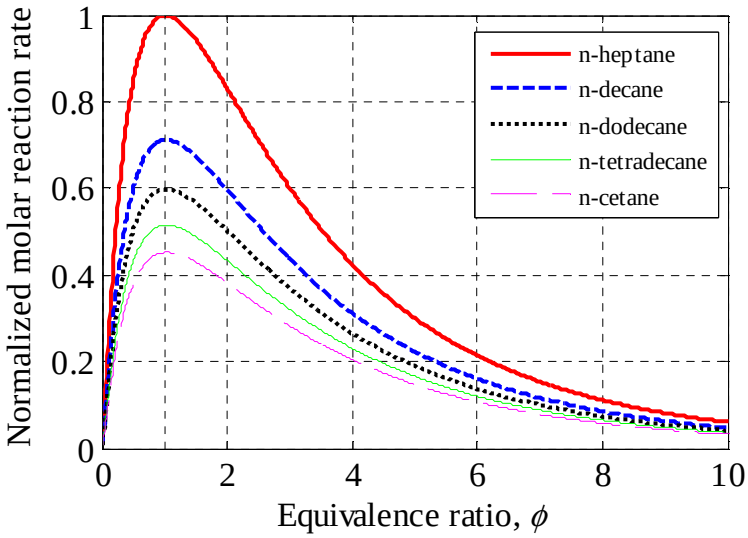

Figure 4.3 Normalized molar reaction rate relative n-heptane case with 21% oxygen mole fraction

Figure 4.3 shows normalized molar reaction rate for five different n-alkane fuels from n-heptane to n-cetane. The ambient oxygen mole fraction is 21 % and the data is normalized to the peak of n-heptane reaction rate. The figure shows that the molar reaction rate of combustion of heavier fuel is slower. This behavior is comparable to other one step global combustion model by Westbrook and Dryer [52]. In their work, one step global reaction mechanism is developed for the combustion of hydrocarbon fuels in flames. The following correlation is used for their reaction rate model.

$$k = A[O_2]^n [F]^m \exp\left(\frac{-E_a}{RT}\right) \tag{4.8}$$

where k is reaction rate in mol/s, E_a is activation energy in kcal/mol and R is universal gas constant: 1.987×10^{-3} kcal/ (K·mol).

Table 4.2 Single step reaction rate model parameters

Fuel	M	α	A*	E_a*	n*	m*
C_5H_{12}	72	8	6.40E+11	30	0.25	1.5
C_6H_{14}	86	9.5	5.70E+11	30	0.25	1.5
C_7H_{16}	100	11	5.10E+11	30	0.25	1.5
C_8H_{18}	114	12.5	4.60E+11	30	0.25	1.5
C_9H_{20}	128	14	4.20E+11	30	0.25	1.5
$C_{10}H_{22}$	142	15.5	3.80E+11	30	0.25	1.5

* Parameters from Westbrook and Dryer [52].

The model parameters for multiple hydrocarbon fuels are obtained by matching laminar flame speed calculation using the reaction mechanism to the experimental data. Table 4.2 shows selected parameters for n-alkanes which have the same activation energy and exponent parameter n and m. The parameter A is found to be correlated with stoichiometric oxygen-fuel molar ratio, α. The goodness of fit R^2 is 0.9968.

$$A = 3.31 \times 10^{12} \alpha^{-0.784} \tag{4.9}$$

Using the parameter A from Eq. (4.9), molar reaction rates for the n-alkane fuels in Figure 4.3 are obtained with Eq. (4.8). The calculated reaction rates are then compared with the result of the scaled pre-mixed burn rate model. Figure 4.4 shows normalized reaction rate calculated from Eq. (4.6) and Eq. (4.8) at stoichiometry with different fuels in pure oxygen and fuel mixture. As seen in the figure, the scaled pre-mixed burn rate model matches remarkably well with the trend of one step global reaction rate model calibrated against different experimental setup.

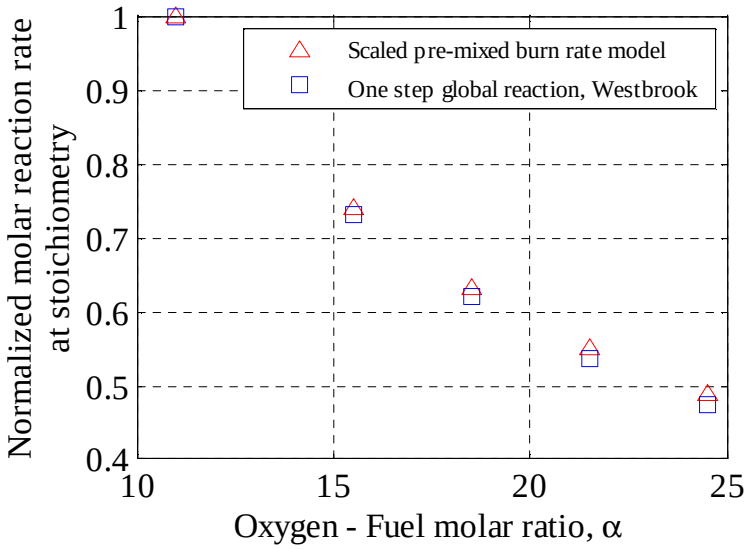

Figure 4.4 Normalized molar reaction rate of scaled premixed burn rate model and Westbrook's one-step global reaction rate at stoichiometric condition in pure oxygen for n-heptane (α =11), n-decane (α =15.5), n-dodecane (α =18.5), n-tetradecane (α =21.5) and n-cetane (α =24.5),

4.3 Summary and conclusion

In this chapter a new scaled premixed burn rate model is presented. Typical Arrhenius equation type premixed burn rate correlation does not have its maximum at stoichiometric with diluted air if it is calibrated with pure oxygen. This can be potentially a problem for EGR application. The proposed model is designed to calculate the rate of burned fuel mass of a premixed combustion appropriately in diluted air with fuel sensitivity. Predictions of proposed model match with molar reaction rate of single step global reaction model calibrated experimentally for different fuels.

The exponential functions used in the proposed model shows slow reaction rate at higher equivalence ratio. The reaction rate is infinitely small but not zero as equivalence

approaches infinite. This characteristic of function works as a flammability limit. In addition the model is numerically more stable than a function using a cutoff equivalence ratio to set the rate zero at the flammability limit.

Chapter 5

Thermodynamic engine cycle simulation integrated with fuel sensitive quasi-dimensional multi-zone combustion models

The engine cycle simulation integrated with quasi-dimensional multi-zone model of a DICI engine is briefly explained in Figure 5.1. The engine cycle simulation consists of four main processes with corresponding sub models which simulate four strokes of the engine. The proposed models in the earlier chapters are implemented in the multi-zone combustion process for the power stroke of engine cycle.

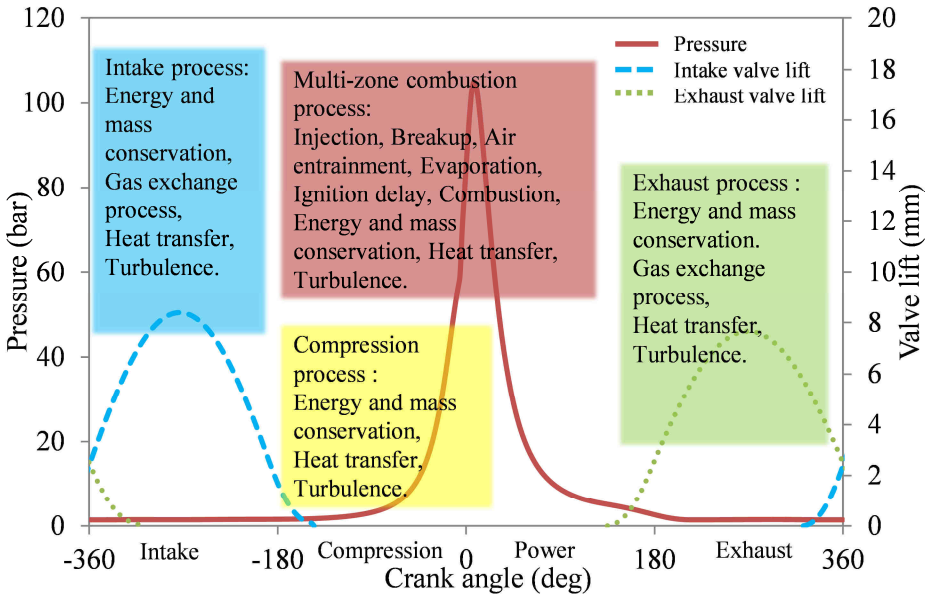

Figure 5.1 Four stroke cycle simulation

The platform for the cycle simulation is developed by Jung [3] using thermodynamic cycle simulation framework developed by Assanis and Heywood [85]. Jung implemented quasi-dimensional multi-zone spray Diesel combustion model into the framework. In this study, the sub models for the Diesel combustion is replaced with proposed fuel sensitive models.

5.1 Background of cycle simulation

The multi-zone thermodynamic Diesel combustion simulation is briefly summarized in this section. Details can be found in the reference [3].

5.1.1 Gas exchange process

The gas exchange processes of the cycle simulation are modeled with one-dimensional quasi-steady state compressible flow model. The model calculates mass flow rate through intake and exhaust valves with tabulated or estimated discharge coefficients using following equation.

$$\dot{m} = C_d A \frac{P_0}{RT_0} \left(\gamma RT_0\right)^{0.5} \left[\frac{2}{\gamma - 1} \left\{ \left(\frac{P_S}{P_0} \right)^{2/\gamma} - \left(\frac{P_S}{P_0} \right)^{(\gamma+1)/\gamma} \right\} \right]^{0.5} \tag{5.1}$$

where C_d is discharge coefficient, A is valve area, P_0 is stagnation pressure upstream of restriction, P_s is static pressure at restriction, γ is specific heat ratio and R is gas constant. If a chocked flow is detected, following equation is used.

$$\dot{m} = C_d A \frac{P_0}{RT_0} \left(\gamma RT_0\right)^{0.5} \left[\left(\frac{2}{\gamma - 1} \right)^{\gamma+1/\gamma-1} \right]^{0.5} \tag{5.2}$$

5.1.2 Heat transfer process

Heat transfer from the cylinder charge to the cylinder wall, piston and cylinder head is also calculated. For the heat transfer, convective heat transfer, $\dot{Q}_c$ from the turbulence flow in the cylinder and the radiative heat transfer, $\dot{Q}_r$ from the flame and burning soot particles are considered. Convective heat transfer is expressed as follow.

$$\dot{Q}_c = hA\left(T_g - T_w\right) \tag{5.3}$$

where A is surface area and h is convective heat transfer coefficient. The convective heat transfer coefficient is calculated from a Nusselt-Reynolds number correlation.

$$Nu = a\,\mathrm{Re}^{d} \tag{5.4}$$

where $Nu = hL/k$ and $\mathrm{Re} = \rho VL/\mu$, a and d is experimentally determined constant. To calculate characteristic length, L, macro scale turbulence is considered. For the characteristic velocity, V, effective velocity due to the contributions from the mean kinetic energy and turbulent kinetic energy and piston motions is used. This is similar to the variations of the heat transfer model by Woshcni [86].

Two radiative heat transfer models are implemented in the cycle simulation and they can be used selectively. The correlation of Annand [87] is expressed as follows

$$\dot{Q}_r = k_r A\left(T_g^4 - T_w^4\right) \tag{5.5}$$

where k_r empirical radiation constant.

The other model is adopted from Assanis and Heywood[85] which calculates radiative coefficient from apparent gray-body emissivity ε_a and Boltzmann constant σ.

$$\dot{Q}_c = \varepsilon_a \sigma A\left(T_g^4 - T_w^4\right) \tag{5.6}$$

5.1.3 Mass and energy conservation

In the power stroke, the multi-zone spray combustion model calculates mass conservation and energy conservation in each zone. Figure 5.2 illustrates the heat and mass fluxes between zones and cylinder walls. In the zone the vapor fuel is considered as an open system. In each system mass transfer from liquid droplet by evaporation, mass transfer by air entrainment, heat transfer to the droplets by evaporation and heat transfer to the cylinder walls are calculated. The air zone outside of spray is also treated as open system with mass transfer to the vapor fuel systems and heat transfer to the cylinder walls are calculated.

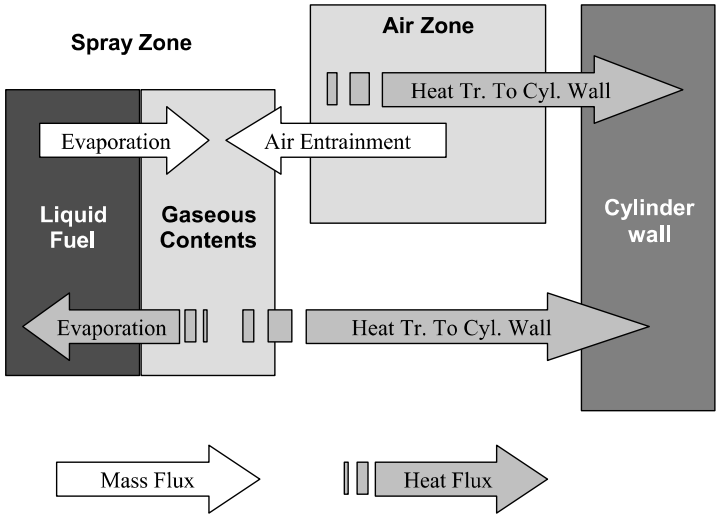

Figure 5.2 Heat and mass fluxes of a zone [3]

The energy equation in the simulation follows the description in Heywood [88]. The air and combustion product mixture inside the cylinder is assumed to be ideal gas and in thermodynamic equilibrium. The first law of thermodynamics in the open system of the engine in quasi-static state is written as follow.

$$\dot{E} = \dot{Q} - \dot{W} + \sum_j \dot{m}_j h_j \tag{5.7}$$

where *j* is number of mass flow in and out of the system. $\dot{Q}$ is total heat transfer rate to the system and $\dot{W}$ is work transfer rate out of the system through the boundary, where the piston is displaced. The work transfer rate is equal to $P\dot{V}$. The change of energy in the cylinder can be expressed as follows

$$\begin{aligned} \dot{E} &= \frac{d}{dt}(mu) \\ &= \frac{d}{dt}(mh) - \frac{d}{dt}(PV) \end{aligned} \tag{5.8}$$

Then, Eq. (5.7) can be rewrites as follows.

$$m\dot{h} = \sum_j \dot{m}_j h_j + \dot{Q} + \dot{P}V - \dot{m}h \tag{5.9}$$

The enthalpy of *h* and the density ρ of the mixture and their rate of changes can be expressed as temperature pressure and equivalence ratio.

$$h = h(T, P, \phi),\ \rho = \rho(T, P, \phi) \tag{5.10}$$

and

$$\dot{h} = \left(\frac{\partial h}{\partial T}\right)_{P,\phi} \dot{T} + \left(\frac{\partial h}{\partial P}\right)_{T,\phi} \dot{P} + \left(\frac{\partial h}{\partial \phi}\right)_{T,P} \dot{\phi} \tag{5.11}$$

$$\dot{\rho} = \left(\frac{\partial \rho}{\partial T}\right)_{P,\phi} \dot{T} + \left(\frac{\partial \rho}{\partial P}\right)_{T,\phi} \dot{P} + \left(\frac{\partial \rho}{\partial \phi}\right)_{T,P} \dot{\phi} \tag{5.12}$$

From the partial derivative of ideal gas law following equation can be obtained.

$$\dot{R} = \frac{1}{\rho T}\dot{P} - \frac{P}{\rho^2 T}\dot{\rho} - \frac{P}{\rho T^2}\dot{T} \tag{5.13}$$

By substituting $\dot{\rho}$ of Eq. (5.13) with Eq. (5.12) $\dot{R}$ is expressed with $\dot{P}$, $\dot{T}$ and $\dot{\phi}$ and together with ideal gas law, the rate of change of pressure can be obtained.

$$\dot{P} = \frac{\rho}{\partial\rho/\partial P}\left(-\frac{\dot{V}}{V} - \frac{1}{\rho}\frac{\partial\rho}{\partial T}\dot{T} - \frac{1}{\rho}\frac{\partial\rho}{\partial\phi}\dot{\phi} + \frac{\dot{m}}{m}\right) \tag{5.14}$$

By expressing energy equation, Eq. (5.9) with Eq. (5.11) and substitute $\dot{P}$ with Eq.(5.14), the rate of change of temperature can be also obtained.

$$\dot{T} = \frac{B}{A}\left[\frac{\dot{m}}{m}\left(1-\frac{h}{B}\right) - \frac{\dot{V}}{V} - \frac{C}{B}\dot{\phi} + \frac{1}{Bm}\left(\sum_j \dot{m}_j h_j + \dot{Q}\right)\right] \tag{5.15}$$

where

$$\begin{aligned} A &= \left(\frac{\partial h}{\partial T}\right)_{P,\phi} + \frac{\partial\rho/\partial T}{\partial\rho/\partial P}\left[\frac{1}{\rho} - \left(\frac{\partial h}{\partial P}\right)_{T,\phi}\right] \\ B &= \frac{1}{\partial\rho/\partial P}\left[1-\rho\left(\frac{\partial h}{\partial P}\right)_{T,\phi}\right] \\ C &= \left(\frac{\partial h}{\partial \phi}\right)_{T,P} + \frac{\partial\rho/\partial\phi}{\partial\rho/\partial P}\left[\frac{1}{\rho} - \left(\frac{\partial h}{\partial P}\right)_{T,\phi}\right] \end{aligned} \tag{5.16}$$

By considering enthalpy flow and heat transfer of each spray zone and air zone, the rates of change of temperature for those zones can be calculated as follows.

$$\dot{T}_i = \frac{\sum_j \dot{m}_{i,j} h_{i,j} + \dot{Q}_i + \left[V_i - \left(\frac{\partial h}{\partial \phi}\right)_{T,P,i}\right]\dot{P} - m_i\left(\frac{\partial h}{\partial P}\right)_{T,\phi,i}\dot{\phi}_i - \dot{m}_i h_i}{m_i\left(\frac{\partial h}{\partial T}\right)_{P,\phi,i}} \tag{5.17}$$

$$\dot{T}_a = \frac{\sum_j \dot{m}_{a,j} h_{a,j} + \dot{Q}_a + \left[V_a - \left(\frac{\partial h}{\partial \phi} \right)_{T,P,a} \right] \dot{P} - \dot{m}_a h_a}{m_a \left(\frac{\partial h}{\partial T} \right)_{P,\phi,a}} \tag{5.18}$$

More details of the modeling method related to the cycle simulation is well described in Jung [3] Assanis and Heywood [85] and Heywood [88].

5.2 Implementation of fuel sensitive models

In this section, the implementation of proposed fuel sensitive model is presented. Methodologies of calculating physical and thermodynamic properties for multi-component fuel are integrated. Calculating air and fuel contents in the cylinder and spray zones are also defined for the proposed ignition delay and combustion models.

5.2.1 Physical and thermodynamic properties

For the fuel sensitive combustion models, physical and thermodynamic properties need to be calculated for the different types of fuel including oxygenated fuels. In the simulation, properties at different temperature and pressure of both liquid and vapor are required. Because estimating real fuel properties in wide ranges of temperature and pressure sometimes inadequate for the simulation, the fuel surrogates are used to achieve flexible and fast calculation for various fuels. A total of 10 different methods to calculate physical properties of multi-component fuel surrogates are employed from multiple references. Table 5.1 presents list of required physical properties and calculation methods briefly. The detailed equations are provided in Appendix A.

Table 5.1 Physical property calculation methods

Properties	Method	Source
Specific heat of liquid fuel	Group contribution method (GCM) - Joback (1984)	Poling [63]
Specific heat of fuel vapor	GCM -Joback (1984)	Poling
Thermal conductivity of fuel vapor	Corresponding state principle (CSP) Chung, et al. (1984, 1988)	Poling
Dynamic viscosity of liquid fuel	Experiment fitting model	API [89] Perry [90], DIPPR [91]
Dynamic viscosity of fuel vapor	CSP Stiel and thodos 1961)	API
Density of liquid fuel	CSP - Rackett (1970)	Poling
Heat of evaporation	CSP - Pitzer et al.	Poling
Vapor pressure	CSP - Lee and Kesler (1975) form	Poling
Diffusion coefficient	Empirical correlation - Fuller, et al. (1965, 1966, 1969)	Poling
Surface tension of fuel	CSP - Sastri and Rao (1995)	Poling

The thermodynamic properties of air and combustion product mixture are calculated using 14 species in a chemical equilibrium program developed by Depcik [92]. The partial derivatives of enthalpy and density of air and combustion products are calculated using the equilibrium program. The integrated thermodynamic properties calculation method is an alternative way of estimating air and combustion product of variety of fuels including oxygenated fuels, to the technique developed by Martin and Heywood [93]. The details are provided in Appendix B.

5.2.2 Calculation of air and fuel contents

The oxygen mole fraction in the air zone is calculated based on the fuel content (the fuel in the form of combustion products) of the intake process. Due to the residual gas of combustion and exhaust gas recirculation (EGR), combustion products exist in the

air inside the cylinder at intake valve closing timing. The fuel mass fraction in the intake air due to the EGR is calculated as follows.

$$F_i = \frac{\dot{m}_{fresh} F_{fresh} + \dot{m}_{EGR} F_{\text{exhaust}}}{\dot{m}_{\text{intake}}} \tag{5.19}$$

where F is defined as m_f/m_{total}, the mass flow rates $\dot{m}_{\text{intake}}$, $\dot{m}_{fresh}$ and $\dot{m}_{EGR}$ indicate intake air, fresh air and EGR flow respectively. F_{exhaus} is fuel fraction at the exhaust which is defined as follow.

$$F_{\text{exhaust}} = \frac{\dot{m}_f}{\dot{m}_{fresh} + \dot{m}_f} \tag{5.20}$$

where $\dot{m}_f$ is fuel flow rate.

In most cases the fuel fraction in the fresh air, F_{fresh} is zero. Therefore Eq. (5.19) is can be expressed as follow.

$$F_i = x_{EGR} F_{\text{exhaust}} \tag{5.21}$$

where x_{EGR} is mass fraction of EGR flow rate in the intake flow.

During the intake process, mass flow into and out of the cylinder is calculated depends on the valve event. The fuel mass fraction F_a in the air zone can be calculated by integrating the following equation.

$$\dot{F}_a = \dot{F}_a + \frac{(F_{\text{flow}} - F_a)\dot{m}_{valve}}{m} \tag{5.22}$$

where F_a is current fuel fraction in the air, F_{flow} is fuel fraction in the intake or exhaust flow, $\dot{m}_{vakve}$ is the mass flow rate though intake or exhaust valve and m is current mass in the cylinder.

At the end of intake process, the oxygen mole fraction of the air zone, $y_{O_2,Amb}$ which corresponds to the fuel fraction, F_a is calculated from chemical equilibrium subroutine. The subroutine takes equivalence ratio as an input parameter. Because the fuel contents is used to calculate fuel fraction including the combustion product, the effective equivalence ratio for the fuel and air mixture can be calculated from the following equation using the stoichiometric air fuel ratio with fresh air.

$$\phi = \frac{F \cdot \left(m_a / m_f\right)_{ST}}{1 - F} \tag{5.23}$$

where $\left(m_a / m_f\right)_{ST}$ is stoichiometric air fuel ratio.

After injection, burned fuel fraction in each zone is used to calculate the properties of combustion product using chemical equilibrium subroutine. The burned fuel fraction for each zone is calculated from the following equation.

$$F_z = \frac{F_a m_a + m_{fb}}{m_z} \tag{5.24}$$

where m_{fb} is burned fuel mass, the mass m_a and m_z are air and total mass of the zone respectively.

In the unburned air and fuel mixture of a zone, oxygen mole fraction and effective equivalence ratio need to be calculate for the burn rate model. Using oxygen mole fraction of the air zone, oxygen mole fraction in each zone is calculated as follow.

$$\begin{aligned} y_{O_2,au} &= \frac{n_{O_2,au}}{n_{au} + n_{ab} + n_{fb}} \\ &= \frac{y_{O_2,Amb}\left(m_{au} / M_a\right)}{\left(m_{au} + m_{ab}\right)/M_a + m_{fb}/M_f} \end{aligned} \tag{5.25}$$

where the subscripts *au* and *ab* indicate unburned and burned air in the zone respectively. M_a and M_f is molar mass for air and fuel respectively.

The effective equivalence ratio for the unburned fuel can be calculated as follows

$$\phi_{ub} = \frac{\left(n_{O_2} / n_{fu}\right)_{ST}}{n_{O_2,au} / n_{fu}} \tag{5.26}$$

5.3 Result of cycle simulation

In this section, the results of engine simulation are compared with two different engine experimental results for the validity and characteristics of the proposed fuel sensitive combustion models in thermodynamic cycle simulation

Salvi *et al.* [94] performed alternative fueled Diesel engine experiment using the experimental setup at the University of Michigan. The engine is 2004 International 6L V-8 Diesel engine equipped with a single variable geometry turbocharger. The engine utilizes exhaust gas recirculation to reduce NOx emission. In addition the injection timing is retarded after top dead center for NOx emission control. The brief engine specification is listed in Table 5.2.

Among the test data, JP8, DF2 and synthetic jet fuel (S8) at low medium and high load cases are used for validation in this study. The test conditions are listed in Table 5.3.

The fuel properties used in the simulation are calculated using fuel surrogates. The composition and the blend ratio for the surrogates are listed in Table 5.4. The surrogate for DF2 and JP8 are the same as that used in Chapters 2 and 3. For S8 two component surrogate is taken from literature [95]. The properties are calculated from property subroutine using the fuel surrogates.

Table 5.2 Engine specification of 2004 International 6L V-8 medium duty diesel engine

Engine specification	
Bore (mm)	95
Stroke (mm)	105
Connecting Rod Length (mm)	176
Compression Ratio	18:01
Maximum Speed (rpm)	3300
Intake Valve Opening (CA deg ATDC)	322
Intake Valve Closing (CA deg ATDC)	-108
Exhaust Valve Opening (CA deg ATDC)	104
Exhaust Valve Closing (CA deg ATDC)	-312
Nozzle Diameter (mm)	0.179
Number nozzle per injector	6

Table 5.3 Test condition of medium duty Diesel engine

	Low load			Medium load			High load		
Engine speed (rpm)	750			1200			1800		
BMEP (bar)	1.5			7			11		
Fuel	DF2	JP8	S8	DF2	JP8	S8	DF2	JP8	S8
Injection timing (deg ATDC)	3.70	4.06	4.32	3.74	4.27	4.67	3.85	4.37	4.72
Injection duration (deg)	2.4	8.9	15.6	2.3	9.0	16.3	2.3	9.2	16.6
Injected fuel mass (mg/cylinder)	11.4	11.6	11.8	34.4	34.3	33.6	50.9	51.6	50.5

Table 5.4 Fuel surrogate blend used in the simulation

	DF2 surrogate	JP8 surrogate	S8 surrogate
Blend ratio for surrogate (mass basis)	n-tetradecane 49.0 %	n-dodecane 82.0 %	n-dodecane 61.67 %
	n-decane 31.0 %	n-tetradecane 18.0 %	iso-octane 38.33 %
	1-methyl naphthalene 20.0 %	n/a	n/a
(n_{O2}/n_f) at stoichiometry	17.49	18.98	15.63
Cetane number	51.4	46.2	58.1

5.3.1 Calibration of the model

The integrated fuel sensitive combustion model is calibrated to the experimental data at a single operating point with DF2 fuel to match apparent heat release rate calculated from pressure data using following the equation from Heywood [88].

$$\frac{dQ_n}{dt} = \frac{\gamma}{\gamma - 1} P \frac{dV}{dt} + \frac{1}{\gamma - 1} V \frac{dP}{dt} \tag{5.27}$$

Since the purpose of calculating apparent heat release rate is not to precisely achieve exact heat release and is to compare simulation to experiment, a simple specific heat ratio correlation is used. The ratio used for both experiment and model calculation is calculated from the following correlation [3].

$$\gamma = 1.338 - 6 \times 10^{-5} T + 1 \times 10^{-8} T^2 \tag{5.28}$$

First of all, the intake air mass at the intake valve closing timing was adjusted manually by changing effective area of valve profile to match the cylinder pressure at that timing. The valve cam profile and exact mass flow rate through the valves are not available for the experimental data; therefore the curve fit of generic cam profile and discharge coefficient calculated using pressure differences between valves were used.

The breakup model shown in Eq. (2.12) has influences mostly on air entrainment because the breakup time determines spray penetration after breakup. Ignition delay also changes slightly by breakup time.

$$t_b = \frac{3.726 B_1 d_n}{\Lambda \Omega} \tag{2.12}$$

The shorter breakup time tend to have more air entrainment and earlier start of evaporation. Therefore duration of premixed burn phase increased with shorter breakup

time .The model time constant B_1 depends on the injector characteristics and could be calibrated to match duration of the premixed burn phase. The value of 7.5 was chosen for B_1.

The local ignition delay model shown in Eq. (3.13) is used for cycle simulation. Only the constant A_z was slightly adjusted to match the ignition delay. It was calibrated to 1.082×10^{-1} $CN^{-1.744}$.

$$\tau_{del}[ms] = A_z \overline{R}^{-n-m} \alpha^{-m} [O_2]^{-n} [F]^{-m} \exp\left(\frac{\theta_z}{T_z}\right) \tag{3.13}$$

The rest of constants in the ignition delay equation are set as the same as the constants in Eq. (3.16): n = -0.8, m = -0.2 and θ_z = 4000.

The burn rate models shown in Eq. (4.6) and Eq. (4.7) changes the peak of each phase of heat releases. These rates are calibrated to match each peak of two phase heat release of experiment at 1200 rpm with DF2 fuel.

Burn rate model of premixed combustion:

$$\left(\frac{dm_{f,v}}{dt}\right)_{PRE} = B_p \phi_{ub}^{1.577} \exp\left(-3.406\phi_{ub}^{0.4847}\right) \frac{\alpha^n y_{O_2,au}^{n+m}}{\left(\alpha + y_{O_2,au}\right)^{n+m}} \left(\frac{M_{O_2}^n M_f^m}{M_{avg}^{n+m}}\right)_{ST} \times \exp\left(\frac{-12000K}{T_z}\right) \rho_m^2 V_z \tag{4.6}$$

Burn rate model of Mixing controlled combustion:

$$\left(\frac{dm_{fb}}{dt}\right)_{MIX} = B_m m_{fu,v} \frac{P_{O_2}}{P} P^{0.25} \exp\left(\frac{-2500K}{T_z}\right) \tag{4.7}$$

The coefficient B_p and B_m of the premixed and mixing controlled burn rate models were determined to 0.5×10^{12} and 700 respectively.

Figure 5.4 and Figure 5.3 shows the comparison of calibrated model prediction and experimental data. Heat release rate in the mixing controlled combustion phase right after premixed combustion slightly overshoots. This was the best match can be achieved by calibrating model parameters. Otherwise the model result fits experimental data very well. R^2 result of comparison is 0.95691.

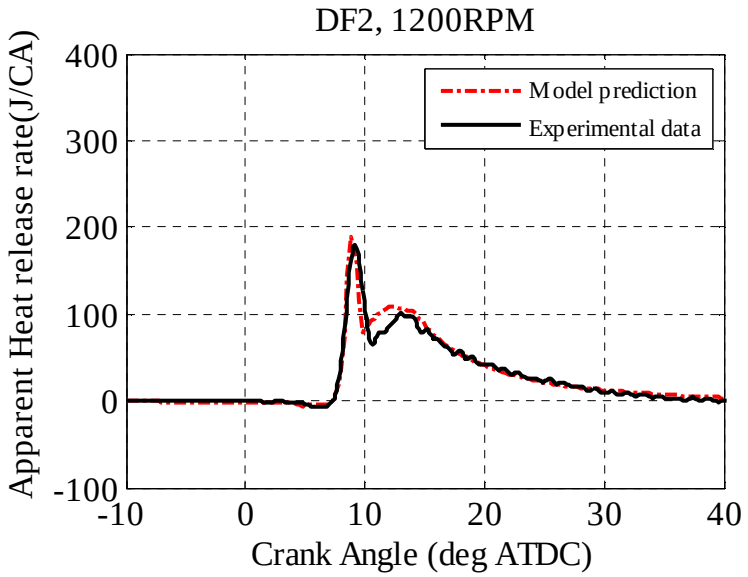

Figure 5.3 Comparison of apparent heat release rate of calibrated model and experiment at the engine speed of 1200 rpm BMEP of 7 bar condition with DF2

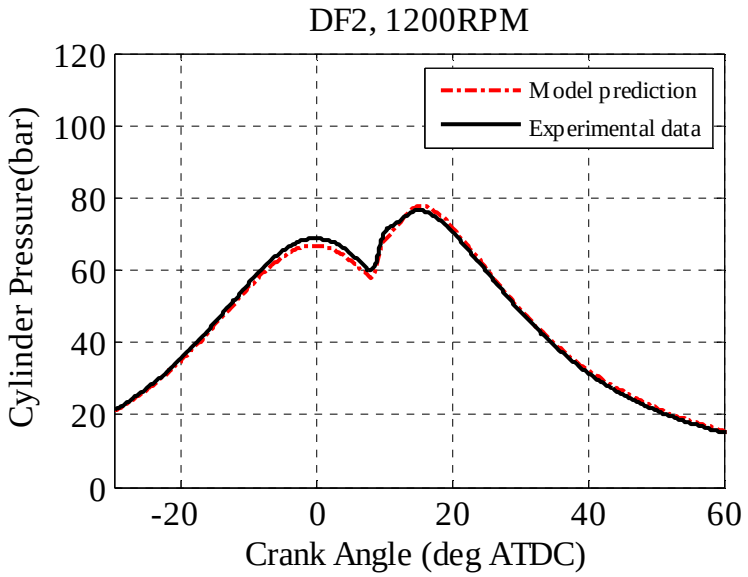

Figure 5.4 Comparison of cylinder pressure of calibrated model and experiment at the engine speed of 1200 rpm BMEP of 7 bar condition with DF2

5.3.2 Validation of the fuel effect

To validate the model capability to capture the fuel effects on the combustion, the apparent heat release rate was calculated and compared to the experimental data. The calibration of the model was kept constant. Figure 5.5 to Figure 5.8 show the apparent heat release rate and cylinder pressure comparisons of JP8 and S8 simulated at 1200 rpm and 7 bar case. The apparent heat release of JP8 in Figure 5.5 shows higher premixed burn rate than DF2 result in Figure 5.3. The premixed heat release rate of S8 in Figure 5.7 is lowest among three fuels. The calculation matches with experimental result well for JP8 while S8 result shows slightly lower premixed heat release rate. Between premixed and mixing controlled combustion phases, there exists a slight overshoot of heat release rates. In S8 case this overshoot is little more pronounced. This is because the premixed burn rate is lower than other fuel cases.

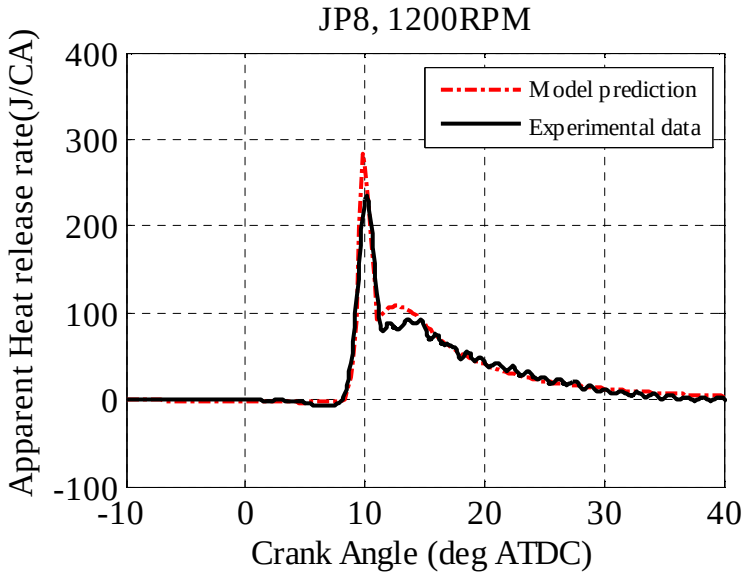

Figure 5.5 Comparison of apparent heat release rate of calibrated model and experiment at the engine speed of 1200 rpm BMEP of 7 bar condition with JP8

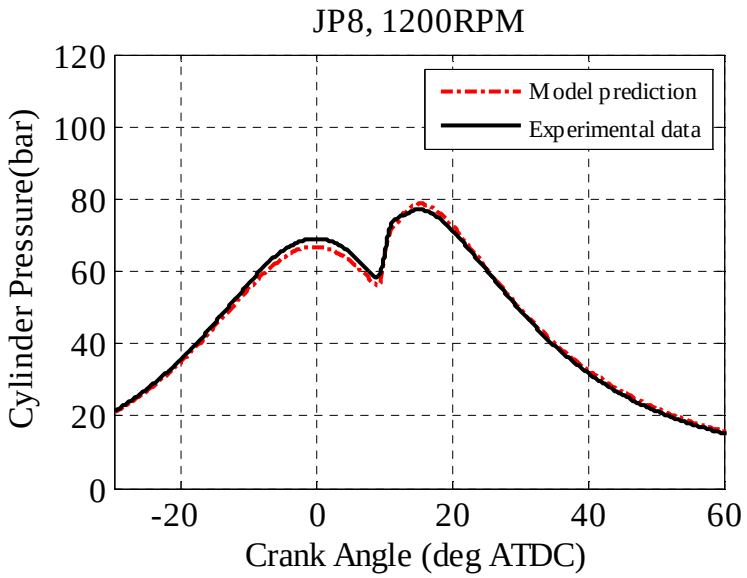

Figure 5.6 Comparison of cylinder pressure of calibrated model and experiment at the engine speed of 1200 rpm BMEP of 7 bar condition with JP8

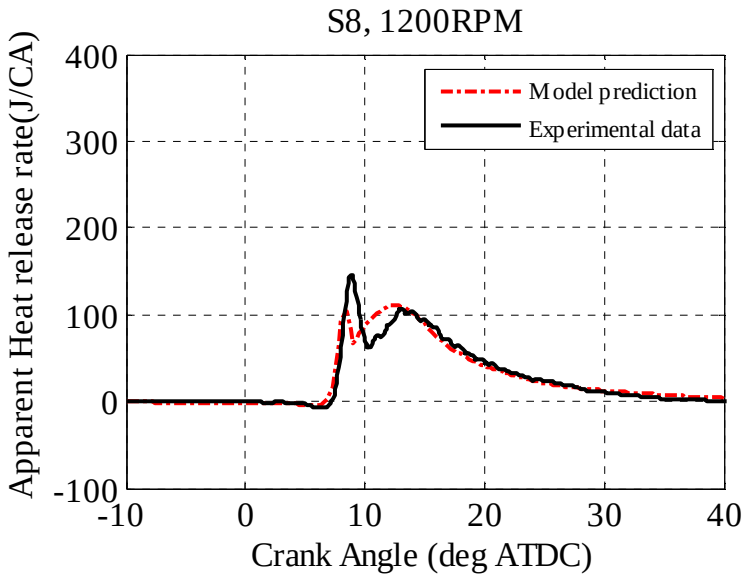

Figure 5.7 Comparison of apparent heat release rate of calibrated model and experiment at the engine speed of 1200 rpm BMEP of 7 bar condition with S8

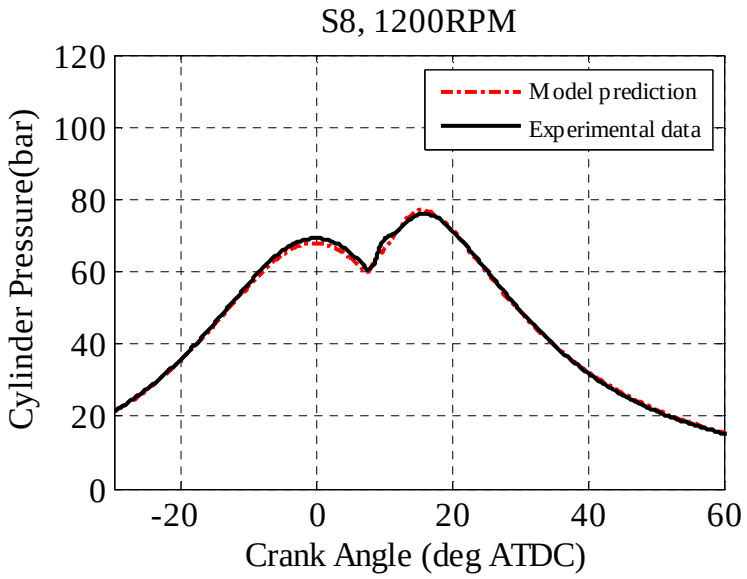

Figure 5.8 Comparison of cylinder pressure of calibrated model and experiment at the engine speed of 1200 rpm BMEP of 7 bar condition with S8

Figure 5.9 shows ignition delay of the three test fuels at the same condition (1200 rpm and 7 bar). The start of combustion (ignition) in the experimental data is defined as the time of the apparent heat release rate crosses zero right before the premixed spike. Ignition delay of DF2 was accurately calculated. The difference is only -0.01 crank angle degree compared to the experiment. For JP8 and S8, the differences are +0.1 and -0.49 crank angle degree respectively. Compared to DF2 fuel, JP8 shows longer ignition delay, and S8 shows shorter ignition delay. Although error S8 is bigger than DF2, the overall result of heat release rate shows that the proposed model in the study is capable of capturing ignition delay trend of different fuels from the experiment. This trend matches with the Cetane number variance of fuels as well. The result also indicates that the differences of the heat release rate of premixed combustion shown in earlier figures (Figure 5.3, Figure 5.5 and Figure 5.7) can be explained by typical effect of ignition

delay; the shorter ignition delay tends to have less premixed heat release because the prepared air and fuel mixtures are small.

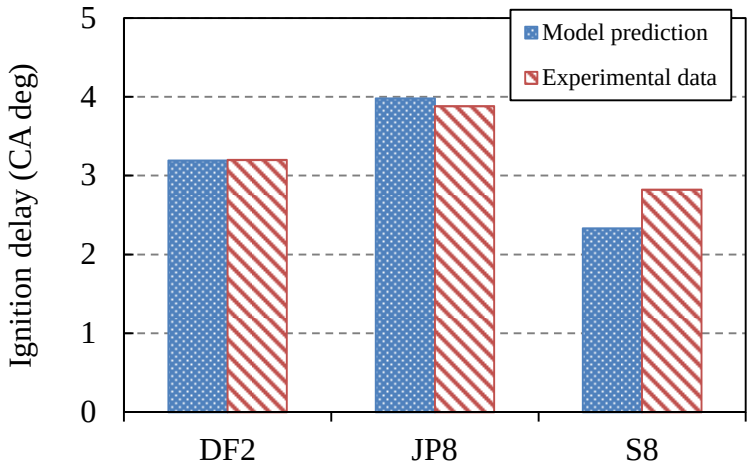

Figure 5.9 Ignition delay of DF2, JP8 and S8 fuels at the engine speed of 1200 rpm BMEP of 7 bar

Figure 5.10 to Figure 5.15 show the comparison of apparent heat release rate of simulation and experimental data at different operating points (750 rpm 1.5 bar and 1800 rpm 11 bar). The simulation was performed with the calibration parameters determined at 1200 rpm 7 bar for DF2 fuel. The premixed heat release rates in 750 rpm cases are slightly higher than experimental result and the rate at 1800 rpm cases are slightly lower than experimental result. In addition, the heat release rates of the mixing controlled combustion phase at 1800 rpm show slight under prediction. Based on the overshooting trends shown in the 1200 rpm cases, the calibration constant for mixing controlled combustion phase is probably not the optimal. In general, the cycle simulation integrated with proposed fuel sensitive models predicts a trend of heat release rate for each fuel at different engine speed and load. Almost all the heat release is oriented from the premixed

combustion at low engine load and the opposite trends are shown in high engine load cases.

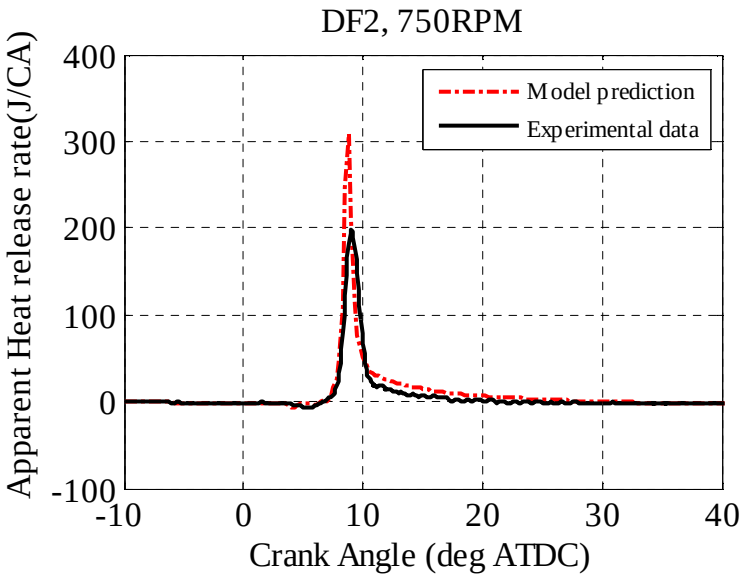

Figure 5.10 Comparison of apparent heat release rate of calibrated model and experiment at the engine speed of 750 rpm BMEP of 1.5 bar condition with DF2

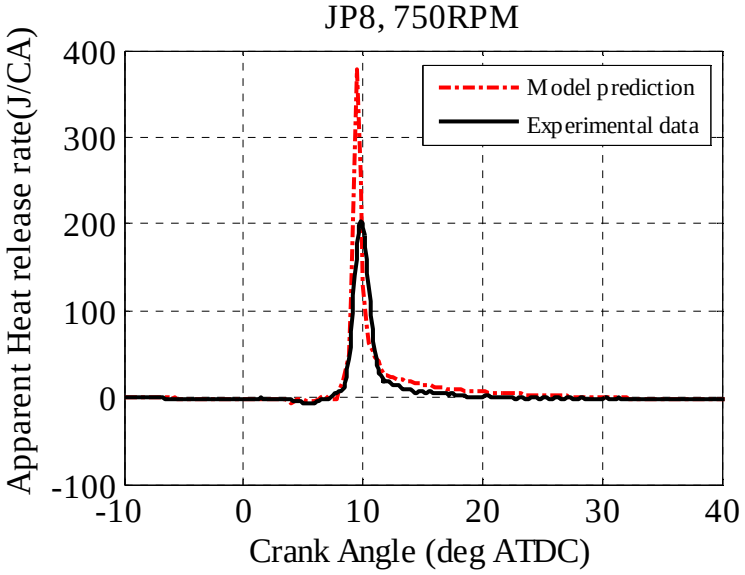

Figure 5.11 Comparison of apparent heat release rate of calibrated model and experiment at the engine speed of 750 rpm BMEP of 1.5 bar condition with JP8

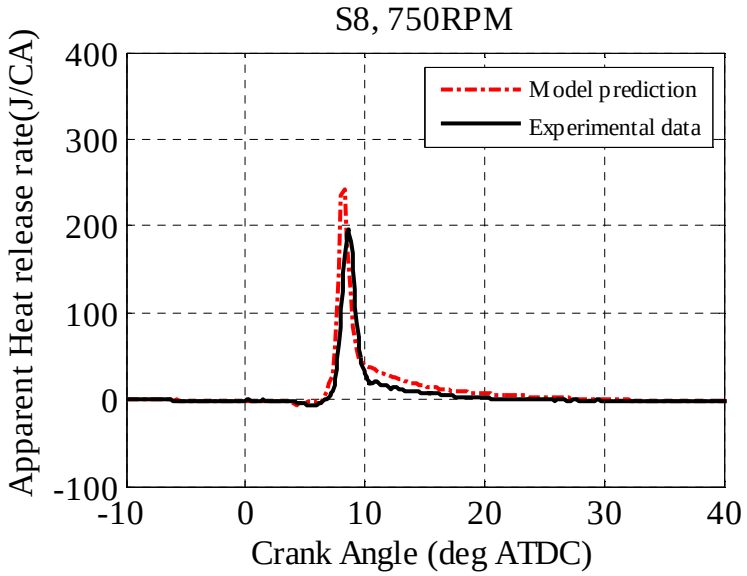

Figure 5.12 Comparison of apparent heat release rate of calibrated model and experiment at the engine speed of 750 rpm BMEP of 1.5 bar condition with S8

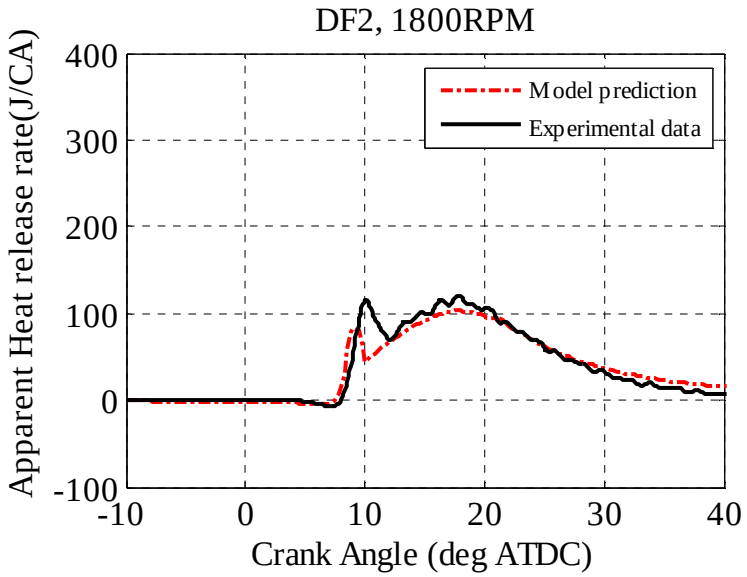

Figure 5.13 Comparison of apparent heat release rate of calibrated model and experiment at the engine speed of 1800 rpm BMEP of 11 bar condition with DF2

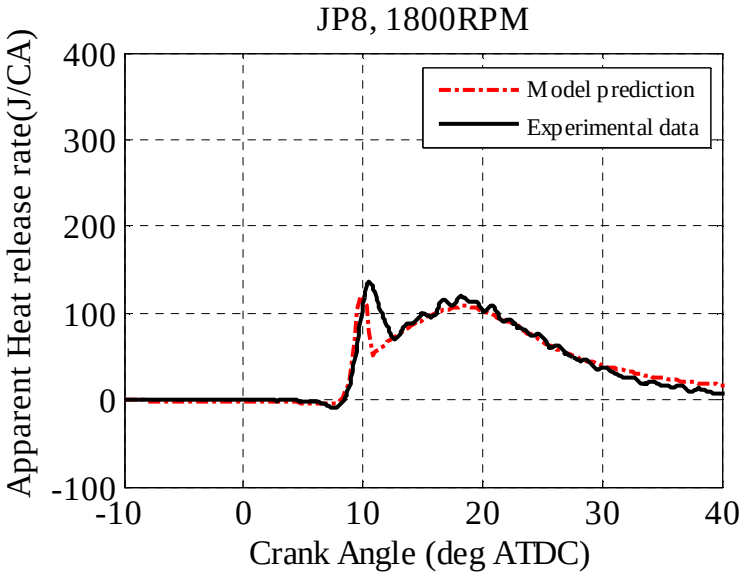

Figure 5.14 Comparison of apparent heat release rate of calibrated model and experiment at the engine speed of 1800 rpm BMEP of 11 bar condition with JP8

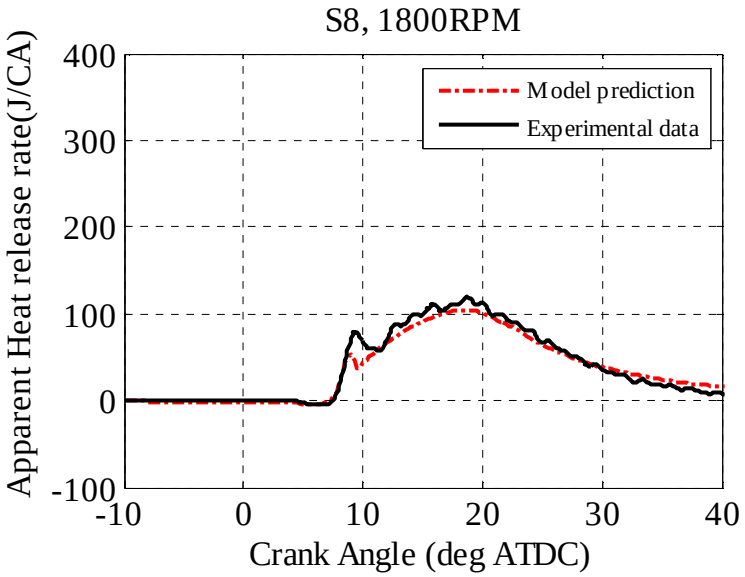

Figure 5.15 Comparison of apparent heat release rate of calibrated model and experiment at the engine speed of 1800 rpm BMEP of 11 bar condition with S8

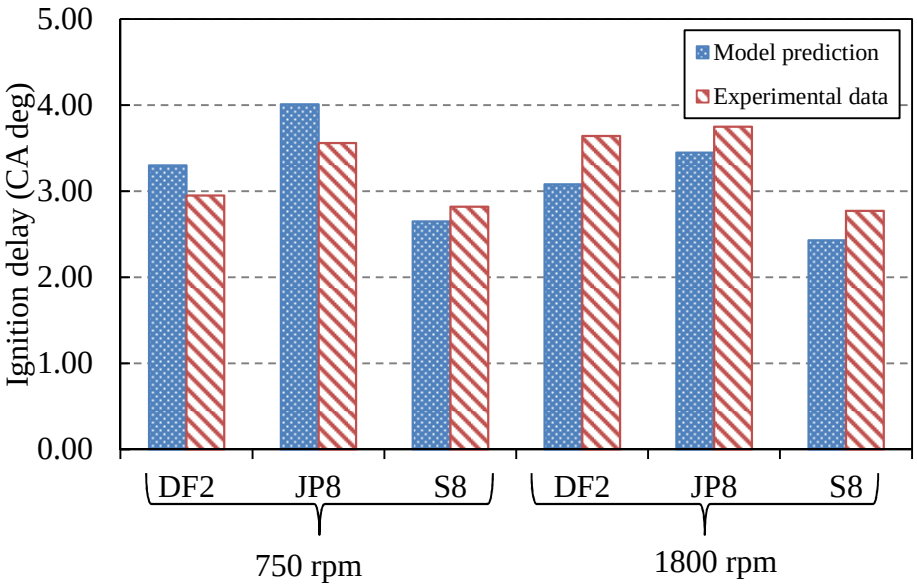

Figure 5.16 Ignition delay of DF2, JP8 and S8 fuels at the engine speed of 750 rpm BMEP of 1.5 bar and 1800 rpm 11 bar

In Figure 5.16, the ignition delay from the simulation is compared with the experimental data. Overall the ignition delay is also well captured for different engine speed and load cases. Table 5.5 shows ignition delay comparison of all nine engine operating points. The maximum error from the simulation is 0.1ms.

Table 5.5 Ignition delay comparison for all nine operating points

Fuel	Engine speed (rpm)	Model prediction (CA deg)	Experiment (CA deg)	Error	
				(CA deg)	(ms)
DF2	750	3.30	2.95	0.35	7.78E-02
	1200	3.19	3.20	-0.01	-1.39E-03
	1800	3.08	3.64	-0.56	-5.20E-02
JP8	750	4.01	3.56	0.45	1.00E-01
	1200	3.98	3.88	0.10	1.39E-02
	1800	3.45	3.75	-0.30	-2.78E-02
S8	750	2.65	2.82	-0.17	-3.78E-02
	1200	2.33	2.82	-0.49	-6.86E-02
	1800	2.43	2.77	-0.34	-3.19E-02

5.3.3 Behavior of fuel sensitive combustion model

To analyze the combustion calculation result easier, ignition delay calculation is bypassed. The start of combustion is given as the same as experimental data.

Comparison with Nishida premixed burn rate model

The model constant of Nishida model in Eq. (4.1) is calibrated to match the maximum premixed heat release rate at 1200 rpm DF2 case: A=1.1 $\times 10^{10}$, n=5 m=1 and θ_p=12000.

$$\frac{dm_{fb}}{dt} = -A\rho_{mix}^{2} x_{O_2}^{n} x_{fu,v}^{m} \exp\left(-\frac{\theta_p}{T_z}\right) \tag{4.1}$$

Figure 5.17 shows the result of simulation at 1200 rpm case with Nishida premixed and the proposed scaled premixed burn rate models. The rate of premixed burn rate of Nishida model shows slightly slow rising rate at the beginning of combustion. This behavior can be also observed in equivalence ratio trace of the zone. Figure 5.18 shows the equivalence ratio of unburned mixture at the tip of the spray (zone index (I,K) =(1,1)). It should be noticed that the apparent heat release rate is the result of all the heat release in the spray zones all together. Therefore, equivalence ratio of a single zone may only represent overall trend in a qualitative manner. Generally equivalence ratio of this zone decreases as air entrains into the zone during the ignition delay period. After ignition equivalence ratio increases little because the burn rate is much faster than evaporation and air entrainment rate.

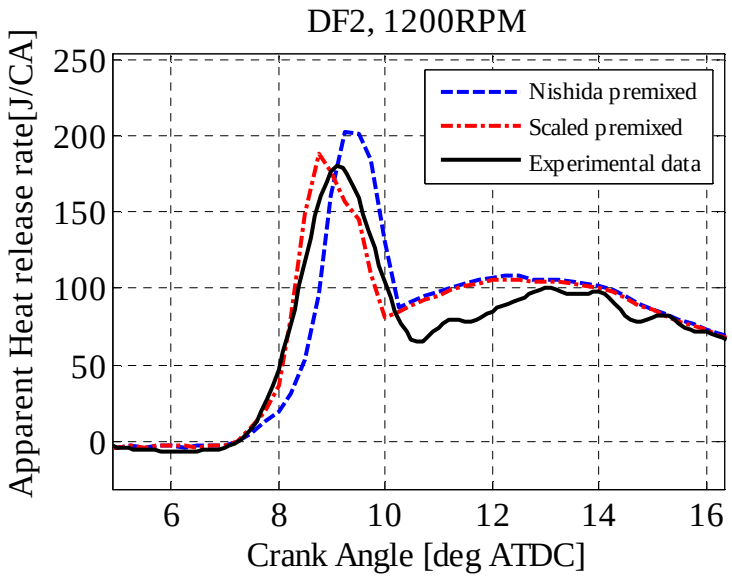

Figure 5.17 Comparison of Nishida premixed bur rate model and scaled premixed burn rate model with experimental result

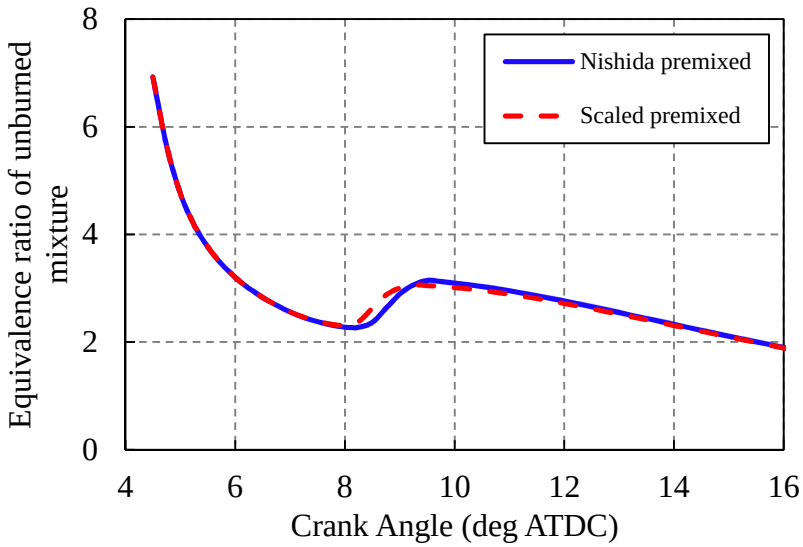

Figure 5.18 History of equivalence ratio at the tip of spray (*I*,*K*)=(1,1)

Ignition delay effect in the combustion

Figure 5.19 shows apparent heat release rate calculated with ignition timing sweep. From the reference the start of combustion time for DF2 1200 rpm case is 7.4 crank angle degree ATDC. The start of combustion (SOC) timing is changed by ± 1 degree. Figure 5.20 shows the heat release rate change by fuel effect. The SOC is fixed at the reference timing, 7.4 crank angle degree ATDC. The fuel effect is captured by spray formation, air entrainment, evaporation and premixed burn rate models. The result shows quite dramatic changes with ignition timing sweep in the premixed heat release rate. The order of variation is much higher than that by fuel effects to the premixed burn rate model shown in Figure 5.20. This comparison demonstrates that the main driver of different fuel effect to the overall combustion is the ignition delay.

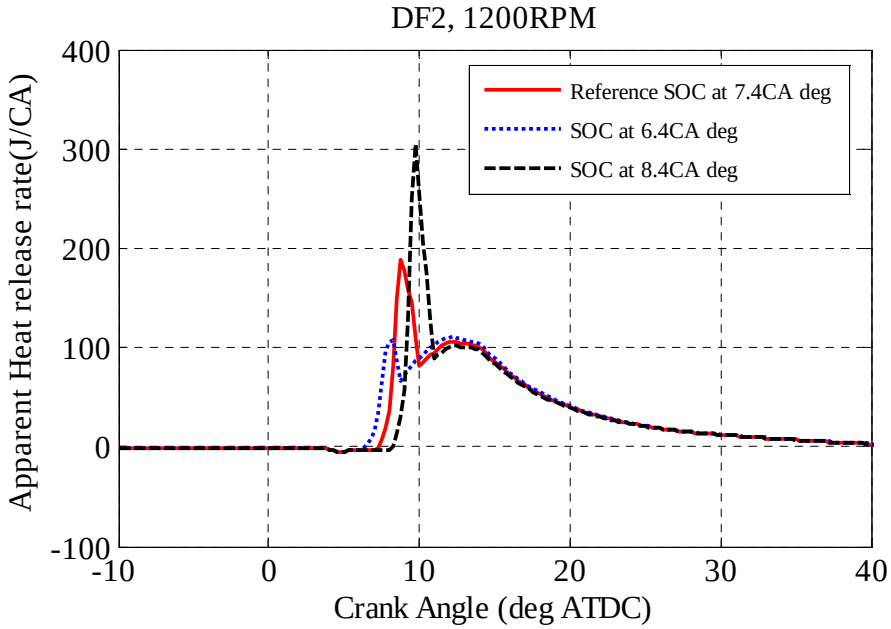

Figure 5.19 Effect of ignition delay.

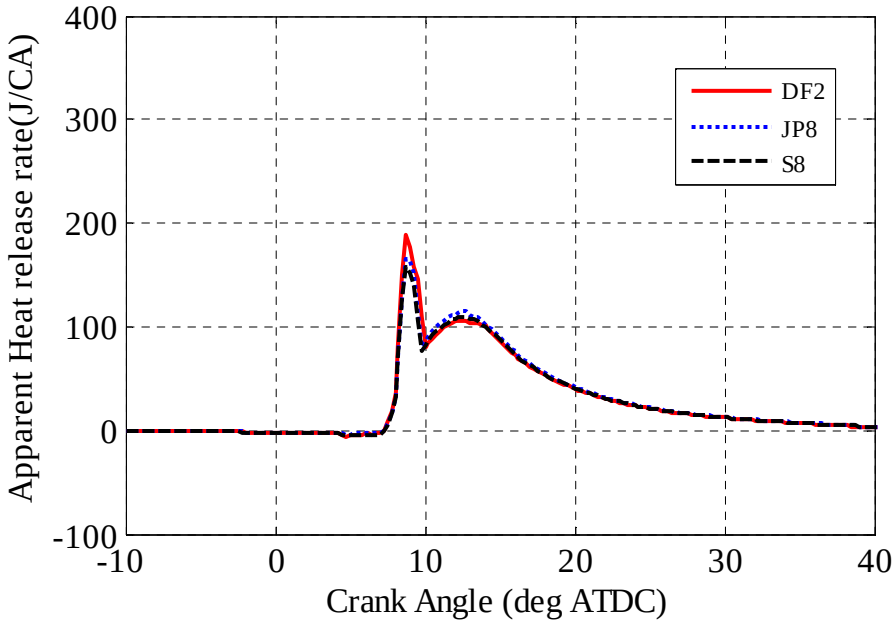

Figure 5.20 burn rate change by fuel effects

5.4 Summary and conclusion

In this chapter, fuel sensitive quasi-dimensional combustion sub models developed in Chapters 2 to 4 are integrated into thermodynamic cycle simulation. The proposed combustion model is able to capture the effect of three different fuels in DICI engine cycles. The predicted ignition delay of the simulation matches accurately with engine experimental data for different fuels. From the apparent heat release rate analysis, slight overshoot and undershoot of the calculation against experimental data are observed. The simulation is also tested without ignition delay calculation. The ignition is specified as an input to observe the combustion model behavior independently. It is found that the ignition delay effect on the combustion is much dominant than fuel sensitive premixed

burn rate model. In the comparison, non-oxygenated fuels (DF2, JP8 and S8) are used thus the proposed ignition delay model is able to predict ignition delay accurately.

The integrated fuel sensitive thermodynamic simulation is designed for large bore engines. Therefore in case of wall wetting condition is not considered. This limitation may require additional calibration procedures.

Chapter 6

Summary, conclusions and recommendations

This chapter addresses summary of this dissertation, conclusions of the study and suggestions for the future work.

6.1 Summary

In this study, the development of fuel sensitive quasi-dimensional multi-zone combustion model for a DICI engine is presented. The models describing each processes of spray combustion are carefully examined and modified or newly developed. The proposed models are validated and compared with experimental results from literature.

Spray evolution process includes breakup, penetration, and air entrainment to the spray. The WAVE breakup model is integrated to replace the traditional Levich breakup model. The WAVE model successfully predicated viscosity and surface tension effect to the spray penetration in the quasi-dimensional multi-zone platform. The zone to zone interaction concept before the breakup is implemented into the spray penetration model. The concept calculates velocities of liquid fuel zones more realistically. The air entrainment is modeled using momentum conservation. In this study, the proposed spray

model is validated by comparing experimental data from literatures with calculated spray penetration and spray angle (spray penetration, spray angle and air entrainment of spray are tied together, thus angle is automatically determined from calculations of the other two models).

Extension of single component droplet model to multi-component evaporation model is done in a simple manner. To avoid excessive calculation, ideal solution and uniform mixture temperature are assumed. Raoult's law is used to calculate the composition of evaporating fuel droplet. The high pressure effect is also considered for the density. Although the developed multi-component model is relatively simple, it can reproduce sizes of evaporating droplets from various experiments well. The behaviors of multi-component evaporation model in engine like ranges of pressure and temperature showed that sensitivity of evaporation to the pressure is inversed at a certain temperature.

Fuel sensitive ignition delay models are developed in a global and local description. The global description utilizes average temperature and pressure, oxygen contents of the air and Cetane number as variables of the model. The local description utilizes zonal information of quasi-dimensional multi-zone spray structure. The local zone temperature, concentration of fuel and oxygen in the zone are used as variables. In addition, the stoichiometric oxygen/fuel molar ratio and Cetane number of fuel are used in the correlation as well. A simple relationship of the model constant is found in a function of Cetane number for four different test fuels. For the oxygenated fuels with same test setup, it is not possible to describe ignition delay with a simple function of Cetane number. An additional effect related to the temperature need to be added for potential improvement of the proposed model.

The scaled burn rate model is developed for premixed combustion. The model is based on the traditional Arrhenius type one-step burn rate model but reformulated to calculate the maximum burn rate at the stoichiometry when air is diluted. The stoichiometric oxygen/fuel molar ratio is also used as a variable for the fuel sensitivity.

The developed spray combustion models are then integrated into the thermodynamic engine cycle simulation. Apparent heat release rates calculated from pressure from the simulation are used to validate the models against experimental data. From the heat release rate results ignition delays are obtained and validated as well. The simulation predicts ignition delay of different fuels very accurately.

6.2 Conclusions

The main conclusions from this dissertation are as follows.

1. The result of developed spray model reveals that the viscosity and surface tension effect to the spray formation and air entrainment is small. Especially, for the fuels relatively close to conventional DF2 fuel (JP8, biodiesel), the effect is minimal for spray formation and air entrainment. The viscosity and surface tension effects are pronounced with the fuel have very low viscosity and surface tension (like DME). In such case the viscosity and surface tension effect need to be considered for the future research.
2. Multi-component evaporation model captures unique pressure effect for evaporation. The evaporation is usually suppressed with higher pressure but the inflection point exists so that in lower temperature higher pressure promotes evaporation. The behavior indicates that in some conditions, such as early

injection or EGR, leading to lower temperatures, this effect is more pronounced. Thus proper evaporation model like the proposed one is required to simulate the combustion more precisely.

3. By introducing temperature, air and fuel contents of the spray zone, the ignition delay is predicted more accurately. Even though developed model has a limitation for predicting wide range of fuels including oxygenated ones, the local ignition delay model have shown the potential of better predictability than global ignition delay model or existing Arrhenius type ignition delay models.
4. The typical pre-mixed combustion model used in diesel combustion modeling is not versatile enough with the diluted air. The new scaled premixed burn rate model properly captures burn rate in diluted air and various fuels.
5. Although the new scaled premixed burn rate model properly calculates burn rate in diluted air and various fuels, the effect of ignition delay to the overall result of engine cycle simulation was much more dominant.

6.3 Suggested future works

Presented work covers modeling of the combustion for DICI engine with alternative fuels from injection of the fuel to end of the combustion. Yet, there is a potential research to extend current work and followings are suggested.

1. For the oxygenated fuel, the ignition delay behaves differently from typical hydrocarbon fuels. It showed additional temperature effect to the ignition delay. The frequency factor of Arrhenius type model could be potentially a function of temperature to capture the effect.

2. Emission analysis is one of the potential future works. The Zel'Dovich's NOx mechanism is included in the quasi-dimensional DICI combustion frame work. With 14 species chemical equilibrium code used in this work, NOx for oxygenated fuel application can also be calculated. In addition to the NOx emission, soot and other emission models can be developed for alternative fuel application.
3. The multi-component evaporation model utilized ideal solution assumption and Raoult's law. It is possible to utilize an equation of state and fugacity for more accurate vapor-liquid equilibrium.
4. Recent effort on optical diagnostic provide measurement of spay environment [96]. Even though the resolution is still not high enough, it could be used to provide some insights of the local equivalence ratio of the spray. Potentially, this data could be used to improve fuel evaporation and air entrainment models.

Appendices

A. Physical properties of multi-component fuel surrogate

The method for estimating the physical properties of the mixture of fuel using pure components properties are explained. Critical temperature and critical compressibility factors and acentric factors of mixture are obtained from Kay's rule [63].

$$\begin{aligned} T_{cm}(\mathrm{K}) &= \sum_i y_i T_{ci} \\ Z_{cm} &= \sum_i y_i Z_{ci} \\ \omega_{cm} &= \sum_i y_i \omega_{ci} \end{aligned} \tag{A.1}$$

The critical molar volume is also calculated by Kay's rule.

$$V_{cm}\left(\mathrm{cm}^3/\mathrm{mol}\right) = \sum_i y_i V_{ci} \tag{A.2}$$

where $V_{ci} = \dfrac{83.144 T_{ci} Z_{ci}}{P_{ci}}$

The critical pressure of the mixture is calculated by following equation.

$$P_{cm}(\mathrm{bar}) = \frac{83.144 Z_{cm} T_{cm}}{V_{cm}} \tag{A.3}$$

1) Specific heat of liquid fuel

Corresponding state principle (CSP) from Bondi (1968) is refitted by Poling et al. [63]

$$Cp_l\left(\mathrm{J}/\mathrm{mol}\cdot\mathrm{K}\right) = Cp^{\circ} + \bar{R}\left[1.586 + \frac{0.49}{T_r} + \omega\left\{4.2775 + \frac{6.3\left(1-T_r\right)^{1/3}}{T_r} + \frac{0.4355}{1-T_r}\right\}\right] \tag{A.4}$$

where Cp^{o} is ideal gas heat capacity of liquid, $\bar{R}$ is universal gas constant equals 8.3144 J/(mol·K). T_r is reduced temperature which equals to T/T_{cm}.

The ideal gas specific heat is calculated from Group contribution method (GCM) developed by Joback (1984).

$$\begin{aligned} Cp^{\circ}\left(\mathrm{J}/\mathrm{mol}\cdot\mathrm{K}\right) = &\left(\sum_k N_k\left(CpAk\right) - 37.93\right) \\ &+ \left(\sum_k N_k\left(CpBk\right) - 0.210\right)T \\ &+ \left(\sum_k N_k\left(CpCk\right) - 3.91\times10^{-4}\right)T^2 \\ &+ \left(\sum_k N_k\left(CpDk\right) + 2.06\times10^{-7}\right)T^3 \end{aligned} \tag{A.5}$$

where N_k indicates number of groups and the following constants are the corresponding values for the group. The group values are taken from the Poling.

For the mixture, molar averaged ideal gas heat capacity is calculated and substituted for Cp^{o} in Eq. (A.4).

$$Cp_m^{\circ}\left(\mathrm{J}/\mathrm{mol}\cdot\mathrm{K}\right) = \sum_i y_i Cp_i^{\circ} \tag{A.6}$$

2) Specific heat of fuel vapor

The fuel vapor is treated as ideal gas and group contribution method in Eq. (A.5) is used. Mixture property is obtained by molar average of ideal gas heat capacity in Eq. (A.6).

3) Thermal conductivity of fuel vapor

Single component thermal conductivity of fuel vapor is obtained using CSP by Chung (1984, 1988).

$$\frac{\lambda M'}{\eta C_v} = \frac{3.75\Psi}{C_v / \overline{R}} \tag{A.7}$$

where

λ = Thermal conductivity, $\mathrm{W/(m \cdot K)}$

M' = Molar mass, kg/mol

η' = Low pressure gas viscosity, $\mathrm{N \cdot s/m^2}$

C_v = Heat capacity at constant volume, $\mathrm{J/(mol \cdot K)}$

$\overline{R}$ = Universal gas constant, $8.3144\ \mathrm{J/(mol \cdot K)}$

$$\Psi = 1 + \alpha \left(\frac{0.215 + 0.28288\alpha - 1.061\beta + 0.26665Z}{0.6366 + \beta Z + 1.061\alpha\beta} \right)$$

$$\alpha = C_v / R\text{-}3/2$$

$$\beta = 0.7862 - 0.7109\omega + 1.3168\omega^2$$

$$Z = 2.0 + 10.5T_r^2$$

Thermal conductivity of mixture is calculated using mass fractions of components.

$$\lambda_m = \sum_i x_i \lambda_i \tag{A.8}$$

4) Dynamic viscosity of liquid fuel

Dynamic viscosity of liquid fuel is obtained from experimental fitting equation. The fitting data is taken from three different sources and corresponding fitting equations are as follows.

(1) American petroleum institute technical data book [89]

$$\begin{aligned} D_{vo} &= 1000.0 \exp\left(a + \frac{b}{1.8T} + c \log(1.8T) + d(1.8T)^e \right) \\ D_{voe} &= -0.0102 + 0.04042 D_{vo}^{\ 0.181} \\ Visc_F\,(\text{Pa - S}) &= D_{vo} \exp\left(\frac{P_{psi} D_{voe}}{1000.0} \right) / 1000 \end{aligned} \tag{A.9}$$

(2) Perry's chemical engineers' handbook [90] and DIPPR [91]

$$Visc_F\,(\text{Pa-S}) = \exp\left(a + \frac{b}{T} + c \log(T) + dT^e \right) \tag{A.10}$$

Mixtures are calculated from mole fractions of components using following equation.

$$Visc_{Fm}(\text{Pa - S}) = \left(\sum_i y_i Visc_{F\,i}^{\ 1/3} \right)^3 \tag{A.11}$$

5) Dynamic viscosity of vapor fuel

Dynamic viscosity of vapor fuel is taken and calculated from following API procedure.

$$\begin{cases} Ann = 3.4\times10^{-4}\left(\dfrac{T}{T_c}\right)^{0.94} & \cdots\cdots \quad T \le 1.5T_c \\ Ann = \left[1.778\times10^{-4}\left(\dfrac{4.58T}{T_c}\right) - 1.67\right]^{0.625} & \cdots\cdots \quad T > 1.5T_c \end{cases}$$

$$EE = \frac{5.4403\left(T_c / 1.8\right)^{1/6}}{M^{0.5}\left(14.5038 \cdot P_c\right)^{2/3}} \qquad \text{(A.12)}$$

$$Visc_G\left(\text{Pa - S}\right) = \frac{Ann}{EE}$$

Mixtures are calculated from mole fractions of components using following equation.

$$Visc_{Gm}\left(\text{Pa - S}\right) = \left(\sum_i y_i Visc_{Gi}^{\,1/3}\right)^3 \qquad \text{(A.13)}$$

6) Density of liquid fuel

Density of liquid fuel is calculated form CSP of Rackett (1970). Saturated liquid density at given temperature at low pressure is calculated from molar volume of the liquid is calculated from following equation.

$$V_s\left(\text{mol}/\text{cm}^3\right) = V_c Z_c^{\left(1-T/T_c\right)^{2/7}}$$

$$\rho_{sat\,s}\left(\text{kg}/\text{m}^3\right) = 1000 \cdot \frac{1}{V_s} M \qquad \text{(A.14)}$$

where M is molar mass in g/mol.

Density of fuel mixture is calculated using critical properties of mixture calculated using Kay's rule. The high pressure effect to the liquid density is applied for the multi-component droplet evaporation in Chapter 2 using compressibility factor.

$$Z_m = Z_m^0 + \omega_m Z_m^1 \tag{2.35}$$

$$\rho_m = \frac{x_{v,s} PM_{v,s}}{Z_m RT_m} \tag{2.36}$$

where R is gas constant for liquid fuel in kJ/(kg·K)

7) Heat of evaporation

Heat of evaporation is calculated using Pitzer CSP from Poling.

$$h_{evap}(\text{J/kg}) = \left[7.08\overline{R}T_c \left(1 - \frac{T}{T_c}\right)^{0.354} + 10.95\omega \left(1 - \frac{T}{T_c}\right)^{0.456} \right] \cdot (1000/M) \tag{A.15}$$

Heat of evaporation of fuel mixture is calculated using critical properties of mixture calculated using Kay's rule.

8) Saturated vapor pressure

Saturated vapor pressure is calculated using Pitzer 2parameter CSP expansion equation from Lee and Kesler (1975).

$$\begin{aligned} F_0 &= 5.92714\text{-}6.09648/T_r\text{-}1.28862\log(T_r)+0.169347T_r^6 \\ F_1 &= 15.2518\text{-}15.6875/T_r\text{-}13.4721\log(T_r)+0.43577T_r^6 \\ P_{sat}(\text{bar}) &= \frac{\exp\left(F_0 + \omega\left(1.0\times10^5 P_c\right)\right)}{1.0\times10^5} \end{aligned} \tag{A.16}$$

Saturated vapor pressure of mixture is calculated based on Raoult's law

$$P_{sat,m}(\text{bar}) = \sum_i y_i P_{sat} \tag{A.17}$$

9) Diffusion coefficient

Binary diffusion coefficient is calculated from empirical correlation by Fuller, et al. (1965, 1966, 1969).

$$D_{AB}\left(\text{cm}^2\right) = \frac{0.00143T^{1.75}}{PM_{AB}^{0.5}\left[\left(\sum v\right)_A^{1/3} + \left(\sum v\right)_B^{1/3}\right]^2} \tag{A.18}$$

where $\sum v$ is atomic diffusion volumes, M_{AB} is average molar mass equals to $2.0 \cdot \left(1/M_f + 1.0/28.97\right)^{-1}$. M_f is molar mass of fuel.

In this study diffusion coefficient for the fuel to air is required thus for the fuel with C, H, O, and N atoms ($C_aH_bO_cN_d$) binary diffusion coefficient is as follows.

$$D_{AB}\left(\text{m}^2\right) = \frac{0.00143T^{1.75}}{1.0\times10^{-4} PM_{AB}^{0.5}\left[\left(15.9a + 2.31b + 6.11c + 4.54d\right)^{1/3} + 19.7^{1/3}\right]^2} \tag{A.19}$$

The diffusion coefficient of fuel vapor mixture is calculated from mole fraction of components.

$$D_{ABm} = \sum_i y_i D_{ABi} \tag{A.20}$$

10) Surface tension

Surface tension is calculated from CSP by Sastri and Rao (1995).

$$\sigma(\mathrm{N/m}) = 1.0\times10^{-3}\,\mathrm{K}P_{\mathrm{c}}^{\mathrm{x}}T_{\mathrm{b}}^{\mathrm{y}}T_{\mathrm{c}}^{\mathrm{z}}\left(\frac{1-T_r}{1-T_{br}}\right)^m \qquad \text{(A.21)}$$

where T_b if boiling temperature and T_{br} equals to $T/T_{b.}$ The values of constants are from Table A.1.

Table A.1 Values of Constants for Sastri-Rao Method

	K	*X*	*Y*	*Z*	*M*
Alcohols	2.28	0.25	0.175	0	0.8
Acids	0.125	0.5	-1.5	1.85	11/9
All others	0.158	0.5	-1.5	1.85	11/9

The surface tension for liqdui mixtures are calculated using mole fraction

$$\sigma_m = \sum_i x_i\sigma_i \qquad \text{(A.22)}$$

B. Thermodynamic properties of combustion product

1) Hot combustion gas equilibrium program

The thermodynamic properties of air and combustion product mixture are calculated using 14 species chemical equilibrium program developed by Depcik [92]. Depcik added two more species NO_2 and HO_2. To the Olikara and Borman program [97]. The code calculates properties of burned gas with respect to temperature, pressure and equivalence ratio.

The global reaction for the fuel with C, H, O and N atoms and oxidizer with O_2, N_3, Ar, CO_2 and H_2O is as follows.

$$y_{15}\left[C_aH_bO_cN_d + \frac{a+0.25b-0.5c}{\phi}\left(\begin{matrix}O_2 + Q_{N_2}N_2 + \\ Q_{Ar}Ar + Q_{CO_2}CO_2 + Q_{H_2O}H_2O\end{matrix}\right)\right] \longrightarrow$$
$$y_1H + y_2O + y_3N + y_4H_2 + y_5OH + y_6CO + y_7NO + y_8O_2 + \quad (B.1)$$
$$y_9H_2O + y_{10}CO_2 + y_{11}N_2 + y_{12}Ar + y_{13}NO_2 + y_{14}HO_2$$

To determine 15 unknown variables in equation above, are solved for four variables using atomic balances constraints and equilibrium equations. Total 15 equations are used. The atomic balance equations are

$$\begin{aligned}
C: &\quad y_6 + y_{10} &&= y_{15}r_3 \\
H: &\quad y_1 + 2y_4 + y_5 + 2y_9 + y_{14} &&= y_{15}r_4 \\
O: &\quad y_2 + y_5 + y_6 + y_7 + 2y_8 + y_9 + 2y_{10} + 2y_{13} + 2y_{14} &&= 2y_{15}r \\
N: &\quad y_3 + y_7 + 2y_{11} + y_{14} &&= 2y_{15}r_1 \\
Ar: &\quad y_{12} &&= y_{15}r_2
\end{aligned} \quad (B.2)$$

Also sum of total mole fraction should equal to unity.

$$\sum_{i=1}^{14} y_i = 1 \quad (B.3)$$

Additionally 9 equilibrium equations are used.

$$
\begin{aligned}
&\tfrac{1}{2} H_2 \Leftrightarrow H && K_1 = y_1 \, P^{1/2} / y_4^{1/2} \\
&\tfrac{1}{2} O_2 \Leftrightarrow O && K_2 = y_2 \, P^{1/2} / y_8^{1/2} \\
&\tfrac{1}{2} N_2 \Leftrightarrow N && K_3 = y_3 \, P^{1/2} / y_{11}^{1/2} \\
&\tfrac{1}{2} H_2 + \tfrac{1}{2} O_2 \Leftrightarrow OH && K_5 = y_5 / y_4^{1/2} \, y_8^{1/2} \\
&\tfrac{1}{2} O_2 + \tfrac{1}{2} N_2 \Leftrightarrow NO && K_7 = y_7 / y_8^{1/2} \, y_{11}^{1/2} \\
&H_2 + \tfrac{1}{2} O_2 \Leftrightarrow H_2O && K_9 = y_9 / y_4 \, y_8^{1/2} P^{1/2} \\
&CO + \tfrac{1}{2} O_2 \Leftrightarrow CO_2 && K_{10} = y_{10} / y_6 \, y_8^{1/2} P^{1/2} \\
&NO + \tfrac{1}{2} O_2 \Leftrightarrow NO_2 && K_{13} = y_{13} / y_7 \, y_8^{1/2} P^{1/2} \\
&O_2 + \tfrac{1}{2} H_2 \Leftrightarrow HO_2 && K_{14} = y_{14} / y_8 \, y_4^{1/2} P^{1/2}
\end{aligned}
\tag{B.4}
$$

These 15 equations can be reduced to 4 equations which are only function of 4 variables.

$$
\begin{aligned}
&y_1 + 2y_2 + y_5 + 2y_9 + y_{14} - \frac{r_4}{r_3}\left(y_6 + y_{10}\right) = 0 \\
&y_2 + y_5 + y_6 + y_7 + 2y_8 + y_9 + 2y_{10} + 2y_{13} + y_{14} - 2\frac{r}{r_3}\left(y_6 + y_{10}\right) = 0 \\
&y_3 + y_7 + 2y_{11} + y_{14} - 2\frac{r_1}{r_3}\left(y_6 + y_{10}\right) = 0 \\
&\sum_1^{11} y_i + y_{13} + y_{14} + \frac{r_2}{r_3}\left(y_6 + y_{10}\right) - 1 = 0
\end{aligned}
\tag{B.5}
$$

Then the Eq. (B.5) is solved by Newton-Raphson iteration technique.

2) Cold combustion gas property calculation

The properties of burned gas less than 600 K can be calculated from simple equilibrium method. Depcik used 7 species equilibrium from Heywood [88]. The reaction is separately written in case of lean and rich condition.

(1) Lean case

$$\phi\varepsilon C_\alpha H_\beta O_\gamma N_\delta + (WO_2 + XN_2 + YAr + ZCO_2) \longrightarrow v_1 CO_2 + v_2 H_2O + v_3 N_2 + v_4 O_2 + v_7 Ar \quad \text{(B.6)}$$

(2) Rich case

$$\phi\varepsilon C_\alpha H_\beta O_\gamma N_\delta + (WO_2 + XN_2 + YAr + ZCO_2) \longrightarrow v_1 CO_2 + v_2 H_2O + v_3 N_2 + v_5 CO + v_6 H_2O + v_7 Ar \quad \text{(B.7)}$$

Detail method for the solving equilibrium methods are presented in Depcik or Heywood. Table B.1 summarizes the result of mole fraction from the program.

Table B.1 Relevant Mole Fractions for Low Temperature Combustion

i	Species	Lean ($\phi \leq 1$)	Rich ($\phi > 1$)
1	CO_2	$\phi\varepsilon\alpha + Z$	$\phi\varepsilon\alpha + Z - v_5$
2	H_2O	$\phi\varepsilon\beta / 2$	$2W - \phi\varepsilon(2\alpha - \gamma) + v_5$
3	N_2	$\phi\varepsilon\delta / 2 + X$	$\phi\varepsilon\delta / 2 + X$
4	O_2	$W(1-\phi)$	0
5	CO	0	v_5
6	H_2	0	$\phi\varepsilon\left(2\alpha + \frac{\beta}{2} + \gamma\right) - 2W - v_5$
7	Ar	Y	Y

Note that 1 mole of Air and fuel are as follows: $WO_2 + XN_2 + YAr + ZCO_2$ and $C_\alpha H_\beta O_\gamma N_\delta$ respectively.

3) Derivatives of thermodynamic properties

Formulation

Derivatives of enthalpy and density in terms of pressure, temperature and equivalence ratio need to be calculated from the properties calculated with chemical equilibrium code. Enthalpy of combustion product charge is calculated by polynomial model with NIST-JANAF table.

$$\frac{h}{\bar{R}T} = a_1 + a_2\frac{T}{2} + a_3\frac{T^2}{3} + a_4\frac{T^3}{4} + a_5\frac{T^4}{5} + \frac{a_6}{T} \tag{B.8}$$

Mixture density is calculated by assuming the charge as ideal gas.

$$\rho = \frac{P \cdot M}{\bar{R}T} \tag{B.9}$$

Using Eqs. (B.8) and (B.9) the derivatives of enthalpy and density are calculated as follows.

$$\begin{aligned}
C_P &= \frac{\partial h}{\partial T}\Big)_{P,\phi} = \frac{d}{dT}\left[\bar{R}T\left(a_1 + a_2\frac{T}{2} + a_3\frac{T^2}{3} + a_4\frac{T^3}{4} + a_5\frac{T^4}{5} + \frac{a_6}{T}\right)\right] \\
C_T &= \frac{\partial h}{\partial P}\Big)_{T,\phi} = \frac{1}{M}\left[\sum_i \frac{\partial y_k}{\partial P}\bar{h}_i - \frac{\partial M}{\partial P}h\right] \\
C_\phi &= \frac{\partial h}{\partial \phi}\Big)_{P,T} = \frac{1}{M}\left[\sum_i \frac{\partial y_k}{\partial \phi}\bar{h}_i - \frac{\partial M}{\partial \phi}h\right]
\end{aligned} \tag{B.10}$$

$$\begin{aligned}
\rho_p &= \frac{M}{\bar{R}T} + \frac{P}{\bar{R}T}\frac{\partial M}{\partial P} \\
\rho_T &= -\frac{P}{\bar{R}T^2} + \frac{P}{\bar{R}T}\frac{\partial M}{\partial T} \\
\rho_\phi &= \frac{P}{\bar{R}T}\frac{\partial M}{\partial \phi}
\end{aligned} \tag{B.11}$$

Validation

The equilibrium code and derivatives calculation code are validated by comparing the results using CEA (Chemical equilibrium with application) program. CEA (Chemical equilibrium with application) is a web application from NASA which calculates chemical equilibrium of various fuel and air. URL: http://cearun.grc.nasa.gov/. The results are also compared with traditional thermodynamic property calculation method developed by Martin and Heywood [93]. This method is intended to calculate traditional hydrocarbon thus the program cannot calculate properties of oxygenated fuel. Test fuel used in this validation is Dimethyl ether (C_2H_6O). Overall, thermodynamic property and its derivatives calculated for Depcik equilibrium program works well with oxygenated fuel and is suitable for the objective of current study.

(1) Mole fraction of burned fuel products

Figures B.1 to B.3 shows mole fractions comparison from temperature sweep comparison of Depcik and CEA program at the pressure of 50 bar and equivalence ratio of 0.5. The CEA utilize 156 species equilibrium for DME fuel. The results are differ by only 0.05 % to 0.1 % .

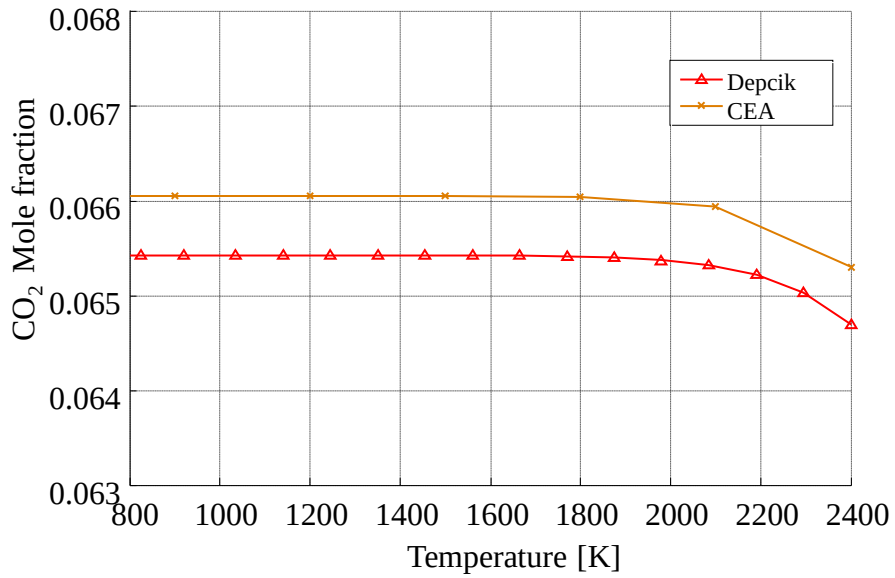

Figure B.1 CO_2 mole fraction comparison

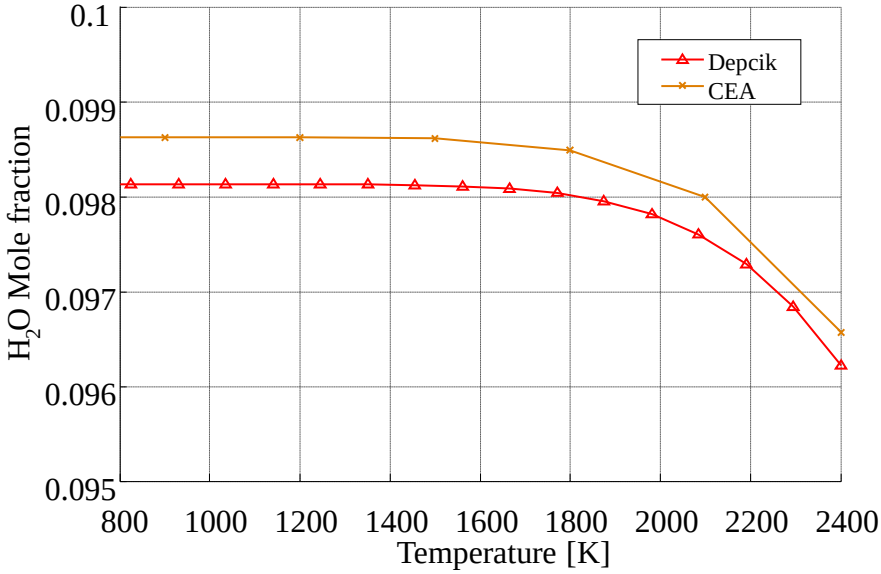

Figure B.2 H_2O mole fraction comparison

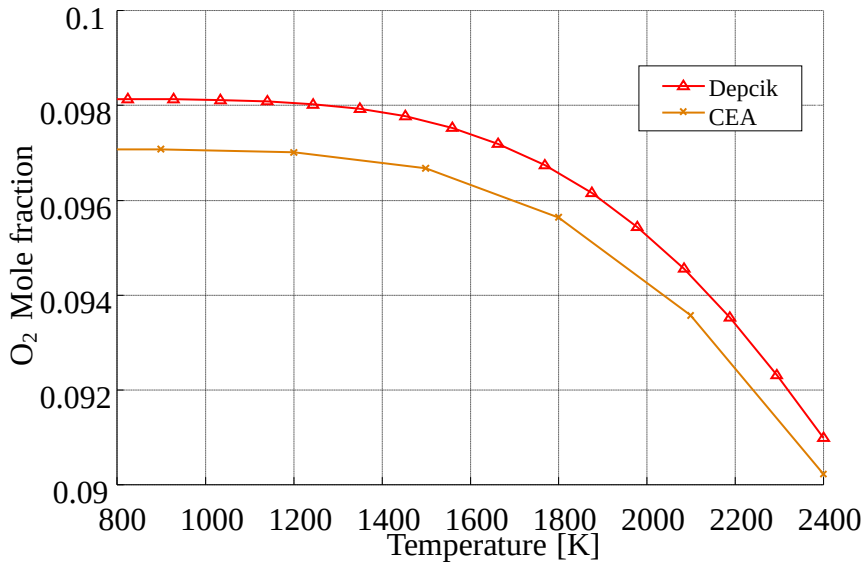

Figure B.3 O_2 mole fraction comparison

(2) Enthalpy of burned fuel products comparison

Figures B.4 to B.6 show the comparison result between Depcik, Martin and Heywood and CEA calculations. Results of Depcik program matches well with CEA, but results of Martin and Heywood are biased from others. This is because the test fuel is oxygenated fuel and the Martin and Heywood program is not designed to calculate burned product properties of such fuels.

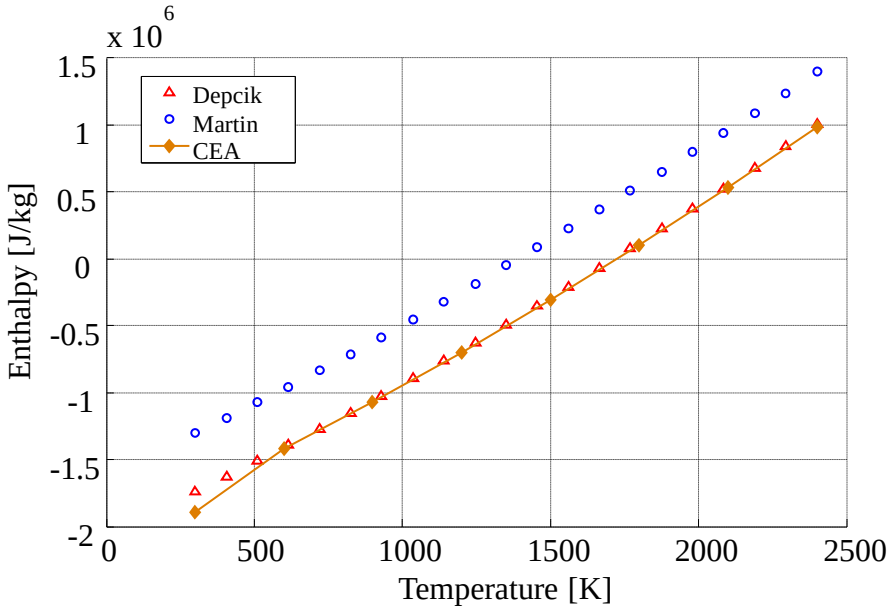

Figure B.4 Enthalpy comparison at 50 bar and equivalence ratio of 0.5

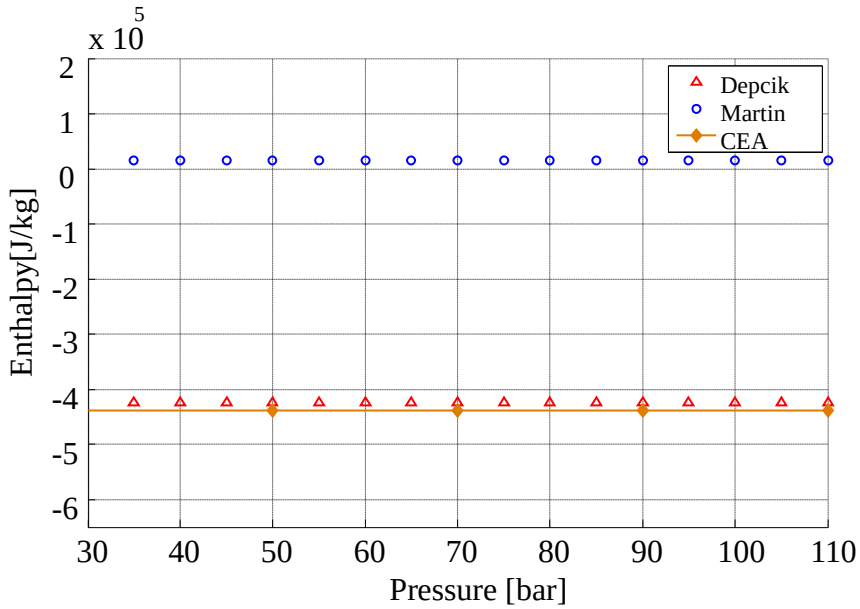

Figure B.5 Enthalpy comparison at 1400K and equivalence ratio of 0.5

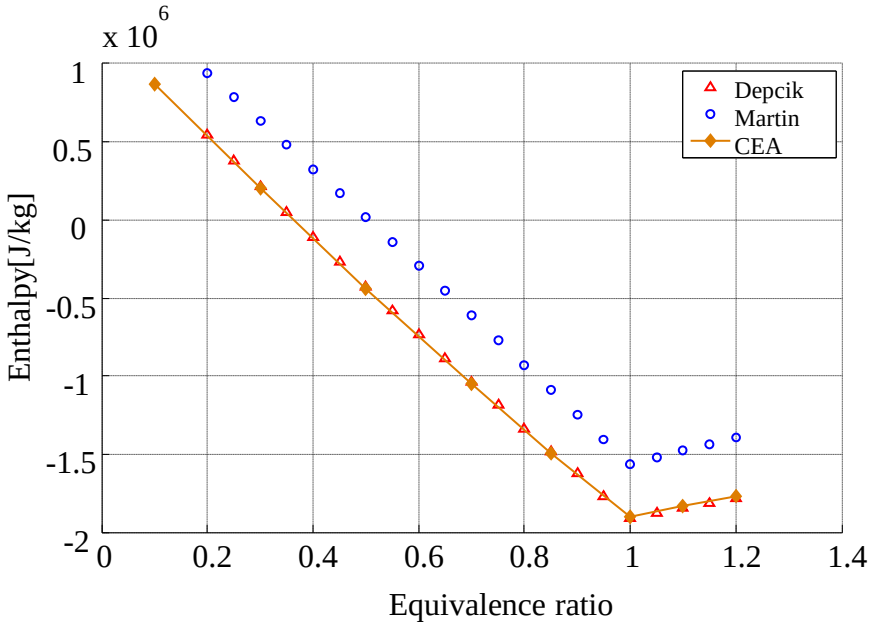

Figure B.6 Enthalpy comparison at 1400K and 50 bar

(3) Derivatives of enthalpy of burned fuel products

Figures B.7 to B.9 shows three derivatives of enthalpy calculated by three different methods. Derivatives of CEA results are calculated numerically while others are analytically calculated. Again, derivatives calculated using Depcik program matches well with CEA.

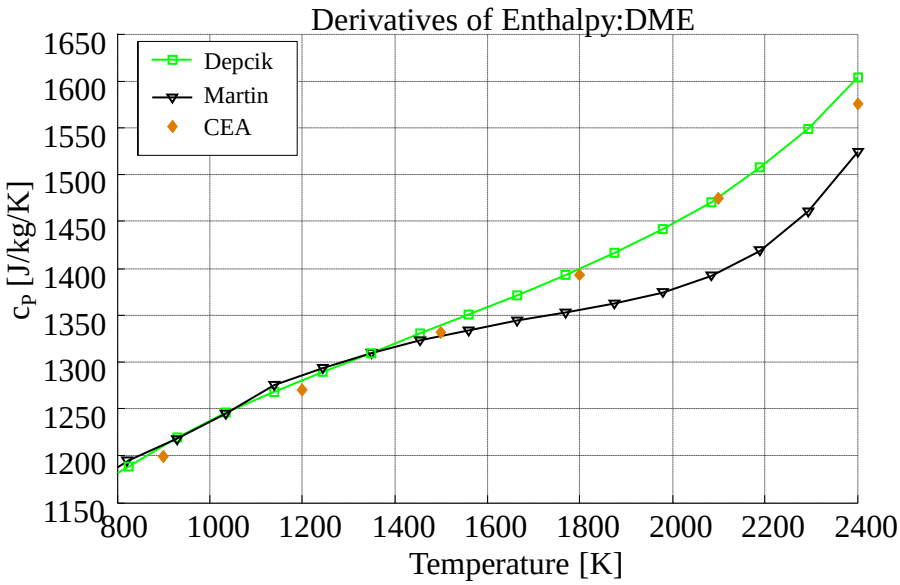

Figure B.7 Derivative of enthalpy with respect to temperature at constant pressure and constant equivalence ratio

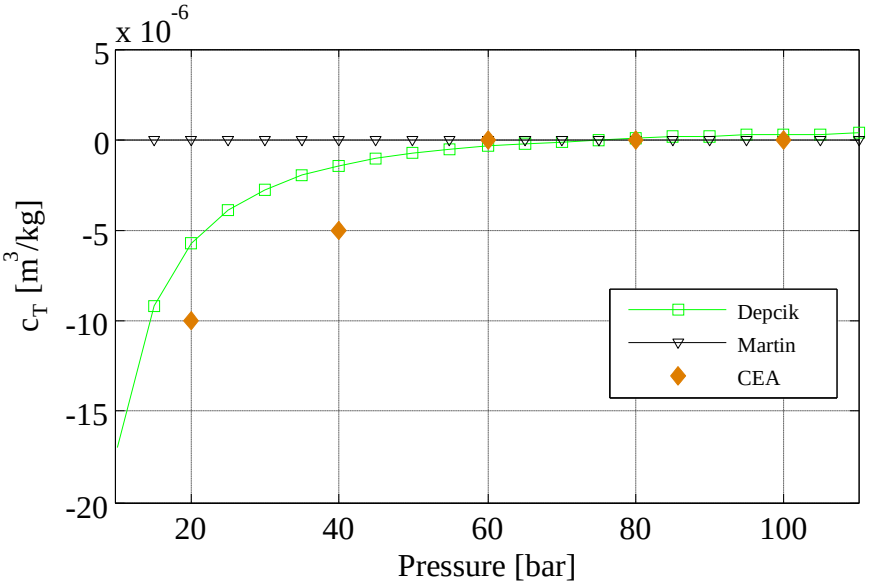

Figure B.8 Derivative of enthalpy with respect to pressure at constant temperature and constant equivalence ratio

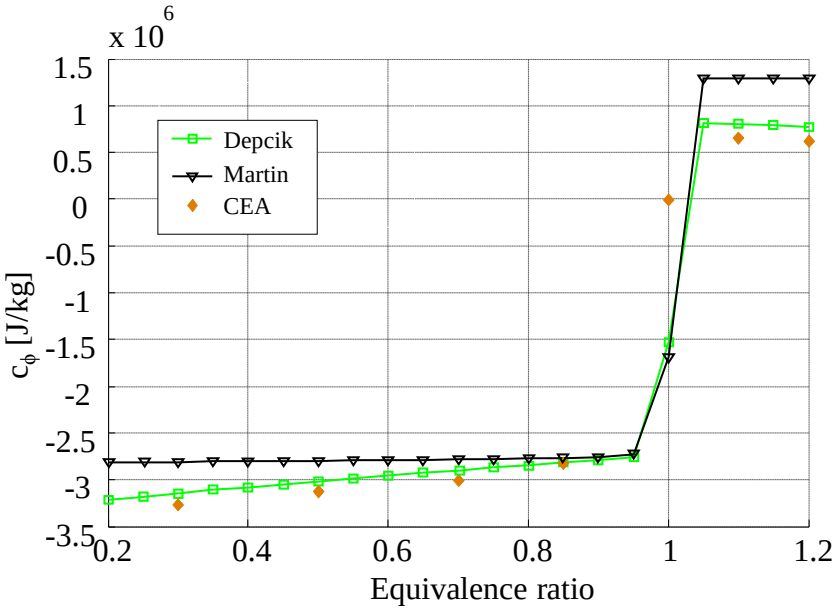

Figure B.9 Derivative of enthalpy with respect to equivalence ratio at constant pressure and constant temperature

C. The data used for ignition delay model

The data are obtained from Engine combustion network data base for fuel set 1 and Pickett and Siebers [82] for fuel set 2

1) Test fuel set 1: JP8, DF2, n-heptane, n-dodecane

	Ambient Density (kg/m^3)	O2 mole fraction	T (K)	P (bar)	τign (ms)	Fuel Tempe-rature (K)	Density of liquid fuel (kg/m^3)	Cetane number
JP8	14.8	0.21	962.7	40.88	0.98	373	746	38
	14.8	0.21	1004.0	42.63	0.87	373	746	38
	14.8	0.21	1099.2	46.67	0.64	373	746	38
	14.8	0.21	1191.3	50.58	0.54	373	746	38
	30	0.21	908.7	78.21	0.71	373	746	38
	30	0.21	1011.9	87.09	0.41	373	746	38
	7.27	0.21	1058.7	22.09	1.67	373	746	38
	7.27	0.21	1110.3	23.17	1.41	373	746	38
	7.27	0.21	1216.7	25.39	0.92	373	746	38
DF2	7.3	0.21	1200.0	24.80	0.55	373	767	46
	7.3	0.21	1050.0	21.70	1.27	373	767	46
	14.8	0.21	1200.0	50.60	0.33	373	767	46
	14.8	0.21	1000.0	42.30	0.57	373	767	46
	14.8	0.21	900.0	38.00	0.88	373	767	46
	14.8	0.21	850.0	35.90	1.25	373	767	46
	30	0.21	1000.0	86.40	0.31	373	767	46
	30	0.21	900.0	77.70	0.51	373	767	46
	7.3	0.15	1100.0	22.80	1.29	436	712	46
	7.3	0.15	1200.0	25.00	0.79	436	712	46
	14.8	0.15	900.0	38.20	1.15	436	712	46
	14.8	0.15	1000.0	42.40	0.73	436	712	46
	14.8	0.15	1100.0	46.80	0.48	436	712	46
	14.8	0.15	1200.0	51.00	0.35	436	712	46
	30	0.15	800.0	69.50	1.36	436	712	46
	30	0.15	900.0	78.40	0.60	436	712	46
	30	0.15	1200.0	104.60	0.20	436	712	46
n-heptane	14.8	0.08	1148.0	51.50	0.64	373	613	56
	14.8	0.08	1058.0	47.20	0.99	373	613	56
	14.8	0.08	967.0	42.90	1.52	373	613	56
	30	0.08	962.0	87.90	0.76	373	613	56
	14.8	0.1	1237.0	55.60	0.54	373	613	56
	14.8	0.1	1058.0	47.10	0.81	373	613	56
	14.8	0.1	1013.0	44.90	0.95	373	613	56
	14.8	0.1	967.0	42.80	1.13	373	613	56
	14.8	0.1	922.0	40.60	1.56	373	613	56
	14.8	0.1	875.0	38.50	1.74	373	613	56

	30	0.1	962.0	87.60	0.61	373	613	56
	14.8	0.12	967.0	42.70	0.95	373	613	56
	14.8	0.12	921.0	40.50	1.13	373	613	56
	14.8	0.12	876.0	38.40	1.33	373	613	56
	30	0.12	962.0	87.40	0.44	373	613	56
	14.8	0.15	967.0	42.50	0.73	373	613	56
	14.8	0.15	922.0	40.40	0.85	373	613	56
	14.8	0.15	876.0	38.20	1.10	373	613	56
	30	0.15	962.0	87.00	0.38	373	613	56
	14.8	0.21	1237.0	54.80	0.26	373	613	56
	14.8	0.21	1148.0	50.60	0.27	373	613	56
	14.8	0.21	1058.0	46.40	0.38	373	613	56
	14.8	0.21	967.0	42.10	0.53	373	613	56
	14.8	0.21	921.0	40.00	0.61	373	613	56
	14.8	0.21	876.0	37.90	0.79	373	613	56
	14.8	0.21	830.0	35.80	1.03	373	613	56
	14.8	0.21	783.0	33.70	1.65	373	613	56
n-dodecane	22.8	0.15	756.2	52.50	0.85	343	713	80
	22.8	0.15	799.3	56.10	0.50	343	713	80
	22.8	0.15	827.3	59.20	0.44	343	713	80
	22.8	0.15	837.6	59.40	0.41	343	713	80
	22.8	0.15	924.1	66.20	0.24	343	713	80
	22.8	0.15	1006.9	73.00	0.15	343	713	80
	22.8	0.15	1083.4	79.40	0.11	343	713	80

2) Test fuel set 2: T70, CN80, GE80 and BM88

The test data is tabulated from the literature [82].

	Ambient Density (kg/m^3)	O2 mole fraction	T (K)	P(bar)	τign (ms)	Fuel Tempe-rature (K)	Density of liquid fuel (kg/m^3)	Cetane number
T70	14.8	0.21	798.20	33.90	2.41	373	808	42.5
	14.8	0.21	848.46	36.04	1.50	373	808	42.5
	14.8	0.21	900.22	38.24	0.90	373	808	42.5
	14.8	0.21	951.77	40.43	0.67	373	808	42.5
	14.8	0.21	1003.28	42.62	0.50	373	808	42.5
	14.8	0.21	1099.61	46.71	0.28	373	808	42.5
	14.8	0.21	1199.19	50.94	0.19	373	808	42.5
	14.8	0.21	1298.74	55.17	0.13	373	808	42.5
	7.3	0.21	948.33	19.87	2.50	373	808	42.5
	7.3	0.21	998.33	20.92	1.60	373	808	42.5
	7.3	0.21	1050.00	22.00	1.13	373	808	42.5
	7.3	0.21	1098.33	23.01	0.76	373	808	42.5
	7.3	0.21	1195.00	25.04	0.45	373	808	42.5
	30	0.21	800.00	68.88	1.21	373	808	42.5
	30	0.21	848.33	73.04	0.59	373	808	42.5

	30	0.21	898.33	77.35	0.42	373	808	42.5
	30	0.21	996.67	85.81	0.14	373	808	42.5
	30	0.21	1098.33	94.57	0.08	373	808	42.5
	30	0.21	1195.00	102.89	0.06	373	808	42.5
CN80	14.8	0.21	802.27	34.08	1.05	373	724	80
	14.8	0.21	855.57	36.34	0.65	373	724	80
	14.8	0.21	905.44	38.46	0.45	373	724	80
	14.8	0.21	955.26	40.58	0.34	373	724	80
	14.8	0.21	1006.73	42.76	0.25	373	724	80
	14.8	0.21	1104.66	46.92	0.15	373	724	80
	14.8	0.21	1204.21	51.15	0.10	373	724	80
	14.8	0.21	1306.02	55.47	0.08	373	724	80
	7.3	0.21	948.33	19.87	0.93	373	724	80
	7.3	0.21	1001.67	20.99	0.76	373	724	80
	7.3	0.21	1050.00	22.00	0.64	373	724	80
	7.3	0.21	1098.33	23.01	0.53	373	724	80
	7.3	0.21	1200.00	25.14	0.31	373	724	80
	30	0.21	800.00	68.88	0.63	373	724	80
	30	0.21	848.33	73.04	0.45	373	724	80
	30	0.21	900.00	77.49	0.25	373	724	80
	30	0.21	1000.00	86.10	0.10	373	724	80
	30	0.21	1098.33	94.57	0.05	373	724	80
	30	0.21	1195.00	102.89	0.05	373	724	80
GE80	7.3	0.21	950.00	19.90	2.75	373	858	80
	7.3	0.21	1000.00	20.95	1.85	373	858	80
	7.3	0.21	1050.00	22.00	1.22	373	858	80
	7.3	0.21	1101.67	23.08	0.92	373	858	80
	7.3	0.21	1196.67	25.07	0.41	373	858	80
	14.8	0.21	798.95	33.94	1.05	373	858	80
	14.8	0.21	848.81	36.05	0.87	373	858	80
	14.8	0.21	903.63	38.38	0.73	373	858	80
	14.8	0.21	951.79	40.43	0.61	373	858	80
	14.8	0.21	1003.30	42.62	0.46	373	858	80
	14.8	0.21	1101.27	46.78	0.28	373	858	80
	14.8	0.21	1200.85	51.01	0.17	373	858	80
	14.8	0.21	1302.09	55.31	0.07	373	858	80
	30	0.21	800.00	68.88	0.41	373	858	80
	30	0.21	846.67	72.90	0.33	373	858	80
	30	0.21	901.67	77.63	0.23	373	858	80
	30	0.21	1000.00	86.10	0.13	373	858	80
	30	0.21	1098.33	94.57	0.05	373	858	80
	30	0.21	1200.00	103.32	0.05	373	858	80
BM88	14.8	0.21	797.87	33.89	2.01	373	907	80
	14.8	0.21	849.29	36.07	1.06	373	907	80
	14.8	0.21	900.71	38.26	0.67	373	907	80
	14.8	0.21	948.82	40.30	0.40	373	907	80
	14.8	0.21	1000.24	42.49	0.32	373	907	80
	14.8	0.21	1099.76	46.71	0.19	373	907	80

	14.8	0.21	1197.63	50.87	0.11	373	907	80
	14.8	0.21	1300.47	55.24	0.07	373	907	80
	7.3	0.21	950.00	19.90	1.08	373	907	80
	7.3	0.21	998.33	20.92	0.74	373	907	80
	7.3	0.21	1048.33	21.96	0.54	373	907	80
	7.3	0.21	1096.67	22.98	0.46	373	907	80
	7.3	0.21	1200.00	25.14	0.24	373	907	80
	30	0.21	798.33	68.74	1.21	373	907	80
	30	0.21	850.00	73.19	0.61	373	907	80
	30	0.21	898.33	77.35	0.38	373	907	80
	30	0.21	1000.00	86.10	0.14	373	907	80
	30	0.21	1098.33	94.57	0.05	373	907	80
	30	0.21	1200.00	103.32	0.05	373	907	80

Bibliography

1. **Diesel R.** Method of and apparatus for converting ehat into work., U.S. Patent US542846 AJul. 1895.
2. **National Highway Traffic Safety Administration** Alternative Fuel Vehicle Badging, Fuel Compartment Labels and Consumer Information on Alternative Fuel Usage: Proposed rules. Department of Transportation, Feb. 2014.
3. **Jung D.** A Multi-Zone Direct-Injection Diesel Spray Combustion Model for Cycle Simulation Studies of Large-Bore Engine Performance and Emissions., Ph.D. Dissertation, Department of Mechanical Engineering, University of Michigan, Ann Arbor, 2001.
4. **Ghojel J. I.** Review of the development and applications of the Wiebe function: A tribute to the contribution of Ivan Wiebe to engine research. *Int. J. Engine Res.* 2010; 11(4):297–312 DOI:10.1243/14680874JER06510.
5. **Miyamoto N., Chikahisa T., Murayama T., and Sawyer R.** Description and Analysis of Diesel Engine Rate of Combustion and Performance Using Wiebe's Functions. SAE Technical Paper 850107, 1985.
6. **Awad S., Varuvel E. G., Loubar K., and Tazerout M.** Single zone combustion modeling of biodiesel from wastes in diesel engine. *Fuel* 2013; 106:558–568 DOI:10.1016/j.fuel.2012.11.051.
7. **Catania A. E., Finesso R., and Spessa E.** Predictive zero-dimensional combustion model for DI diesel engine feed-forward control. *Energy Convers. Manag.* 2011; 52(10):3159–3175 DOI:10.1016/j.enconman.2011.05.003.
8. **Morel T. and Wahiduzzaman S.** Modeling of Diesel Combustion and Emissions. 96 FISITA Proceedings, 26th International Congress, Praha, Czech Republic, June 1996.
9. **Gao Z. and Schreiber W.** A phenomenologically based computer model to predict soot and NOx emission in a direct injection diesel engine. *Int. J. Engine Res.* 2001; 2(3):177–188 DOI:10.1243/1468087011545415.
10. **Zhou P., Zhou S., and Clelland D.** A modified quasi-dimensional multi-zone combustion model for direct injection diesels. *Int. J. Engine Res.* 2006; 7(4):335–345 DOI:10.1243/14680874JER02604.
11. **Rakopoulos C. D., Antonopoulos K. A., Rakopoulos D. C., and Hountalas D. T.** Multi-zone modeling of combustion and emissions formation in DI diesel engine operating on ethanol–diesel fuel blends. *Energy Convers. Manag.* 2008; 49(4):625–643 DOI:10.1016/j.enconman.2007.07.035.

12. **Cerri T., Onorati A., and Mattarelli E.** 1D Engine Simulation of a Small HSDI Diesel Engine Applying a Predictive Combustion Model. *J. Eng. Gas Turbines Power* 2008; 130(1):012802 1–10 DOI:10.1115/1.2747258.
13. **Perini F. and Mattarelli E.** Development and calibration of an enhanced quasi-dimensional combustion model for HSDI diesel engines. *Int. J. Engine Res.* 2011; 12(4):311–335 DOI:10.1177/1468087411401285.
14. **Hountalas D. T., Raptotasios S. I., and Zannis T. C.** Implications of Exhaust Gas, CO2, and N2 Recirculation on Heavy-Duty Diesel Engine Performance, Soot, and NO Emissions: A Comparative Study. *Energy Fuels* 2013; 27(8):4910–4929 DOI:10.1021/ef400289w.
15. **Hiroyasu H. and Arai M.** Fuel Spray Penetration and Spray Angle of Diesel Engines. *Trans JSAE* 1980; 21:5–11.
16. **Hiroyasu H., Toshikazu K., and Arai M.** Development and Use of a Spray Combustion Modeling to Predict Diesel Engine Efficiency and Pollutant Emissions. *Bull. JSME* 1983; 26(214):569–575.
17. **Yoshizaki T., Nishida K., and Hiroyasu H.** Approach to Low NOx and Smoke Emission Engines by Using Phenomenological Simulation. SAE Technical Paper 930612, 1993.
18. **Wakuri Y., Fujii M., Amitani T., and Tsuneya R.** Studies on the Penetration of Fuel Spray in a Diesel Engine. *Bull. JSME* 1960; 3(9):123–130.
19. **Dent J. C.** A Basis for the Comparison of Various Experimental Methods for Studying Spray Penetration. SAE Technical Paper 710571, 1971.
20. **Naber J. D. and Siebers D. L.** Effects of Gas Density and Vaporization on Penetration and Dispersion of Diesel Sprays. SAE Technical Paper 960034, 1996.
21. **Siebers D. L.** Scaling Liquid-Phase Fuel Penetration in Diesel Sprays Based on Mixing-Limited Vaporization. SAE Technical Paper 1999–01–0528, 1999.
22. **Sazhin S. S., Feng G., and Heikal M. R.** A model for fuel spray penetration. *Fuel* 2001; 80(15):2171–2180 DOI:10.1016/S0016-2361(01)00098-9.
23. **Desantes J. M., Payri R., Salvador F. J., and Gil A.** Development and validation of a theoretical model for diesel spray penetration. *Fuel* 2006; 85(7–8):910–917 DOI:10.1016/j.fuel.2005.10.023.
24. **Pickett L. M., Manin J., Genzale C. L., Siebers D. L., Musculus M. P. B., and Idicheria C. A.** Relationship Between Diesel Fuel Spray Vapor Penetration / Dispersion and Local Fuel Mixture Fraction. *SAE Int. J. Engines* 2011; 4(1):764–799 DOI:10.4271/2011-01-0686.
25. **Reitz R. D. and Bracco F. V.** On the Dependence of the Spray Angle and Other Spray Parameters on Nozzle Design and Operating Conditions. SAE Technical Paper 790494, 1979.
26. **MacGregor S. A.** Air entrainment in spray jets. *Int. J. Heat Fluid Flow* 1991; 12(3):279–283 DOI:10.1016/0142-727X(91)90064-3.
27. **Cossali G. E.** An integral model for gas entrainment into full cone sprays. *J. Fluid Mech.* 2001; 439:353–366 DOI:10.1017/S0022112001004591.
28. **Abramzon B. and Sirignano W. A.** Droplet vaporization model for spray combustion calculations. *Int. J. Heat Mass Transf.* 1989; 32(9):1605–1618 DOI:10.1016/0017-9310(89)90043-4.

29. **Stengele J., Prommersberger K., Willmann M., and Wittig S.** Experimental and theoretical study of one- and two-component droplet vaporization in a high pressure environment. *Int. J. Heat Mass Transf.* 1999; 42(14):2683–2694 DOI:10.1016/S0017-9310(98)00285-3.
30. **Burger M., Schmehl R., Prommersberger K., Schafer O., Koch R., and Wittig S.** Droplet evaporation modeling by the distillation curve model: accounting for kerosene fuel and elevated pressures. *Int. J. Heat Mass Transf.* 2003; 46(23):4403–4412 DOI:10.1016/S0017-9310(03)00286-2.
31. **Hohmann S. and Renz U.** Numerical simulation of fuel sprays at high ambient pressure: the influence of real gas effects and gas solubility on droplet vaporisation. *Int. J. Heat Mass Transf.* 2003; 46(16):3017–3028 DOI:10.1016/S0017-9310(03)00077-2.
32. **Ra Y. and Reitz R. D.** A vaporization model for discrete multi-component fuel sprays. *Int. J. Multiph. Flow* 2009; 35(2):101–117 DOI:10.1016/j.ijmultiphaseflow.2008.10.006.
33. **Zhang L. and Kong S.-C.** Modeling of multi-component fuel vaporization and combustion for gasoline and diesel spray. *Chem. Eng. Sci.* 2009; 64(16):3688–3696 DOI:10.1016/j.ces.2009.05.013.
34. **Novella R., García A., Pastor J. M., and Domenech V.** The role of detailed chemical kinetics on CFD diesel spray ignition and combustion modelling. *Math. Comput. Model.* 2011; 54(7–8):1706 – 1719 DOI:http://dx.doi.org/10.1016/j.mcm.2010.12.048.
35. **Brakora J. and Reitz R.** A Comprehensive Combustion Model for Biodiesel-Fueled Engine Simulations. presented at SAE Technical Paper 2013.
36. **Ismail H. M., Ng H. K., Gan S., Lucchini T., and Onorati A.** Development of a reduced biodiesel combustion kinetics mechanism for CFD modelling of a light-duty diesel engine. *Fuel* 2013; 106(0):388 – 400 DOI:http://dx.doi.org/10.1016/j.fuel.2012.10.015.
37. **Halstead M. P., Kirsch L. J., Prothero A., and Quinn C. P.** A Mathematical Model for Hydrocarbon Autoignition at High Pressures. *Proc. R. Soc. Math. Phys. Eng. Sci.* 1975; 346(1647):515–538 DOI:10.1098/rspa.1975.0189.
38. **Sazhina E. M., Sazhin S. S., Heikal M. R., and Marooney C. J.** The Shell autoignition model: applications to gasoline and diesel fuels. *Fuel* 1999; 78(4):389–401 DOI:10.1016/S0016-2361(98)00167-7.
39. **Hamosfakidis V. and Reitz R. D.** Optimization of a hydrocarbon fuel ignition model for two single component surrogates of diesel fuel. *Combust. Flame* 2003; 132(3):433–450 DOI:10.1016/S0010-2180(02)00489-3.
40. **Watson N., Pilley A. D., and Marzouk M. A.** Combustion Correlation for Diesel Engine Simulation. SAE Technical Paper 800029, 1980.
41. **Assanis D. N., Filipi Z. S., Fiveland S. B., and Syrimis M.** A Predictive Ignition Delay Correlation Under Steady-State and Transient Operation of a Direct Injection Diesel Engine. *J. Eng. Gas Turbines Power* 2003; 125(2):450 DOI:10.1115/1.1563238.
42. **Zheng M., Mulenga M. C., Reader G. T., Wang M., Ting D. S.-K., and Tjong J.** Biodiesel engine performance and emissions in low temperature combustion. *Fuel* 2008; 87(6):714–722 DOI:10.1016/j.fuel.2007.05.039.

43. **Maroteaux F. and Saad C.** Diesel engine combustion modeling for hardware in the loop applications: Effects of ignition delay time model. *Energy* 2013; 57:641–652 DOI:10.1016/j.energy.2013.03.098.
44. **Hountalas D. T., Lamaris V. T., Pariotis E. G., and Ofner H.** Parametric Study Based on a Phenomenological Model to Investigate the Effect of Post Fuel Injection on HDDI Diesel Engine Performance and Emissions–Model Validation Using Experimental Data. SAE Technical Paper 2008–01–0641, 2008 DOI:10.4271/2008-01-0641.
45. **Wolfer H. H.** Ignition lag in diesel engines. *VDI-Forschungsheft* 1938; 392:621–436.
46. **Kavtaradze R. Z., Zeilinger K., and Zitzler G.** Ignition Delay in a Diesel Engine Utilizing Different Fuels. *High Temp.* 2005; 43(6):951–960 DOI:10.1007/s10740-005-0143-z.
47. **Aligrot C., Champoussin J. C., Guerrassi N., and Claus G.** Prediction of Self-Ignition Delay of Different Liquid Diesel Fuels. International Symposium COMODIA 331, 1991.
48. **Hardenberg H. O. and Hase F. W.** An Empirical Formula for Computing the Pressure Rise Delay of a Fuel from Its Cetane Number and from the Relevant Parameters of Direct-Injection Diesel Engines. SAE Technical Paper 1979–02–01, 1979.
49. **Nishida K. and Hiroyasu H.** Simplified Three-Dimensional Modeling of Mixture Formation and Combustion in a D.I. Diesel Engine. SAE Technical Paper 890269, 1989.
50. **Rakopoulos C. D. and Hountalas D. T.** Development and Validation of a 3-D Multi-Zone Combustion Model for the Prediction of DI Diesel Engines Performance and Pollutants Emissions. SAE Technical Paper 981021, 1998.
51. **Hountalas D. T., Kouremenos D. A., and Pariotis E. G.** Using a Phenomenological Multi-Zone Model to Investigate the Effect of Injection Rate Shaping on Performance and Pollutants of a DI Heavy Duty Diesel Engine. SAE paper 2002–01–0074, 2002.
52. **Westbrook C. K. and Dryer F. L.** Chemical kinetic modeling of hydrocarbon combustion. *Prog. Energy Combust. Sci.* 1984; 10(1):1–57 DOI:10.1016/0360-1285(84)90118-7.
53. **Maiboom A., Tauzia X., Shah S. R., and Hétet J.-F.** New Phenomenological Six-Zone Combustion Model for Direct-Injection Diesel Engines. *Energy Fuels* 2009; 23(2):690–703 DOI:10.1021/ef800735d.
54. **Meng X., Jiang Z., Wang X., and Jiang D.** Quasi-dimensional multizone combustion model for direct injection engines fuelled with dimethyl ether. *Proc. Inst. Mech. Eng. Part J. Automob. Eng.* 2004; 218(3):315–322 DOI:10.1243/095440704322955830.
55. **Ma G., Tauzia X., and Maiboom A.** One-dimensional combustion model with detailed chemistry for transient diesel sprays. *Proc. Inst. Mech. Eng. Part J. Automob. Eng.* 2014; 0954407013518036 DOI:10.1177/0954407013518036.
56. **Levich V. G.** Physicochemical Hydrodynamics., 2nd ed., Prentice-Hall, Englewood Cliffs, NJ, ISBN 978-0136744405, 1962.

57. **Faeth G. ., Hsiang L.-P., and Wu P.-K.** Structure and breakup properties of sprays. *Int. J. Multiph. Flow* 1995; 21, Supplement:99–127 DOI:10.1016/0301-9322(95)00059-7.
58. **Chryssakis C.** A unified fuel spray breakup model for internal combustion engine applications., Ph.D. Dissertation, Department of Mechanical Engineering, University of Michigan, Ann Arbor, 2005.
59. **Reitz R. D.** Modeling Atomization Processes in High-Pressure Vaporizing Sprays. *At. Spray Technol.* 1987; 3:309–337.
60. **El Wakil M. M., Uyehara O. A., and Myers P. S.** A theoretical investigation of the heating-up period of injected fuel droplets vaporizing in air. *Natl. Advis. Comm. Aeronaut.* 1954; 3179 of Technical note.
61. **Ranz W. E. and Marshall W. .** Evaporation from drops: Part I. *Chem. Eng. Prog.* 1952; 48:141–146.
62. **Pitzer K. S., Lippmann D. Z., Curl R. F., Huggins C. M., and Petersen D. E.** The Volumetric and Thermodynamic Properties of Fluids. II. Compressibility Factor, Vapor Pressure and Entropy of Vaporization1. *J. Am. Chem. Soc.* 1955; 77(13):3433–3440 DOI:10.1021/ja01618a002.
63. **Poling B. E., Prausnitz J. M., and Connell J. O.** The Properties of Gases and Liquids., 5th ed., McGraw-Hill Prof Med/Tech, ISBN 978-0070116825, 2000.
64. **Estes K. A. and Mudawar I.** Correlation of sauter mean diameter and critical heat flux for spray cooling of small surfaces. *Int. J. Heat Mass Transf.* 1995; 38(16):2985–2996 DOI:10.1016/0017-9310(95)00046-C.
65. **Kim H. J., Park S. H., Suh H. K., and Lee C. S.** Atomization and Evaporation Characteristics of Biodiesel and Dimethyl Ether Compared to Diesel Fuel in a High-Pressure Injection System. *Energy Fuels* 2009; 23(3):1734–1742 DOI:10.1021/ef800811g.
66. **Pickett L. M. and Hoogterp L.** Fundamental spray and combustion measurements of JP-8 at diesel conditions. *SAE Int. J. Commer. Veh.* 2008; 1(1):108–118 DOI:10.4271/2008-01-1083.
67. **Nomura H., Ujiie Y., Rath H. J., Sato J., and Kono M.** Experimental study on high-pressure droplet evaporation using microgravity conditions. *Symp. Int. Combust.* 1996; 26(1):1267–1273 DOI:10.1016/S0082-0784(96)80344-4.
68. **Gökalp I., Chauveau C., Berrekam H., and Ramos-Arroyo N. A.** Vaporization of miscible binary fuel droplets under laminar and turbulent convective conditions. *At. Sprays* 1994; 4(6):661–676.
69. **Dwyer H. A. and Sanders B. R.** Detailed computation of unsteady droplet dynamics. *Symp. Int. Combust.* 1985; 20(1):1743–1749 DOI:10.1016/S0082-0784(85)80671-8.
70. **Liang L., Naik C. V., Puduppakkam K., Wang C., Modak A., Meeks E., Ge H., Reitz R., and Rutland C.** Efficient Simulation of Diesel Engine Combustion Using Realistic Chemical Kinetics in CFD. SAE Technical Paper 2010–01–0178, 2010 DOI:10.4271/2010-01-0178.
71. **Schihl P., Hoogterp L., and Pangilinan H.** Assessment of JP-8 and DF-2 Evaporation Rate and Cetane Number Differences on a Military Diesel Engine. SAE Technical Paper 2006–01–1549, 2006 DOI:10.4271/2006-01-1549.

72. **Zigan L., Schmitz I., Flügel A., Wensing M., and Leipertz A.** Structure of evaporating single- and multicomponent fuel sprays for 2nd generation gasoline direct injection. *Fuel* 2011; 90(1):348–363 DOI:10.1016/j.fuel.2010.08.001.
73. **Kadota T. and Hiroyasu H.** Evaporation of a Single Droplet at Elevated Pressures and Temperatures : 2nd Report, Theoretical Study. *Bull. JSME* 1976; 19(138):1515–1521.
74. **Sandia National Laboratories** Diesel Spray Combustion., *Engine Combustion Network*. [Online]. Available: http://www.sandia.gov/ecn/.
75. **Ciezki H. and Adomeit G.** Shock-tube investigation of the ignition delay on n-heptane/air-mixtures in a high pressure shock tube under conditions relevant to diesel-engine combustion. *AIP Conf. Proc.* 1990; 208(1):707–712 DOI:doi:10.1063/1.39508.
76. **ASTM D613 – 10a** Test Method for Cetane Number of Diesel Fuel Oil. ASTM International 2010;
77. **ASTM D6890-07a** Test Method for Determination of Ignition Delay and Derived Cetane Number (DCN) of Diesel Fuel Oils by Combustion in a Constant Volume Chamber. ASTM International D6890 – 07a 2013;
78. **Meredith B. Colket III and Louis J. Spadaccini** Scramjet Fuels Autoignition Study. *J. Propuls. Power* 2001; 17(2):315–323.
79. **Penyazkov O. G., Sevrouk K. L., Tangirala V., and Joshi N.** Autoignitions of Diesel Fuel/Air Mixtures Behind Reflected Shock Waves. Proceedings of the European Combustion Meeting 2009.
80. **Dean A. J., Penyazkov O. G., Sevruk K. L., and Varatharajan B.** Autoignition of surrogate fuels at elevated temperatures and pressures. *Proc. Combust. Inst.* 2007; 31(2):2481–2488 DOI:10.1016/j.proci.2006.07.162.
81. **Livengood J. C. and Wu P. C.** Correlation of Autoignition Phenomena in Internal Combustion Engines and Rapid Compression Machines. Proceedings of Fifth International Symposium on Combustion 347–356, 1955.
82. **Pickett L. M. and Siebers D. L.** Fuel Effects on Soot Processes of Fuel Jets at DI Diesel Conditions. SAE Technical Paper 2003–01–3080, 2003.
83. **Edelman R. B. and Harsha P. T.** Laminar and turbulent gas dynamics in combustors—current status. *Prog. Energy Combust. Sci.* 1978; 4(1):1–62 DOI:10.1016/0360-1285(78)90010-2.
84. **Weibull W.** A Statistical Distribution Function of Wide Applicability. *J. Appl. Mech.* 1951; 293–297.
85. **Assanis D. N. and Heywood J. B.** Development and Use of a Computer Simulation of the Turbocompounded Diesel System for Engine Performance and Component Heat Transfer Studies. SAE Technical Paper 860329, 1986.
86. **Woschni G.** A Universally Applicable Equation for the Instantaneous Heat Transfer Coefficient in the Internal Combustion Engine. SAE Technical Paper 670931, 1967.
87. **Annand W. J. D.** Heat Transfer in the Cylinders of Reciprocating Internal Combustion Engines. *Proc. Inst. Mech. Eng.* 1963; 177(1):973–996 DOI:10.1243/PIME_PROC_1963_177_069_02.
88. **Heywood J.** Internal Combustion Engine Fundamentals., 1st ed., McGraw-Hill, ISBN 007028637X, 1988.

89. **Daubert, TE and Danner, RP** API technical data book-petroleum refining., 6th ed., American Petroleum Institute (API), Washington D.C, 1997.
90. **Perry R. H. and Green D. W.** Perry's chemical engineers' handbook., McGraw-Hill, New York, ISBN 9780071593137 0071593136 0071601503 9780071601504 1601196520 9781601196521, 2008.
91. **Design Institute for Physical Properties, Sponsored by AIChE** DIPPR Project 801-Evaluated Standard Thermophysical Property Values., Design Institute for Physical Properties/AlChe, 2012.
92. **Depcik C.** Open-Ended Thermodynamic Cycle Simulation., MS Thesis of University of Michigan, 2000.
93. **Martin M. k. and Heywood J. B.** Approximate Relationships for the Thermodynamic Properties of Hydrocarbon-Air Combustion Products. *Combust. Sci. Technol.* 1977; 15:1–10.
94. **Salvi A. A., Assanis D., and Filipi Z.** Impact of Physical and Chemical Properties of Alternative Fuels on Combustion, Gaseous Emissions, and Particulate Matter during Steady and Transient Engine Operation. *Energy Fuels* 2012; 26(7):4231–4241 DOI:10.1021/ef300531r.
95. **S.H. Won, S. Dooley, P.S. Veloo, H. Wang, M.A. Oehlschlaeger, F.L. Dryer, and Y. Ju** Quantification of Molecule Structure Impact on Combustion Properties for Synthetic Diesel Fuel: 2,6,10-Trimethyldodecane. presented at 8th US National Technical Meeting of the Combustion Institute,Salt Lake City, UT 2013.
96. **Michael Mosburger, Sick V., and Drake M. C.** Quantitative high-speed imaging of burned gas temperature and equivalence ratio in internal combustion engines using alkali metal fluorescence. *Int. J. Engine Res.* 2013;
97. **Olikara C. and Borman G. L.** A Computer Program for Calculating Properties of Equilibrium Combustion Products with Some Applications to I.C. Engines. SAE Technical Paper 750468, 1975.